From bacteria to biosensors
Engineering gas vesicles for biomolecular ultrasound imaging

Terwiel, D.

DOI
10.4233/uuid:f56b02a7-8a52-43cf-89c9-6b9c755229f9

Publication date
2025

Document Version
Final published version

Citation (APA)
Terwiel, D. (2025). *From bacteria to biosensors: Engineering gas vesicles for biomolecular ultrasound imaging*. [Dissertation (TU Delft), Delft University of Technology]. https://doi.org/10.4233/uuid:f56b02a7-8a52-43cf-89c9-6b9c755229f9

From Bacteria to Biosensors

Engineering Gas Vesicles For Biomolecular Ultrasound Imaging

Dion Terwiel

FROM BACTERIA TO BIOSENSORS

ENGINEERING GAS VESICLES FOR BIOMOLECULAR ULTRASOUND IMAGING

FROM BACTERIA TO BIOSENSORS

ENGINEERING GAS VESICLES FOR BIOMOLECULAR ULTRASOUND IMAGING

Proefschrift

ter verkrijging van de graad van doctor
aan de Technische Universiteit Delft,
op gezag van de Rector Magnificus Prof. dr.ir. T.H.J.J. van der Hagen,
voorzitter van het College voor Promoties,
in het openbaar te verdedigen op donderdag 25 september 2025 om 10:00 uur

door

Dion TERWIEL

Ingenieur Biotechnologie,
Technische Universiteit Delft,
geboren te Schiedam, Nederland.

Dit proefschrift is goedgekeurd door de

Promotor: prof. dr. N. de Jong
Copromotor: dr. D. Maresca

Samenstelling promotiecommissie:

Rector Magnificus,	voorzitter
Prof. dr. N. de Jong,	Technische Universiteit Delft
Dr. D. Maresca,	Technische Universiteit Delft
Onafhankelijke leden:	
Dr. A. Bar-Zion,	Technion IIT
Dr. N. Nakatsuka,	École Polytechnique Fédérale de Lausanne
Prof. dr. ir. M. Ottens,	Technische Universiteit Delft
Prof. dr. A. Stiel,	Helmholtz Munich
Prof. dr. F. Hollmann,	Technische Universiteit Delft, reservelid

The work in this thesis was supported by the Dutch research council (NWO.STU. 019.021).

Printed by: Gildeprint B.V.

Front & Back: A visual analogy, where GVs experiencing ultrasound waves are represented as surfers experiencing ocean waves. The back cover shows calm waters. Created by providing google Gemini AI with a draft image with the prompt: "please make this image look nicer"

ISBN 978-94-6518-119-6

CONTENTS

SUMMARY

Ultrasound imaging is a cornerstone of medical diagnostics, offering high-resolution, real-time visualization of anatomical structures. However, its application to molecular and cellular imaging has been limited by the lack of nanoscale contrast agents. Gas vesicles (GVs), air-filled protein nanostructures evolved for buoyancy in microorganisms, offer transformative potential in this domain. This thesis explores the engineering and application of GVs as biomolecular ultrasound contrast agents, emphasizing their use as biosensors for molecular imaging. It builds on their unique genetic encodability, tunable acoustic properties, and nanoscale dimensions to address key limitations in ultrasound imaging.

In chapter 1 and chapter 2 we introduce the potential of GVs as genetically encoded ultrasound contrast agents, highlighting their advantages over traditional agents like microbubbles. These chapters provide an overview of ultrasound imaging's evolution, focusing on the emerging field of biomolecular ultrasound imaging, which leverages GVs to bridge the gap between molecular processes and ultrasound modalities. Applications such as neuroscience imaging and functional imaging of dynamic biological processes are discussed, emphasizing GVs' nanoscale properties and unique acoustic behavior.

The contents of chapter 3 focus on the cryo-electron microscopy (cryo-EM) structural analysis of GVs. This study provides an atomic-level model of the GV shell, particularly in the absence of the reinforcement protein GvpC. By combining structural insights with a sequence analysis of GvpC, the chapter proposes a hypothetical binding mechanism that informs mutagenesis experiments in later work. This structural foundation is critical for the subsequent engineering of GVs for biosensor applications.

In chapter 4 we present the development and validation of *pHonon*, the first GV-based pH biosensor. By engineering pH-sensitive histidine residues into GvpC, the biosensor's acoustic properties were tuned to detect pH variations. Validation experiments, conducted both in vitro and in vivo, demonstrated *pHonon*'s efficacy for real-time, non-invasive pH imaging. This work highlights the versatility of GVs as platforms for biosensor engineering and their potential for applications in both basic research and clinical diagnostics.

Then, chapter 5 explores alternative approaches to enhancing GV functionality through aggregation. By inducing GV clustering via methods like biotin-streptavidin interactions and depletion interactions, significant improvements in ultrasound contrast were achieved. This chapter shows that aggregation enhances both linear and non-linear acoustic responses, providing a complementary strategy to genetic engineering for optimizing GV performance. These findings open new avenues for improving the signal strength and utility of GVs in various imaging applications.

The thesis concludes by summarizing the key findings and their implications for the field of biomolecular ultrasound imaging. It emphasizes the breakthroughs achieved, such as the high-resolution GV structural model, the development of *pHonon*, and the exploration of aggregation-based contrast enhancement. These contributions advance the field significantly, offering innovative solutions to challenges in molecular imaging. This thesis lays the basis for future research on broadening the array of biomarkers identifiable by GVs, improving genetic engineering methods, and investigating additional imaging techniques to enhance the effectiveness of biomolecular ultrasound imaging.

SAMENVATTING

Echografie is een hoeksteen van de medische diagnostiek, met hoge resolutie, realtime visualisatie van anatomische structuren. De toepassing ervan op moleculaire en cellulaire beeldvorming is echter beperkt door het gebrek aan contrastmiddelen op de nanoschaal. Gasvesikels (GVs), met lucht gevulde eiwit-nanostructuren die geëvolueerd zijn voor drijfvermogen in micro-organismen, bieden transformatief potentieel in dit domein. Dit proefschrift onderzoekt de ontwikkeling en toepassing van GVs als biomoleculaire contrastmiddelen voor echografie, met een nadruk op hun gebruik als biosensoren voor moleculaire beeldvorming. Het bouwt voort op hun unieke genetische encodeerbaarheid, afstembare akoestische eigenschappen en nanoschaaldimensies om belangrijke beperkingen in echografie aan te pakken.

In hoofdstuk 1 en hoofdstuk 2 introduceren we de mogelijkheden van GVs als genetisch gecodeerde contrastmiddelen voor echografie, waarbij hun voordelen ten opzichte van traditionele middelen zoals microbubbles worden benadrukt. Deze hoofdstukken geven een overzicht van de evolutie van echografie, met de nadruk op het opkomende veld van biomoleculaire ultrageluidbeeldvorming. Dit veld benut GVs om de kloof te overbruggen tussen moleculaire processen en echografiemodaliteiten. Toepassingen zoals hersenactiviteitsbeeldvoorming en functionele beeldvorming van dynamische biologische processen worden besproken, waarbij de nanoschaaleigenschappen en het unieke akoestische gedrag van GVs worden benadrukt.

De inhoud van hoofdstuk 3 richt zich op de structurele analyse van GVs met cryo-elektronenmicroscopie (cryo-EM). Deze studie biedt een atoomniveau-model van de GV-wand, met name in afwezigheid van het versterkingseiwit GvpC. Door structurele inzichten te combineren met een eiwitsequentieanalyse van GvpC, stelt dit hoofdstuk een hypothetisch bindingsmechanisme voor dat mutagenese-experimenten in later werk informeert. Deze structurele basis is cruciaal voor de daaropvolgende ontwikkeling van GVs voor biosensor-toepassingen.

In hoofdstuk 4 presenteren we de ontwikkeling en validatie van *pHonon*, de eerste GV pH-biosensor. Door pH-gevoelige histidineresiduen in GvpC te integreren, werden de akoestische eigenschappen van de biosensor beïnvloed om pH-variaties te detecteren. Validatie-experimenten, uitgevoerd zowel in vitro als in vivo, toonden de effectiviteit van *pHonon* aan voor realtime, niet-invasieve pH-meting. Dit werk benadrukt de veelzijdigheid van GVs als basis voor biosensorontwikkeling en hun potentieel voor toepassingen in zowel fundamenteel onderzoek als klinische diagnostiek.

Vervolgens verkent hoofdstuk 5 alternatieve benaderingen om de functionaliteit van GVs te verbeteren via aggregatie. Door GV-clustering te induceren via methoden zoals biotine-streptavidine-interacties en depletie-interacties, werden significante verbeteringen in ultrageluidcontrast bereikt. Dit hoofdstuk laat zien dat aggregatie zowel lineaire als niet-lineaire akoestische responsen versterkt en een complementaire strategie biedt naast genetische engineering om de prestaties van GVs te optimaliseren. Deze bevindingen openen nieuwe wegen om de signaalsterkte en bruikbaarheid van GVs in verschillende beeldvormingstoepassingen te verbeteren.

Het proefschrift sluit af met een samenvatting van de belangrijkste bevindingen en hun implicaties voor het veld van biomoleculaire ultrageluidbeeldvorming. Het benadrukt de behaalde doorbraken, zoals het hoge resolutie GV-structuurmodel, de ontwikkeling van *pHonon*, en de verkenning van op aggregatie gebaseerde contrastverbetering. Deze bijdragen betekenen een aanzienlijke vooruitgang voor het veld en bieden innovatieve oplossingen voor langdurige uitdagingen in moleculaire beeldvorming. Toekomstige richtingen omvatten het uitbreiden van het scala aan biomarkers dat door GVs kan worden gedetecteerd, het verfijnen van genetische engineeringstrategieën, en het onderzoeken van complementaire beeldvormingstechnieken om de mogelijkheden van biomoleculaire ultrageluidbeeldvorming verder uit te breiden.

1

INTRODUCTION

> *In concentrating on the study of a small corner of biology, there is always the hope that one may uncover information that can be applied more widely in the subject.*
>
> Anthony E. Walsby

These were the words of Anthony Walsby in his highly cited review paper where he discusses the properties of gas vesicles (GVs) that, 20 years later, would start off a revolution in an entirely unexpected field: ultrasound imaging. Gas vesicles, genetically encoded gas-filled protein nanostructures, are uniquely suited as ultrasound contrast agents due to their air-filled interiors. Their genetic encodability for the first time allowed ultrasound imaging to assess molecular processes inside opaque organisms. Additionally, their tiny size allows them access to smaller vasculature making them uniquely suited for functional ultrasound imaging. Finally, GVs are exceptionally suited to be engineered into biosensors. In this thesis, we will explore GV biosensors in more detail, starting with a more accurate cryo-EM based atomic model of GVs, and building on this to show the first GV-based ultrasound biosensor for pH. Finally, we open the door for a novel approach to engineering of GV biosensors: aggregation of GVs.

PROJECT INTRODUCTION

Ultrasound imaging is one of the most widely used medical imaging modalities in the world. Since its introduction into clinical practice in the late 18th century, ultrasound has become a go-to technology in medical clinics, valued for its ability to provide real-time imaging at the organ scale. Its unique combination of high spatial and temporal resolution, capability to penetrate deep into opaque tissues, and accessibility of the equipment makes it particularly well-suited for imaging anatomical features of the human body. Today, ultrasound imaging is an indispensable tool in nearly every field of medicine, employed for diagnosing a wide array of pathologies. From obstetrics and cardiology to oncology and musculoskeletal imaging, its versatility ensures its continued prominence in clinical practice.

Beyond its use in diagnostic medicine, ultrasound imaging has also emerged as a powerful tool in scientific research. Historically, ultrasound research was largely restricted to large animal models such as pigs, sheep, and non-human primates due to the limitations of imaging technology. However, the rapid advancements in microelectronics and computational power since the early 1990s have revolutionized the field, enabling high-resolution imaging of smaller animals, such as mice and rats. These technological advancements have not only made small-animal imaging feasible but have also significantly expanded the range and depth of information obtainable from ultrasound images.

For example, Doppler imaging has enabled researchers to visualize blood flow velocity, a capability that paved the way for functional ultrasound imaging, which can be used to observe dynamic processes like brain activity [1]. Similarly, the advent of contrast-enhanced ultrasound imaging has introduced highly specific and targeted imaging techniques, including methods for visualizing particular cell types and tissues, achieving super-resolution imaging [2], and even delivering targeted therapeutics [3]. These advancements underscore the growing utility of ultrasound as a research tool, particularly in the life sciences.

Despite these innovations, the use of ultrasound for molecular and cellular imaging has historically been limited. This field has been predominated by optical imaging methods, which offer higher resolution and an array of well-established nano-scale contrast agents. The relatively lower resolution of ultrasound compared to optical modalities, combined with the lack of cell-specific, nano-scale contrast agents, restricted its application to molecular-scale imaging. However, recent breakthroughs have started to bridge this gap.

The discovery of GVs—air-filled protein nanostructures—has opened up new possibilities for molecular and cellular ultrasound imaging [4]. GVs provide a novel means of imaging dynamic biological processes such as gene expression [5], cell surface modifications [6, 7], and tumor development [8, 9]. One of the most compelling properties of GVs as ultrasound contrast agents is their genetic and structural tunability [10], allowing researchers to tailor their acoustic properties for specific applications. Of particular importance is their ability to act as biosensing molecular reporters [11]. By modifying the structural protein GvpC, which reinforces the GV shell, it is possible to alter the stiffness of the vesicles. This stiffness directly influences the non-linear response of GVs to ultrasound waves, thereby enabling their use as biosensors. Non-linear ultrasound signals, which are affected by changes in GVs' mechanical properties, provide a measurable and specific readout that can be harnessed for detecting molecular-scale events.

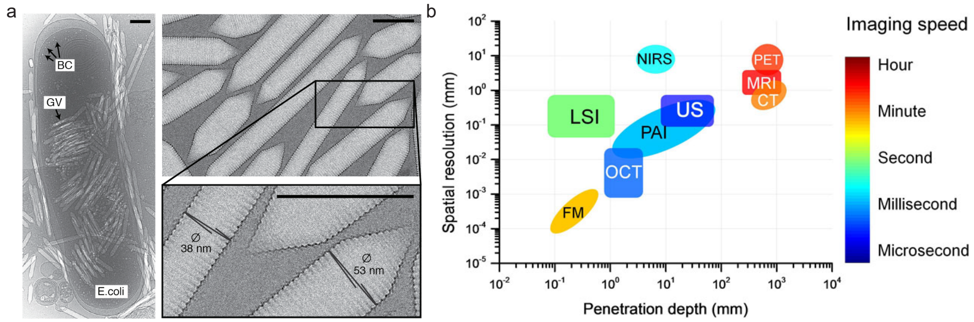

Figure 1.1: a, Cryo-EM micrographs of *Bacillus Megaterium* GVs in *Eschericia coli*, and in isolation [12]. b, Comparisons of the penetration depth, spatial resolution, and image speed among various techniques for neuroimaging, including magnetic resonance imaging (MRI), computed tomography (CT), positron emission tomography (PET), ultrasound imaging (US), optical coherence tomography (OCT), photoacoustic imaging (PAI), fluorescence microscopy (FM), near-infrared spectral imaging (NIRS), and laser speckle imaging (LSI), reprinted with caption from [13]

MOLECULAR ULTRASOUND IMAGING

Molecular imaging is the visualization of molecular and cellular processes within live, intact organisms. A variety of imaging modalities exist, each with unique advantages and limitations, including MRI, CT, SPECT, PET, optical imaging, photoacoustics, and ultrasound (Figure 1.1). Among these, ultrasound imaging offers high spatial and temporal resolution, as well as significant penetration depth, making it an attractive option for many applications. However, its broader applicability has historically been constrained by the lack of specific contrast agents, a limitation explored in more detail in chapter 2. Contrast-enhanced ultrasound imaging has long relied on a main type of contrast agent: microbubbles. These phospholipid-shelled bubbles range in size from 1 to 15 µm and have gas-filled interiors, which provide a substantial acoustic impedance mismatch compared to tissue or blood [14]. This property makes them highly effective as contrast agents. Microbubbles enabled some of the earliest molecular imaging experiments by targeting surface-displayed molecules using ligands conjugated to their surfaces [15]. Despite this success, microbubbles have significant limitations. Their large size restricts their ability to penetrate into deep tissues, limiting their utility in systemic imaging. Furthermore, microbubbles cannot probe intracellular targets, reducing their specificity to surface molecules. Finally, their lack of a genotype-phenotype link prevents them from detecting molecular or genomic variations that are not externally displayed.

GAS VESICLES AS ULTRASOUND CONTRAST AGENTS

The discovery of gas vesicles (GVs) as a nanoscale alternative to microbubbles [4] addresses many of these challenges. GVs are protein-based structures naturally used by cyanobacteria and other microorganisms as buoyancy devices to regulate their position in water columns [16]. They are found in over 150 prokaryotic species spanning five bacterial

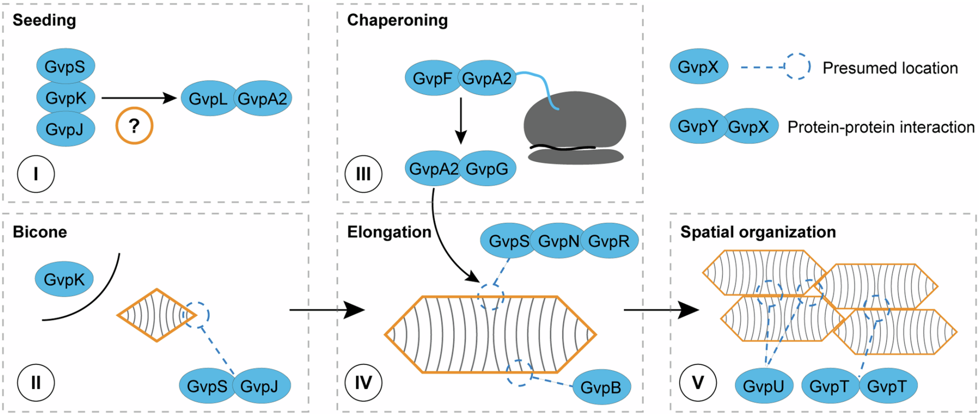

Figure 1.2: GV synthesis in 5 phases and, most common proteins involved and their hypothetical functions. reprinted from Iburg, M. *et al.* Elucidating the assembly of gas vesicles by systematic protein-protein interaction analysis. *The EMBO Journal* **43,** 4156–4172. ISSN: 0261-4189 (Oct. 2024)

and two archaeal phyla. Despite variations in size, their morphology is highly conserved, consisting of a cylindrical body closed at each end with conical caps. These structures are enclosed by a 2 nm-thick protein wall, whose hydrophobic interior excludes water molecules, creating a gas-filled space. This gas can diffuse across the wall via small pores. The genes encoding GV formation are typically organized in large clusters of around 10 genes. Among these, GvpA and GvpC are the most well-characterized. GvpA is the primary structural protein of the GV wall, while GvpC binds to GvpA on the cytosolic side, reinforcing the structure. Although the functions of other genes in the cluster remain incompletely understood, GV synthesis is thought to proceed in four to five stages: seeding, bicone formation, chaperoning, elongation, and spatial organization [17] (Figure 1.2).

The repurposing of GVs as ultrasound contrast agents by Shapiro et al. in 2014 [4] marked a pivotal moment for molecular ultrasound imaging. GVs overcome many of the limitations of microbubbles. Their nanoscale size allows for deeper tissue penetration [18], and their genetic encodability enables precise and versatile applications. GVs are structurally stable and can be used for harmonic (nonlinear) imaging. In addition to demonstrating proof of concept for GVs as contrast agents, this work revealed that clustering GVs enhances their echogenicity. In 2016, Lakshmanan et al. [19] advanced the field by demonstrating that the removal or mutation of GvpC significantly influences the nonlinear acoustic properties of *Anabaena* GVs. Removing GvpC reduces the stiffness of the GVs, enhancing their deformation during insonification. This increased deformation generates nonlinearities in the backscattered ultrasound signal, forming the foundation for this thesis: that GvpC engineering can be used to tailor GV acoustic properties for specific imaging applications. Research into GVs as ultrasound contrast agents has since branched into three main areas: the development of imaging technologies specific to GVs, the engineering of GVs as ultrasound reporter genes, and their use as injectable contrast agents.

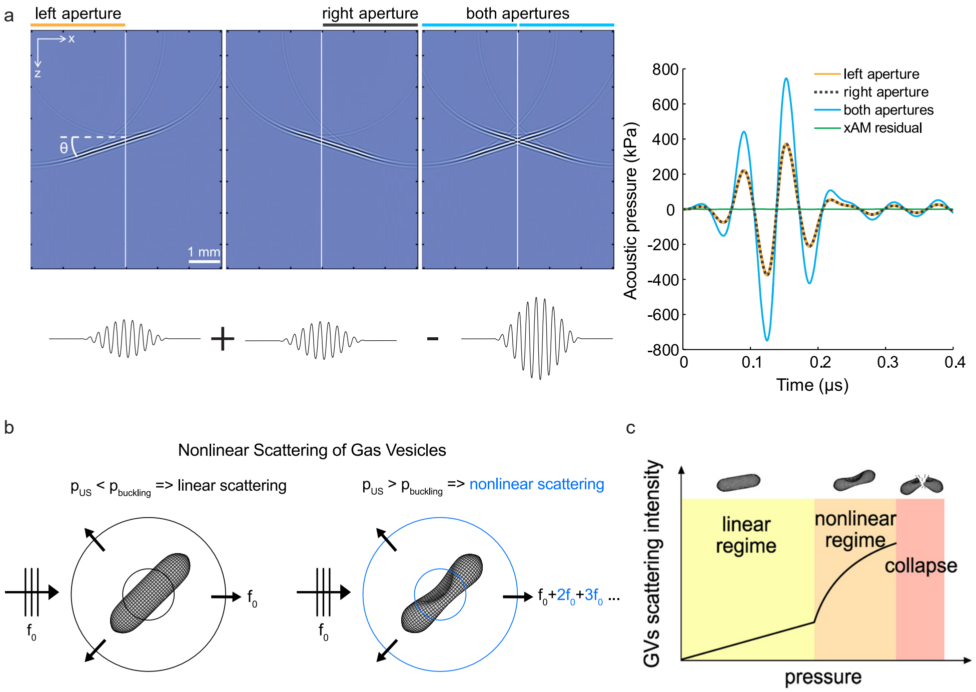

Figure 1.3: nonlinear contrast agent imaging principles. a, Three pulses, two with amplitude A and one with amplitude 2*A are fired. Shown in the top row is a cross-propagating plane-wave implementation. The xAM residual represents the non-linearity of the backscattered echo. b, Gas vesicles are susceptible to buckling and deformation through sufficient acoustic pressure. (a and b adapted from Maresca *et al.* [20], under license CC BY 4.0). c, scattering intensity of GVs versus the acoustic pressure. The buckling behaviour at higher acoustic pressures introduces non-linearity in the backscatter intensity and leads to increase contrast in nonlinear imaging modes. (adapted from Rabut *et al.* [21] under license CC BY 4.0).

GV IMAGING TECHNOLOGIES

From the outset, GVs were shown to be well-suited for harmonic imaging methods [4, 20, 22], similar to microbubbles. When exposed to high ultrasound pressures, GVs buckle and deform, altering the frequency content of the backscattered echoes [23, 24] (Figure 1.3). This creates a signal with increased energy in the higher harmonics. Isolating these higher harmonics enables GV-specific imaging modes. Beyond harmonic imaging, GVs also exhibit non-linear behavior in the fundamental frequency. Parabolic amplitude modulation (pAM) was developed to isolate this nonlinear signal [25]. In pAM, three ultrasound transmissions with different amplitudes are used, and their signals are combined mathematically to extract the nonlinear response (Figure 1.3c). However, this method introduces nonlinear propagation artifacts below the scatterers, caused by cumulative nonlinear wave interactions. To address this, X-wave amplitude modulation (xAM) was introduced [20], using angled plane waves to minimize artifacts (Figure 1.3a,b). Building on these methods, ultrafast AM (uAM) [21] combines coherent plane wave compounding with plane wave AM principles to achieve higher frame rates and greater imaging depth. While this approach sacrifices contrast and lateral resolution in comparison to pAM and xAM methods, it represents a significant advancement in imaging performance. For three-dimensional imaging, nonlinear soundsheet microscopy (NSSM) applies xAM principles to row-column addressed probes [9], creating a cross-sectional "soundsheet" for acoustic sectioning of living biological tissues labelled with GVs or microbubbles. Despite these advancements, nonlinear imaging methods are limited by low signal strength, which can hinder their application in scenarios where GV concentrations are low. This limitation is particularly pronounced in mammalian cells, which often produce only a few GVs per cell. To overcome this, Sawyer et al. [26] developed BURST imaging, which exploits the sharp signal increase caused by GV collapse under high ultrasound pressures. By isolating this dynamic signal, BURST imaging achieves a 1000-fold increase in sensitivity, enabling near-single-cell detection.

GVS AS ULTRASOUND REPORTER GENES

The genetic encodability of GVs sets them apart from conventional contrast agents. Similar to GFP in optical imaging, GVs can be used as acoustic reporter genes [5, 8, 10]. The first acoustic reporter gene (ARG1) was a chimeric cluster that combined GvpA and GvpC from *D. flos-aquae* with additional genes from *B. megaterium* [10]. Subsequent work identified additional clusters, such as bARGser, which produce GVs with significantly improved nonlinear contrast [8]. Through directed evolution, Nystrom et al. [27] engineered bARG710, encoding the most echogenic GVs to date. These reporter genes have been expressed in various organisms, including E. coli, gut bacteria [8, 28], mammalian tumor cells (HEK) [10], and T-cells [29] enabling applications ranging from tumor imaging to monitoring inflammation in vivo.

GVS AS INJECTABLE CONTRAST AGENTS AND BIOSENSORS

In addition to genetic applications, GVs can be used directly as injectable contrast agents. They can be purified from native hosts such as *B. megaterium, Halobacterium sp., and Serratia sp.*. In contrast to the use of ARGs, no genomically modified organisms are used in the production of the GVs, increasing the their suitability for translation to clinical diagnostics. Recent studies have shown that even non-elongated GV bicones can be imaged effectively [18]. The tiny size of these bicones allows them to effectively perfuse cancerous tissue through characteristic leaky vasculature, enabling specific tumor imaging without any type of targeted ligand. A particularly promising area of research involves engineering GvpC to create biosensors that respond to specific biomarkers. For example, a protease-sensitive GvpC variant was designed to cleave upon exposure to the corresponding protease, significantly increasing nonlinear contrast [11]. Similarly, a calcium-sensitive biosensor was developed by introducing a calmodulin recognition domain into GvpC [30]. Binding of calmodulin caused a subtle structural change, detaching GvpC from the GV shell and altering its acoustic properties.

THESIS OUTLINE

This thesis focuses on the development and demonstration of a novel gas vesicle (GV)-based biosensor for pH, an essential physiological parameter. The regulation of pH plays a fundamental role in maintaining the homeostasis of both intra- and extracellular environments in healthy organisms. Disruptions in pH balance are associated with a wide range of pathological conditions, including cancer, cardiovascular diseases, cerebrovascular damage, and ischemia-reperfusion injury [31–34]. These connections underscore the critical importance of understanding pH dynamics in both normal and diseased states. To address the need for accurate pH measurement, significant efforts have been devoted to developing imaging techniques capable of monitoring pH levels in living tissues. These efforts aim to measure pH within both intracellular and extracellular compartments with high spatial and temporal resolution. Optical imaging approaches have shown considerable promise for visualizing pH changes at the cellular level, leveraging fluorescence-based sensors and pH-sensitive dyes [35, 36]. However, optical methods are typically restricted to thin specimens due to their limited tissue penetration and are less effective for studying pH variations across larger cell populations or within entire organs. In contrast, MRI-based pH imaging offers a broader spatial range and excels at measuring extracellular pH changes. Despite this, MRI methods are inherently less effective for detecting intracellular pH variations due to their relatively low sensitivity and resolution [37–39]. Ultrasound imaging, augmented by the use of GVs as contrast agents, provides a novel and promising alternative for pH measurement. The nanoscale size and genetic encodability of GVs, combined with their ability to produce nonlinear ultrasound contrast, create a platform well-suited to address many of the limitations of existing imaging techniques.

In chapter 3, we present a high-resolution structural model of GVs derived from cryo-electron microscopy (cryo-EM). This model focuses on GVs without the reinforcement protein GvpC attached. By integrating the structural model with a conservancy screening of GvpC sequences, we propose a hypothetical folding and binding mechanism for GvpC. This work provides critical insights into the molecular architecture of GVs and forms the foundation for our engineering efforts to develop a pH-sensitive GV biosensor. The proposed GvpC binding model guides our mutagenesis experiments and biosensor design strategies.

In chapter 4, we detail the design, characterization, and validation of pHonon, the first GV-based pH sensor for ultrasound imaging. The design process leverages the atomic model of GVs developed in chapter 3 to identify potential mutation sites in GvpC. Mutations were selected based on their potential to confer pH sensitivity while preserving the essential structural features of GvpC. Specifically, we screened a subset of mutants containing histidine substitutions, chosen for their pH-dependent ionization properties. The results revealed surprising characteristics in pHonon's behavior, necessitating further investigation into the molecular mechanisms underlying its pH sensitivity. This chapter also presents the validation of pHonon as a functional ultrasound biosensor, with experiments conducted both in vitro and in vivo. These results demonstrate the utility of pHonon for non-invasive pH imaging and highlight its potential for applications in both basic research and clinical diagnostics.

In chapter 5, we explore an alternative approach to enhancing GV biosensor functionality, focusing on methods to aggregate GVs for improved ultrasound contrast. This strategy bypasses the need for extensive protein engineering by manipulating the physical arrangement of GVs. Aggregation is achieved through covalent binding, such as biotin-streptavidin interactions, or via depletion interactions that induce GV clustering. Notably, depletion interactions produce aggregates that are predominantly aligned lengthwise, significantly boosting nonlinear ultrasound contrast. We demonstrate that this approach can enhance both linear and nonlinear ultrasound signals in vitro. Additionally, we show that aggregation can enable nonlinear scattering from wildtype GVs, which are typically too stiff to undergo buckling under insonification. These findings suggest that aggregation-based methods may complement biosensor engineering efforts, offering a versatile tool for optimizing GV performance.

Finally, in chapter 6, we summarize the key findings of this work and discuss their implications for the broader field of biomolecular ultrasound imaging. This chapter reflects on the development and validation of pHonon, evaluating its potential applications and limitations. We also provide recommendations for future research directions, both specific to GV-based pH sensing and extending to other biosensor designs. These include the exploration of additional biomarkers, refinement of GV engineering strategies, and the development of complementary imaging techniques to further expand the capabilities of biomolecular ultrasound imaging.

2

THE ADVENT OF BIOMOLECULAR ULTRASOUND IMAGING

Ultrasound imaging is one of the most widely used modalities in clinical practice, revealing not only human prenatal development but also arterial function in the adult brain. Ultrasound waves travel deep within soft biological tissues and provide information about the motion and mechanical properties of internal organs. A drawback of ultrasound imaging is its limited ability to detect molecular targets due to a lack of cell-type specific acoustic contrast. To date, this limitation has been addressed by targeting synthetic ultrasound contrast agents to molecular targets. This ultrasound molecular imaging approach has proved to be successful but is restricted to the vascular space. Here, we introduce the nascent field of biomolecular ultrasound imaging, a molecular imaging approach that relies on genetically encoded acoustic biomolecules to interface ultrasound waves with cellular processes. We review ultrasound imaging applications bridging wave physics and chemical engineering with potential for deep brain imaging.

Heiles, B., **Terwiel, D.**, & Maresca, D. (2021). The advent of biomolecular ultrasound imaging. *Neuroscience* **474**, 122-133.

INTRODUCTION

Ultrasound imaging is used daily in clinical practice to assess the anatomical and physiological features of organs. Next to diagnostic applications in obstetrics and cardiology, we are witnessing a growing interest for ultrasound imaging in the field of neuroscience [40]. Transcranial ultrasound Doppler has been used for decades to assess the cerebrovascular function of major arteries of the brain [41]. In 2011, functional ultrasound neuroimaging (fUS) [1, 42] has been introduced as a breakthrough modality that relies on neurovascular coupling to map neuronal activity with a higher spatiotemporal resolution and portability than fMRI [43]. fUS has been used to track epilepsy crises in human neonates [44] or to delineate tumor-brain interfaces in neuro-oncology patients [45, 46]. More recently, a technique inspired by optical super-resolution named 3D ultrasound localization microscopy (ULM) has generated vascular maps of the living brain with a 30 microns resolution [47]. Unfortunately, these ultrasound imaging methods are not inherently sensitive to cellular and molecular processes.

To observe biological processes at the cellular scale, ultrasound engineers can now rely on endogenous, synthetic or biomolecular contrast agents (Figure 2.1) as vascular or intracellular reporters [40]. Red blood cells (RBCs) are a unique cell type that can be detected with high specificity thanks to their motion. RBC motion differs significantly from collective tissue motion and induces a phase shift in ultrasound signals [48] that can be captured to map blood vessels [49] (Figure 2.1A). Lipid-shelled microbubbles (MBs) are the main class of synthetic ultrasound contrast agents (Figure 2.1B). MBs scatter ultrasound more efficiently than RBCs thanks to their highly compressible gas core, and are administered intravenously to image blood perfusion [50]. MBs have also been engineered to target specific endothelial biomarkers [51]. The combination of ultrasound imaging with targeted MBs is the most established molecular ultrasound imaging strategy so far. In 2014, genetically encoded acoustic biomolecules called gas vesicles (GVs) have been introduced as ultrasound analogs to the green fluorescent protein [4, 52] (Figure 2.1C). GVs enable acoustic labeling of cells which opens the possibility of tracking cellular processes with ultrasound [53].

Endogenous, synthetic, and biomolecular ultrasound contrast agents enabled various molecular imaging applications such as ultrasound imaging of erythrocyte aggregation [54], ultrasound imaging of vascular endothelial growth factor (VEGF) [15], or ultrasound imaging of gene expression [10, 55]. GV engineering has also led to the development of acoustic biosensors that could be used across a wide spectrum of applications [11, 19]. This review article presents an overview of recent ultrasound technologies for deep imaging of the living brain. We cover recent ultrasound neuroimaging methods, ultrasound contrast agents used to interface with the brain, molecular imaging applications in the vascular space, and extravascular biomolecular imaging applications. Our focus is on methods to interface a penetrant form of energy – ultrasound waves – with cellular processes occurring in the brain. Light transmission based methods such as photoacoustics [56] are not discussed here.

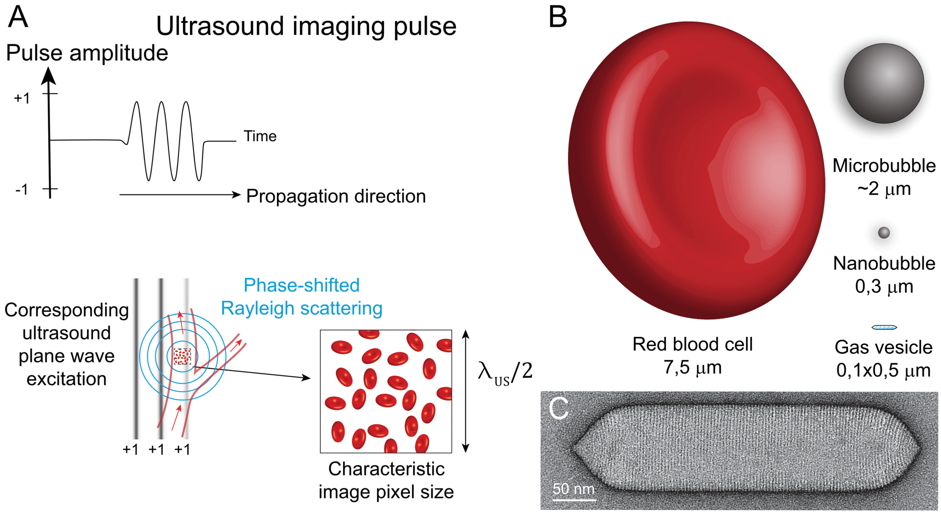

Figure 2.1: Contrast agents used in ultrasound neuroimaging. **(A)** Scattering of an ultrasound imaging pulse by red blood cells in motion. **(B)** Scale comparison of endogenous, synthetic and biomolecular ultrasound contrast agents. **(C)** Transmission electron microscopy image of a single gas vesicle.

RECENT ADVANCES IN ULTRASOUND NEUROIMAGING

Recent ultrasound neuroimaging methods rely exclusively on intravascular acoustic contrast (Figure 2.2). Neurovascular signals are separated from the gobal brain ultrasound backscatter thanks to their motion or their specific frequency content. In the mammalian brain, blood flow velocities range from several centimeters per second in major arteries [57] down to less than 1 mm/s in capillaries supplying neurons with oxygen [57]. At 15 MHz - a frequency often used for preclinical ultrasound imaging - the ultrasound voxel size is typically $10^6 \mu m^3$, which contains about 100 cortical neurons [58] or 10^5 RBCs in mice [59]. Ultrasound neuroimaging is therefore mapping the dynamics of cell populations rather than individual cells.

MAPPING CEREBROVASCULAR FUNCTION WITH ULTRAFAST ULTRASOUND DOPPLER IMAGING

With the introduction of high framerate plane wave ultrasound imaging, referred to as ultrafast ultrasound [66], ultrasound imaging can now capture thousands of images per second. This ultrasound imaging approach was originally proposed by Bruneel *et al.* [67] but only recently made possible thanks to modern multi-core computing architectures [66]. Instead of forming ultrasound images line by line, ultrafast ultrasound imaging relies on tilted plane wave transmissions to insonify brain tissues at kilohertz framerates [68]. Ultrafast ultrasound Doppler imaging (UDI) exploits these high framerates to achieve dense spatiotemporal sampling of RBC motion in tissue regions of interest. The UDI signal is a combination of blood scattering, tissue scattering, and noise. A critical problem in UDI

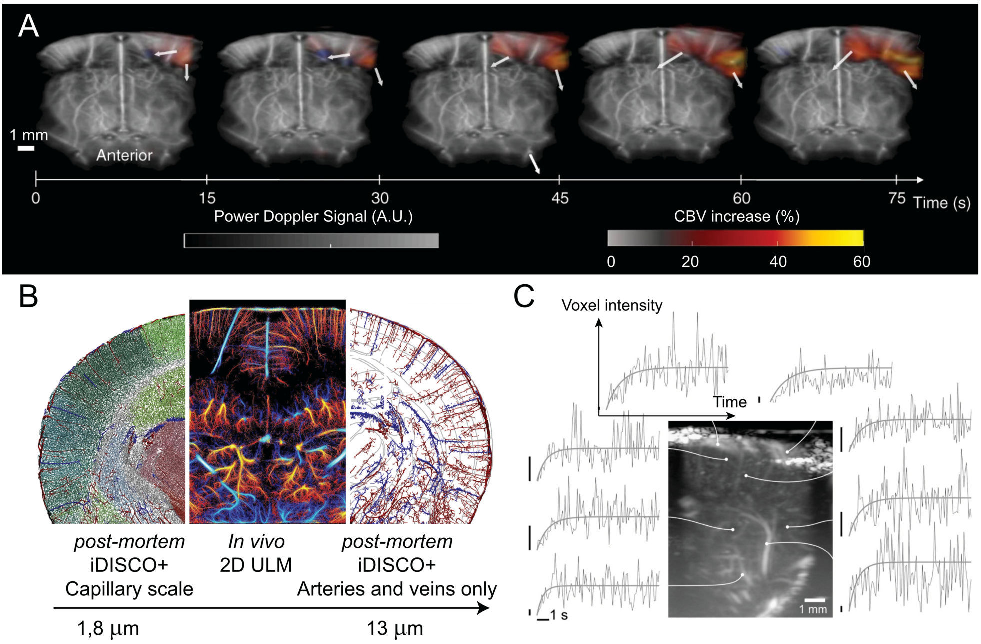

Figure 2.2: Emerging ultrasound neuroimaging methods. **(A)** 4D fUS imaging of the rat brain, adapted with permission from [42]. **(B)** ULM resolution compared to that of a post-mortem tissue clearing method (iDISCO+). Adapted with permission from [60]. **(C)** Temporal variations of cerebral hemodynamics measured by a nonlinear ultrasound imaging pulse sequence. Adapted with permission from [61]

is therefore to distinguish signal contributions arising from blood from signal contributions arising from other tissue types and noise. State of the art filtering approaches rely on spatiotemporal filtering of ultrafast ultrasound datasets [69].

Experimental comparisons have shown that UDI is 30 to 50 times more sensitive than conventional Doppler imaging [1]. This increase in sensitivity is key to capture blood flow variations in smaller vessels. UDI was successfully applied in a range of medical disciplines such as rheumatology [70], cardiology [71, 72], stroke imaging [73], or intensive care [72]. The capacity of UDI to map flow variations in small brain vessels led to the fus imaging breakthrough. fUS relies on neurovascular coupling that serves as an indirect readout of neural activity (like in fMRI) [1]. Since 2011, fUS imaging (Figure 2.2A) was reported in many animal models [40, 42], using experimental paradigms to study brain-wide circuits during sleep, active behavior, motor planning or recently optogenetic stimulation [74]. In a clinical setting, fUS imaging has been used to monitor neonates [75] and during tumor resection surgery [45, 46].

Contrast-free methods	Linear contrast-enhanced methods	Nonlinear contrast-enhanced methods
fUS imaging [42]	MB-enhanced fUS imaging [62]	AM and PI imaging of MBs and NBs [63]
	GV-enhanced fUS imaging [64]	AM and PI nonlinear Doppler imaging [65]
		x-AM imaging of GV [20]

Table 2.1: Overview of non-contrast and contrast-enhanced ultrasound neuroimaging methods. PI = pulse inversion, AM = amplitude modulation, x-AM = cross amplitude modulation.

MAPPING CEREBROVASCULAR ANATOMY WITH ULTRASOUND LOCALIZATION MICROSCOPY

Replacing fluorophores with MB contrast agents, and relying on the imaging speed of ultrafast ultrasound, Errico *et al.* [76] super-resolved the rat brain vasculature with a 10 μm precision ($\lambda_{US}/10$). This technique, referred to as ultrasound localization microscopy (ULM) [77] (Figure 2.2B), has also been used to visualize tumors [78], kidneys [79, 80], diabetes [81] and embryos [82]. 3D ULM was recently demonstrated in vitro [47] and in vivo in the rat brain [83]. A critical parameter in ULM is the ability to detect individual MBs. Initially, a frame to frame subtraction or a rolling background technique was used to subtract static echoes [84, 85]. This technique is hardly applicable in vivo because tissue motion can be important and out-of-plane, leading to inaccurate MB localization [47]. Spatiotemporal filters have been successfully used in this context as well to separated MB signals from tissue clutter [86]. Pixel oriented filtering methods such as the non-local means technique are also providing good results [82] (Song P, et al., 2018). Current ULM methods rely on MB motion. If MBs are targeted to endothelial biomarkers or stopped by a vascular occlusion, their ULM detection is no longer possible. This problem can be solved by relying on the unique nonlinear frequency content of MB echoes rather than on MB motion. Nonlinear ultrafast ultrasound imaging of MBs has been demonstrated [65, 87, 88] and lends itself well to ULM processing [89]. In this context, special attention must be given to MB destruction, especially when mapping targeted MBs for molecular imaging applications.

MAPPING BLOOD PERFUSION WITH NONLINEAR ULTRASOUND PULSE SEQUENCES

Several ultrasound pulse sequences dedicated to MB detection have been reported over the years. In neuroscience, van Raaij *et al.* [61, 90] showed that high-frequency nonlinear ultrasound imaging of MBs could capture rat brain activity evoked by forepaw stimulation (Figure 2.2C). A first class of pulse sequences relies on amplitude modulation (AM) of ultrasound pulses transmitted in tissues. Low amplitude ultrasound pulses elicit a linear response from MB and tissues, whereas high amplitude ultrasound pulses elicit a nonlinear response from MBs but not from tissues. The AM response of MBs is unique and differes from that of tissue. Ultrafast AM imaging has been used characterization of kidney and tumor perfusion [65]. A second class of ultrasound pulse sequences relies on the pulse inversion (PI) of ultrasound imaging pulses. In PI imaging, pairs of phase inverted pulses are transmitted into tissues and the echoes recorded are subsequently summed. This process retains nonlinear signatures that are unique to MBs circulating in tissues. Ultrafast PI imaging has been used to study blood perfusion [91]. A drawback of nonlinear ultrasound pulse sequences is their susceptibility to nonlinear propagation artifacts that misclassify tissues as contrast agents [92, 93]. This occurs when ultrasound waves travel through large inclusions of nonlinear contrast agents. Imaging methods based on cross-propagating plane waves are currently investigated and have shown to significantly reduce nonlinear propagation artifacts [92].

Endogenous, synthetic and biomolecular ultrasound contrast agents

Ultrasound waves are backscattered by microscale structures such as cells or ultrasound contrast agents. Individual particles with dimensions below a tenth of the wavelength ($\lambda_{US}/10$) are referred to as Rayleigh scatterers [94] and their reflective power is characterized by the scattering cross section σ_{Rs},

$$\sigma\_Rs \propto V_{Rs}^{2} f_{US}^{4}(((\kappa_{Rs}-\kappa_{0})/\kappa_{0})^{2}+(3((\rho_{Rs}-\rho_{0})/((2\rho)_{Rs}+\rho_{0})))^{2}) \tag{2.1}$$

with f_{US} the ultrasound wave frequency, V_{Rs} the volume of the Rayleigh scatterer, c_0 the speed of sound, κ_{Rs} and κ_0 the compressibility of the scatterer and of the surrounding medium respectively, ρ_{Rs} and ρ_0 the mass density of the scatterer and of the surrounding medium respectively. Equation 2.1 states that microscale particles exhibiting a density and/or compressibility contrast with surrounding tissue scatter ultrasound waves (Figure 2.1A). In addition, σ_{Rs} scales with ultrasound frequency to the power 4. An example is RBC contrast which is hardly visible at 1 MHz but easily detectable at 10 MHz and above [95]. Last, it is worth noting that Rayleigh scattering can also arise from structural inhomogeneities within cells such as genetically encoded GVs [10, 55, 96].

Red blood cells as indirect reporters of neuronal activity

While the acoustic contrast arising from RBCs does not inform directly on cellular or molecular events, it can measure functional hyperemia induced by neurovascular coupling [97]. In a recent study, Aydin *et al.* [98] reported that functional hyperemia measured with fUS imaging [1] is a robust reporter of underlying neuronal calcic activity. The hemodynamic response function (HRF) of the brain typically lags 2s behind the electric response [99]. The fUS HRF has been modeled as a gamma-distribution function with no post-stimulus undershoot [98]. It is therefore possible to exploit ultrasound backscattering induced by RBC motion to map neuronal activity with ultrasound.

Synthetic microbubbles and nanobubbles

MBs are the first and most widespread ultrasound contrast agents. Early developments aimed at controlling their scattering power as well as their stability [100]. Modern synthetic MBs are stable enough to pass through the heart and lungs, and their in vivo lifetime allows for multiple recirculations which lengthens the diagnostic window [101]. To stabilize MBs, a majority of them are now coated with a phospholipid layer, and their gas core is made of perfluorinated gases such as sulfur hexafluoride [102], perfluoropropane [103], or perfluorobutane [104, 105]. More than a dozen agents have now been commercialized with various technologies. Commercial MB diameters range from 0.5 to 10 λm [101] which lets them circulate in most vessels after intravenous injection (Figure 2.1B). The scattering power of MBs is directly linked to their size and ability to resonate at medical ultrasound frequencies [94]. Recently, monodisperse MB size distributions have triggered interest as these can boost MB echogenicity further [106]. MBs are too large to extravasate [107, 108]. In healthy vasculature, particles above 7 nm cannot pass through endothelial tight juctions [109]. In leaky cancer vasculature, particles as large as 380-780 nm were shown to extravasate [110]. This consideration triggered the development of nanobubble (NB) ultrasound contrast agents for cancer imaging [111, 112] and drug delivery [63, 80, 113]. Synthetic MBs can also be engineered to adhere to vascular biomarkers, creating the possibility for molecular ultrasound imaging of endothelial function. By adding targeting ligands to their shell, such as peptides, proteins, polymers, antibodies or aptamers, targeted MBs capable of sensing inflammation (with ICAM-1, VCAM-1, E-selectin, P-selectin) [114, 115], angiogenesis (with $\alpha_v\beta_3$ integrin, VEGF, VEGFR2, endoglin) [116–118] or thrombosis (cRGD) [119, 120] have been created. Increasing the sensitivity of molecular ultrasound imaging with monodisperse MBs would be particularly valuable as just a fraction of targeted MBs end up binding to endothelial markers [121–123]. Finally, Nakatsuka *et al.* [124] demonstrated that it was possible to engineer MBs that become reflective only when levels of thrombin are significant but remain dormant in normal physiological conditions.

ACOUSTIC BIOMOLECULES

The adoption of molecular ultrasound imaging based on MBs remains limited because of MB size, intravascular confinement, and in vivo half-life [15, 125]. Recently, GVs were introduced as a new class of genetically encoded ultrasound contrast agents that have the potential to become the “GFP for ultrasound” [40]. GVs are ancient hollow protein nanostructures evolved as motility devices by aquatic microorganisms to regulate their buoyancy (Figure 2.3A). In 2014, Shapiro *et al.* realized that the gas content of GVs would make them bright in ultrasound images. The GV nanostructure consists of two proteins. GV protein A (GvpA) forms the spindle-shaped backbone structure and GV protein C (GvpC) binds externally to GvpA and stiffens the assembled GV [126].

Both linear and nonlinear ultrasound imaging of GVs has been reported in literature [4, 23, 127]. Nonlinear GV scattering is thought to arise from large GV shell deformations referred to as buckling [128]. At medical ultrasound frequencies, buckling behavior occurs above an acoustic pressure of a few hundreds of kPa range and is particularly suited to AM ultrasound [128]. Thanks to their biogenic origin, GVs lend themselves to molecular and genetic engineering (Figure 2.3). The acoustic properties of GVs have been successfully manipulated by altering GvpC binding to GvpA. Complete GvpC removal was shown to weaken GVs and increase their nonlinear scattering [19, 128]. GvpC removal is also lowering GV collapse pressure. This characteristic was leveraged to engineer acoustic

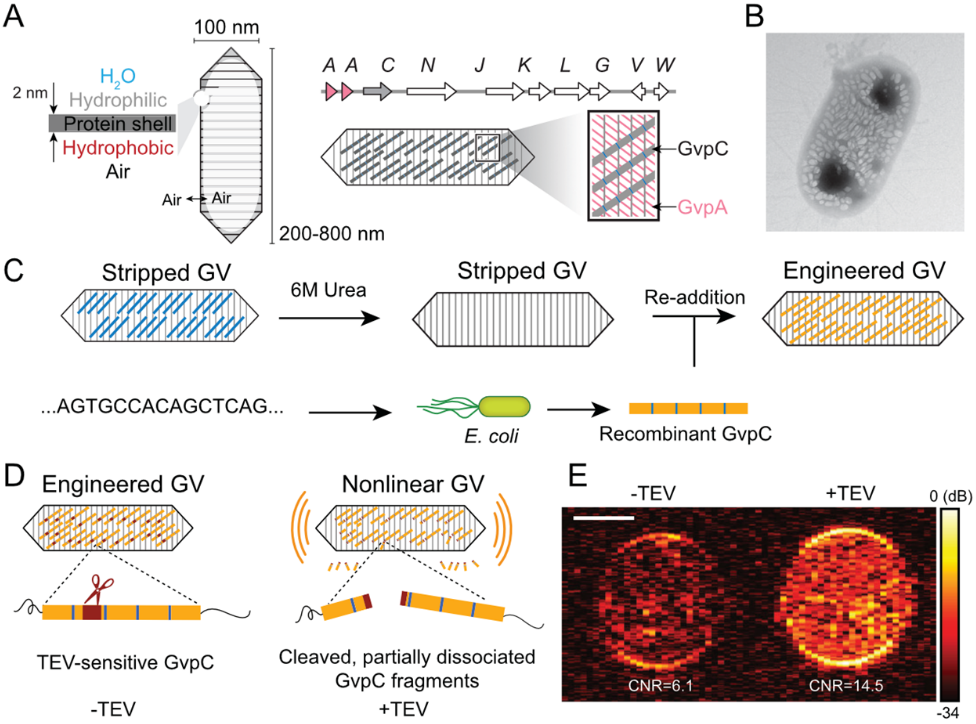

Figure 2.3: Engineering of acoustic biomolecules. (A) GV hollow protein nanostructure, gene cluster encoding GVs and surface arrangement of the GV shell proteins GvpA and GvpC. Adapted with permission from [20]. (B) Heterologous expression of gas vesicles in E.coli. Adapted with permission from [10]. (C) GvpC bioengineering pipeline, adapted with permission from [20]. (D) Design of an acoustic biosensor of Tobacco Etch Virus (TEV) protease activity. Adapted with permission from [11]. (E) Nonlinear ultrasound imaging of acoustic biosensors of TEV activity. Scale bar, 1mm. Adapted with permission from [11].

reporters with distinct acoustic collapse pressures and used for multiplexed imaging [19]. Specific biomarkers can also be bound to to the outer wall of GVs, following the example of targeted MBs. In summary, GvpC provides a convenient handle for GV shell functionalization.

MOLECULAR ULTRASOUND IMAGING USING VASCULAR AGENTS

TARGETED MBS AS ACOUSTIC REPORTERS OF ENDOTHELIAL FUNCTION

Many vascular inflammation diseases and types of cancer are characterized by differential expression of endothelial biomolecules. Targeted MBs have been successfully used to bind to multiple membrane proteins such as P- and E-selectin, VCAM-1 and ICAM-1, locally enhancing imaging contrast in diseased areas [125, 129, 130]. In practice, ultrasound imaging with targeted MBs requires a significant difference in concentration between bound and unbound MBs. A 5-10 minutes window after intravenous injection is enough for the reticuloendothelial system to clear non-functionalized MBs from the bloodstream. MB clearance is also in part due to acoustic collapse or gas diffusion through the MB phospholipid shell [131]. A vast majority of methods for discerning bound and freely circulating microbubbles rely on destruction-replenishment strategies. In destruction-replenishment methods, MBs are first destroyed using a high-intensity ultrasound pulse. The subsequent signal is assumed to be arising from freely-circulating MBs and can be subtracted from the initial signal that accounts for both bound and unbound MBs [132]. Molecular ultrasound imaging using targeted microbubbles has been recently combined with ULM to co-localize vascular anatomy and vascular markers of angiogenesis [89] (Figure 2.4A). This promising multimodal approach could be used to study longitudinal cancer development and vascular remodeling in living organisms.

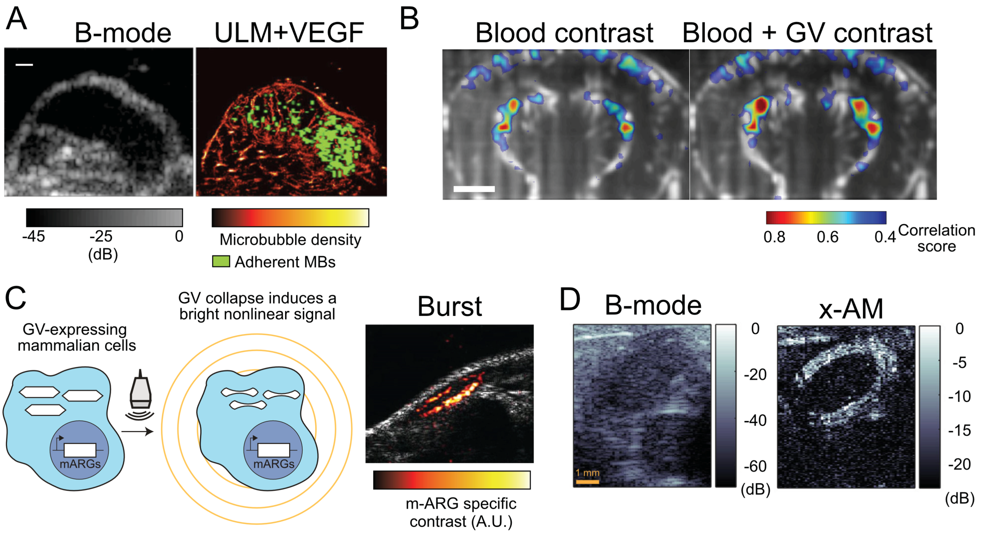

Figure 2.4: Biomolecular ultrasound imaging in mouse models. (A) Molecular ultrasound imaging of Vascular Endothelial Growth Factor (VEGF) expression using targeted microbubbles (MBs), and co-registered with ULM imaging of vascular anatomy in a mouse tumor model. Scale bar, 1mm. Adapted with permission from [89]. (B) Transcranial GV-enhanced fUS imaging of the mouse brain. Scale bar, 1mm. Adapted with permission from [64]. (C) Ultrasound imaging of gene expression in a mouse tumor model using a GV-collapse based approach. Image width 9 mm. Adapted with permission from [55]. (D) Nonlinear cross-amplitude modulated (x-AM) imaging revealing the presence of GVs in the gastrointestinal tract of a mouse. Adapted with permission from [20].

GV-ENHANCED HEMODYNAMIC FUS IMAGING

GVs were recently investigated as hemodynamic enhancers for sensitive transcranial fUS imaging in mice [64] (Figure 2.4B). This study constitutes a first step towards biomolecular fUS imaging of neural activity. Purified GVs were used as linearly scattering nanoparticles circulating alongside RBCs, increasing the overall blood backscatter and raising the sensitivity of Doppler methods. A first finding was that thanks to their nanoscale, inherent stability, and large numbers in circulation, GVs-enhanced UDI could measure slow flow velocities more accurately than conventional UDI and MB-enhanced UDI [64]. One possible explanation is that unlike MBs, GVs are dominated by Stokes drag over other forces such as buoyancy. The capacity of GVs to enhance Doppler signals down to 50 μm/s flow velocities is critical to map the neurovascular coupling in the smallest vascular compartments [97]. A second finding was that intravenous bolus injection of GVs did enhance ultrafast Doppler signals in the mouse brain. While the peak enhancement provided by GVs was inferior to that of MBs (+34% compared to baseline level for GVs and +149% for MBs), GVs yielded a significantly smoother Doppler signal enhancement (the mean variance of the fast time fluctuation of the GV-enhanced Doppler signal was 0.8% compared to 4.5% for the MB-enhanced Doppler signal). A third finding was that bolus injections of GVs provided a pseudo-steady transcranial enhancement of fUS signals over the course of 4 minutes in mice, whereas bolus injections of MBs deteriorated the quality of brain activity maps. In the future, a comparison of different modes of administration (bolus versus infusion) and a broader range of doses would help optimize this imaging approach. It is worth noting that in contrast-free fUS imaging, the percent change in fUS signals at 15 MHz is lower in mice (5%) [74] than in rats (15%) [42] for a given brain stimulation protocol (e.g. whisker stimulation). This might be due to differences in RBC volume - 45.5 μm^3 in laboratory mice [133] versus 60.7 μm^3 in laboratory rats [134]. This justifies the need for method capable of enhancing fUS sensitivity in mice. The benefit of GVs at lower ultrasound frequencies and in larger brains remains to be demonstrated. In any case, efforts to engineer brighter GVs will be beneficial across medical ultrasound frequencies [135]. Together these results demonstrated that GVs could become a preferred contrast agent for fUS imaging thanks to their noise-free enhancement of fUS signals across a wide range of cerebral blood flow velocities.

Imaging with engineered red blood cell contrast

An interesting strategy to couple molecular events to hemodynamic fUS imaging could be to artificially trigger vasodilatory responses in the brain using vasodilating peptides [136, 137]. Using fMRI, Desai *et al.* [136] showed that nanomolar concentrations of the cgrp peptide induced larger cerebral flood flow variations than neurovascular coupling. Since fUS imaging measures local blood flow variations in the brain, molecular ultrasound imaging combining fUS and vasoactive peptides could be envisioned. Another interesting chemical engineering approach consists in using RBC membranes to “hide” ultrasound contrast agents from the immune system [138] and increase the contrast agent circulation time [139]. RBCs can circulate in the bloodstream for several months whereas the lifetime of MB circulation is of the order of 10 minutes and prevents longitudinal experiments. Contrast-enhanced transcranial fUS imaging methods would greatly benefit from long circulating contrast agents [62, 64].

Biomolecular ultrasound imaging applications

Ultrasound imaging of gene expression

GVs are the first genetically encoded acoustic biomolecules and could become the “GFP for Ultrasound” [40]. GVs are encoded by highly conserved genetic clusters of 8 to 12 genes in microorganisms such as *Anabaena flos-aquae* [92]. Two of these genes encode for the structural proteins GvpA and GvpC that are the main constituents of GV nanostructures. Fully assembled GVs present a 2 nm-thick shell made of periodic repeats of the single protein GvpA which is further reinforced with the external scaffold protein GvpC. In 2018, Bourdeau *et al.* [10] demonstrated heterologous expression of GVs in *Escherichia coli* (*E. Coli*) (Figure 2.3B) and *Salmonella typhimurium*, making these engineered cells visible with ultrasound imaging. In addition, Bourdeau *et al.* [10] reported ultrasound imaging of bacteria in the gastrointestinal (GI) tract of mice, a first demonstration of cell tracking with ultrasound. Interestingly, GV-expression in *E. Coli* is also creating the possibility for high-throughput screening of engineered echogenic bacterial phenotypes [10, 135]. In 2019, Farhadi *et al.* reported genetic expression of GVs in mammalian cells. Their study showed that acoustic contrast arising from GVs and occupying less than 0.1% of the cytoplasm could be detected using a destructive template-based ultrasound imaging sequence named BURST. Using this approach, they reported depth-resolved ultrasound imaging of GV expression in a subcutaneous tumor model (Figure 2.4C). In the future, ultrasound imaging of mammalian acoustic reporter genes (mARGs) using nondestructive methods such as cross amplitude modulation [20] should emerge (Figure 2.4D). The development of mARGs is still in its infancy and research efforts are needed to facilitate targeted GV expression in various cell-types using viral vectors. In neuroscience, a potential application could be to drive GV-expression with neural activity-dependent promoters such as Arc, fos or E-SARE [140] to observe time integrated neural responses in the brain. A second exciting route is to engineer GVs into acoustic intracellular sensors to study dynamic cellular processes deep into brain tissues.

ACOUSTIC BIOSENSORS FOR DEEP MOLECULAR ULTRASOUND IMAGING

Following the discovery of GFP, fluorescent proteins were further engineered into genetically-encoded indicators to investigate biological processes at the cellular scale. In neuroscience, genetically encoded calcium and voltage indicators are now established tools to study cognition in animal models. Lakshmanan *et al.* [19] showed that the acoustic response of GVs could be shifted from linear to nonlinear by removing GvpC (Figure 2.3C), a first critical step towards the development of an acoustic biosensor. In 2020, they reported the first genetically encoded acoustic biosensor with tunable nonlinear constrast in response to protease activity (Figure 2.3D). To do so, they inserted a short recognition sequence for the model Tobacco Etch Virus (TEV) endopeptidase into one of the GvpC repeats. They observed that GVs covered with TEV-sensitive GvpC were weakened in the presence of TEV, which led to increased nonlinear ultrasound scattering (Figure 2.3E). Similar results were obtained for two other acoustic biosensor designs, one based on the calcium-activated calpain protease, and the other on a degradation tag appended to the C-terminus of GvpC (model proteosome ClpXp). These acoustic biosensors were successfully expressed in probiotic bacteria and imaged in the mouse GI tract. In neuroscience, proteases are involved in various aspects of neuropathophysiology. For example, intracellular proteases such as calpain and caspases get involved in neuronal dysfunction in Alzheimer's disease. A current limitation is that acoustic biosensors based on GvpC degradation are not reversible and cannot report on dynamic intracellular processes. The feasibility of fast and reversible acoustic biosensors conceptually similar to GCamP [141] remains an open research question.

ULTRASOUND IMAGING OF PHAGOLYSOSOMAL FUNCTION

Next to genetic expression of mARGs, purified GVs can be used as injectable to report on cellular activity. In a proof-of-concept study, Ling *et al.* [142] used GVs to image liver macrophage phagolysosomal function with ultrasound. After intravenous injection, purified GVs get cleared from the bloodstream by liver macrophages that recognize them as foreign particles. Next, phagocytosed GVs undergo lysosomal degradation. This process was monitored byLing *et al.* using two different ultrasound imaging modes. UDI was used to track GV circulation in brain vessels over time. A sharp increase in UDI intensity was observed 100 s after injection before decreasing over time due to GV retention in the liver. The GV circulation half-life was equal to 230 s. In parallel to UDI, the accumulation of GVs in liver macrophages was monitored using AM ultrasound imaging. AM signals peaked 10 minutes after injection, before to decrease decrease due to lysosomal degradation of GVs. Together, these results showed that ultrasound imaging of phagocytosis and lysosomal degradation rates could be used to diagnose healthy versus diseased liver states in humans. In neuroscience, purified GVs could be used as injectable to report on cerebrovascular afflictions such as ischemia-reperfusion injuries, atherosclerosis, or brain tumors.

OUTLOOK AND OPPORTUNITIES IN NEUROSCIENCE

The field of biomolecular ultrasound imaging was born in 2014 with the introduction of GVs as genetically encoded ultrasound contrast agents. GVs have now been used as acoustic reporters genes in bacteria and mammalian cells, engineered into acoustic biosensors of protease activity, and vascular reporters for transcranial functional ultrasound neuroimaging or imaging of macrophage phagolysosomal function. Next to the introduction of GVs, the field of ultrasound neuroimaging has witnessed major developments. In 2011, functional ultrasound neuroimaging was established as a breakthrough modality that can map brain activity where fMRI fails: in freely moving animals, human neonates, and during intraoperative brain surgery. In 2015, ultrasound localization microscopy was reported as a super-resolution method capable of mapping the whole brain-wide vasculature of living mammals with a 10 μm resolution. In 2018, a new nonlinear ultrasound pulse sequence enabled depth-resolved, nondestructive tracking of GVs in the GI tract (Figure 2.4D). The combination of these methods with endongenous, synthetic and biomolecular ultrasound contrast agents will create new opportunities for deep molecular imaging of the brain at work. Clinical use of biomolecular ultrasound technologies is far ahead, but two translational paths can be envisioned. The first is cell-based. Genetically modified cell agents such as CAR T cells are already sent in the human body to fight cancer [143]. These cells could augmented with the capacity to produce their own acoustic contrast and enable ultrasound monitoring of immune cell therapy. From a regulatory point of view, potential immune responses to GVs - bacteria-derived proteins – will need to be investigated. The second path consists in using GVs as purified nanoparticles administered intravenously. A potential application could be to sense cancer microenvironments with acoustic biosensors. Here again, future studies must be conducted to investigate potential immune reactions. Bridging the fields of chemical engineering and acoustics, biomolecular ultrasound imaging will certainly lead to a wave of discoveries in neuroscience.

3

CRYO-EM STRUCTURE OF GAS VESICLES FOR BUOYANCY-CONTROLLED MOTILITY

Gas vesicles are gas-filled nanocompartments that allow a diverse group of bacteria and archaea to control their buoyancy. The molecular basis of their unique properties and assembly remains unclear. Here, we report the 3.2 Å cryo-EM structure of the gas vesicle shell made from the structural protein GvpA that self-assembles into hollow helical cylinders closed off by cone-shaped tips. Two helical half-shells connect through a characteristic arrangement of GvpA monomers, suggesting a mechanism of gas vesicle biogenesis. The fold of GvpA features a corrugated wall structure typical for force-bearing thin-walled cylinders. Small pores enable gas molecules to diffuse across the shell, while the exceptionally hydrophobic interior surface effectively repels water. Comparative structural analysis confirms the evolutionary conservation of gas vesicle assemblies and reveals molecular details of shell reinforcement by GvpC. Our findings will further research into gas vesicle biology, and facilitate molecular engineering of GVs for ultrasound imaging.

Huber, S. T., **Terwiel, D.**, Evers, W. H., Maresca, D., & Jakobi, A. J. (2023). Cryo-EM structure of gas vesicles for buoyancy-controlled motility. Cell, 186(5), 975-986.

3.1. Introduction

Microorganisms utilize active motility systems to move towards or away from a variety of environmental stimuli such as chemicals and light [144]. These include swimming by rotation of rigid flagella; and movement over solid surfaces with filamentous appendages [145]. Other forms of motility do not rely on active propulsion. Aquatic bacteria and archaea have evolved mechanisms to regulate buoyancy and can – similar to ballast tanks in submarines – create and eliminate gas-filled compartments to allow vertical migration in the water column. The cellular compartments providing positive buoyancy are formed by gas-filled protein shells called gas vesicles (GVs) [126].

There are very specific requirements for such structures: to achieve net buoyancy, GVs must occupy a substantial proportion of the cell, which involves forming compartments that extend over hundreds of nanometers in size. To maximize buoyancy the shell must be constructed from minimal material. At the same time, the shell needs to provide resistance to hydrostatic pressure to maintain buoyancy with changes in water depth [146].

GVs have therefore evolved as rigid, thin-walled structures composed of a single protein unit that typically polymerizes into large cylindrical shells closed off by conical tips [147, 148]. The shell allows gas to diffuse passively between the GV lumen and the surrounding liquid, while effectively repelling water [149]. All GVs identified to date appear to be constructed from the same components [150]. The 7 kDa primary gas vesicle protein GvpA forms the core of the GV shell and the cone-shaped tips. A second protein, GvpC, binds the exterior of the gas vesicle and provides additional structural reinforcement [16, 151].

With molar masses exceeding hundreds of MDa, GVs range among the largest protein-based macromolecular assemblies reported to date. Despite intensive efforts [147, 152–158], the molecular structure of GVs and therefore a molecular-level understanding of their distinctive properties have remained elusive. Here, we present the cryo-EM structure of the canonical gas vesicle shell, providing detailed insight into the biogenesis of GVs and the unique evolutionary adaptions that enable buoyancy-controlled motility.

3.2. Results

Cryo-EM structure of the gas vesicle wall

We expressed and purified *B. megaterium* GVs that form narrow tubes most suitable for cryo-EM analysis (Figure 3.1). The small diameter enables preparation of samples with thin ice to maximize contrast and reduces the propensity of GVs to deform from ideal cylindrical shape. The native *B. megaterium* GV gene cluster contains two almost identical GvpA homologs, named GvpA and GvpB; for consistency in naming convention, we will refer to them as GvpA1 and GvpA2. A minimal gene cluster including GvpA2 but lacking GvpA1 is sufficient for GV assembly in E.coli [159, 160] (Figure 3.1A). Cryo-EM images showed GVs forming 0.1-1 μm long cylinders with varying diameters (55±7 nm), consistent with previous data [161]. A subset of images (16%) contained GVs with diameters as small as 34-42 nm (Figure 3.1B) which had their cylinder shape best preserved in the thin liquid film of cryo-EM samples (Figure 3.1B-F).

We used a combination of 2D and 3D classification techniques to select 4% of the small GV subset corresponding to 35.6 nm diameter (Figure A1) and used helical recon-

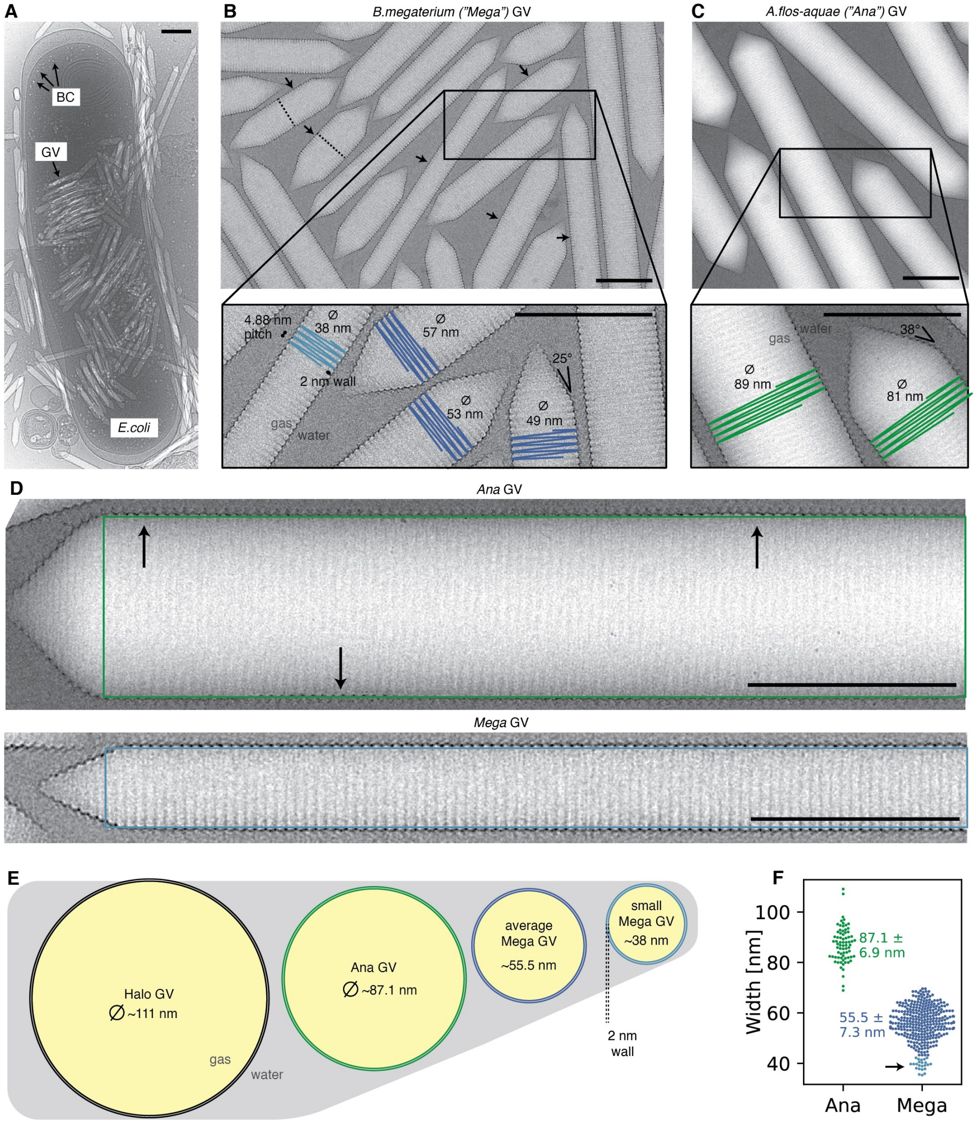

Figure 3.1: Gas vesicles. (A) Cryo-EM micrograph of an *E. coli* cell heterologously producing *B. megaterium* gas vesicles (GVs). Mature GVs and small bicone (BC) nuclei are visible inside bacteria and in the surrounding medium. (B) Cryo-EM micrograph of purified *B. megaterium* GVs. GVs appear brighter than the surrounding solvent due to the lower density of the GV-contained gas. Dashed lines on a subset of GVs represent midpoints of the helical GV segment; arrows indicate the location of the seam. The inset shows close-up examples of average-sized GVs (blue) and a small diameter GV (light-blue) used for structure determination. The 48.8 Å helical pitch, the 2 nm thick wall and the 25° cone angle are annotated. See also Figure A4.

struction to obtain a cryo-EM density of 3.2 Å resolution (Figure 3.2). The final reconstruction yielded a cylindrical GV shell assembly with 93 GvpA2 monomers per helical turn, which represents one member of a range of helical polymorphs with diameters ranging from 34 to 70 nm and with 90 to 183 monomers per helical turn.

The reconstructed density allowed de novo atomic model building of GvpA2 in the structural context of its native assembly (Figure 3.2, Table A1). The cylindrical shell is constructed from thousands of GvpA2 monomers polymerized side-by-side into ribs spiraling into a left-handed helix with a helical pitch of 48.8 Å and -3.87° helical twist, resulting in 92.93 GvpA2 units per helical turn (Figure 3.2A-B). Contrary to postulated models[155, 157], GvpA monomers and not antiparallel dimers form the repeating units of the helical assembly. GvpA2 adopts a coil-α-β-β-α-coil fold (Figure 3.2A-B). The carboxyl-terminal residues Asp67-Ile88 are flexible and not resolved in our structure. The helical lattice forms an array of ribs consisting of densely packed GvpA2 subunits with a lateral center-to-center distance of 12 Å. The central β-hairpin, tilted at -36° relative to the long axis of the cylinder, forms the core of the GV ribs. Helix α2 folds back onto the hairpin, and helix α1 forms a bridge across the 16 Å gap separating adjacent ribs. The GV wall is therefore only one or two peptide layers thick (Figure 3.2B). The inner wall of the GV shell forms a continuous hydrophobic surface consisting of a dense pattern of hydrophobic residues located on the luminal side of the β-hairpin and helix α1 (Figure 3.2C-D). Connections between the ribs of the GV shell are formed by the predominantly polar N-terminus, which extends perpendicular to helix α1 and folds across the β-hairpin of the adjacent rib, stabilized by interactions with several residues in the β-hairpin and helix α2 (Figure 3.2E).

The extreme hydrophobicity of the luminal GV surface constitutes an energetic barrier for diffusion of liquid water or condensation of gaseous H_2O. Consistently, GVs have been shown to be impermeable to water but to be highly permeable to gas molecules [149]. How gas molecules passage through the GV wall has so far been unknown. We located pores in the GV shell formed by slit-like openings between α1-helices of adjacent GpvA2 monomers (Figure 3.2F). We quantified the resulting pore size in the GV assembly computationally using Voronoi diagrams [162] and retrieved three different access routes with minimal constrictions ranging from 2.4 - 3.8 Å, compatible with the collisional cross-sections of gases dissolved in the cytosol (Figure 3.2F) [163].

Despite its limited thickness, the GV shell can resist several atmospheres of pressure without collapse [146]. GvpA2 monomers are held together tightly by lateral connections along the GV ribs formed by an extensive hydrogen-bonding network between the β-strand backbones (Figure 3.2G). The hydrogen bonds are oriented at an angle of 54° relative to the cylinder axis, which is close to the "magic angle" 54.7° at which transverse and longitudinal stresses are equal in the wall of a cylinder [126, 164]. Additional reinforcements are made by a continuous network of salt bridges formed by Glu43-Arg31 between two monomers and Arg31-Glu38 within a monomer. The GvpA2 shell consists of alternating line segments and triangular cross-sections providing force-bearing elements (Figure 3.2E). The corrugations increase stiffness along the rib direction, while the linear segments provide compliant hinge elements that increases elasticity of GVs, increasing their capacity to accommodate deformations orthogonal to the rib without collapse [165].

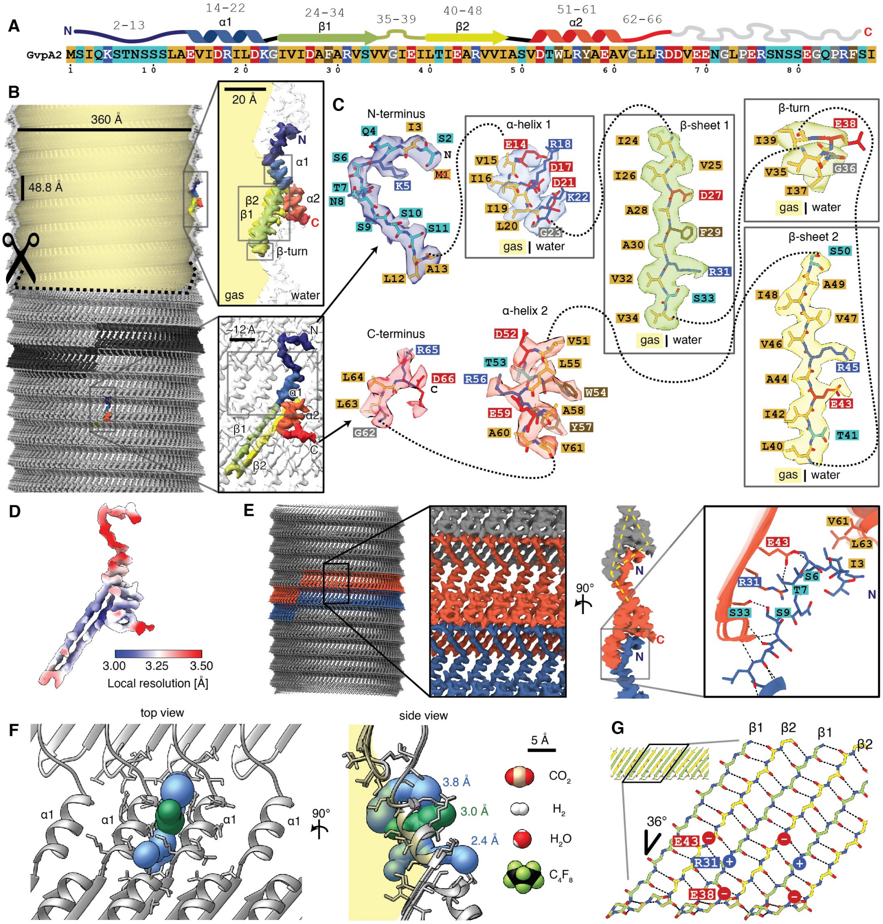

Figure 3.2: Cryo-EM structure of the gas vesicle wall. (A) Primary and secondary structure of *B. megaterium* GvpA2. Residues in the primary structure are colored based on physicochemical properties. (B) GvpA2 monomers form thin-walled gas-filled protein shells assembled into a left-handed helix. One individual rib formed by 93 monomers is highlighted in dark gray. The top part of the GV is cut open to visualize the gas space. The 3.2 Å resolution cryo-EM density is shown with a single monomer colored according to sequence (N-terminus blue, C-terminus red) from a side-view (top inset) and front-view (bottom inset). (C) Entire cryo-EM density of a monomer annotated with respective amino acid one-letter codes and the atomic model. Aliphatic residues (Ala, Val, Leu, Ile) line the gas-facing side of the GV wall. (D) Estimate of local resolution. (E) Cryo-EM density of the GV wall with two ribs highlighted in orange and blue. Side-view illustrating corrugated zig-zag structure and triangular cross-sections of the wall (yellow lines). Close-up of inter-rib interactions mediated by the N-terminus (blue), which binds across the β-hairpin and the C-terminus (orange) of adjacent ribs, stabilized by hydrogen bonds from backbone and side chains (Ser6, Thr7, Ser9) and hydrophobic contacts (Ile3). (F) A slit between $\alpha 1$ helices allows diffusion of gas through the wall. Three computed tunnels approximate the slit and have bottleneck sizes ranging from 2.4 to 3.8 Å. The van-der-Waals surfaces of several gas molecules known to diffuse through the wall are shown to scale, with perfluorocyclobutane being the largest with 6.3 Å collision diameter. (G) Schematic of the β-strand rib providing the majority of lateral connections for the assembly through backbone hydrogen bonding (dotted lines) and electrostatic interactions (Glu43-Arg31-Glu38).

GAS VESICLES CONSIST OF TWO HALF-SHELLS WITH INVERTED ORIENTATION

The thin film of the cryo-EM sample orients the large GVs into a sideways orientation, providing a consistent viewing direction onto the GV edges in projection. Detailed inspection of gas vesicles edges revealed that GvpA2 monomers are always oriented with their β-turns pointing towards the center of the GV cylinder (Figure 3.3A), which contains a structural irregularity that has previously been referred to as a seam [153]. 2D class averages of GV edges around this seam showed two oppositely oriented GvpA2 monomers that make contact via their β-turns (Figure 3.3A, Figure A2A) implying that this is the contact site of two GV half-shells with inverted orientation.

While two contacting cylinders or cones have the same contact geometry along the entire circumference, GVs are assembled from two contacting helices. Continuity of the helicity implies there must be a unique polarity reversal point (PRP) at a point along the circumference, where an upwards and a downwards-oriented GvpA2 monomer meet side-by-side. Apart from classes showing contacting β-turns, there is one less frequent set of 2D classes of the seam that displays two overlapping GvpA2 monomers in inverted orientation (Figure 3.3A, Figure A2B). We posit that this 2D class is a projection view of the PRP located at the GV edge. As GVs can freely rotate around the cylinder axis in the thin ice layer, the PRP will be located exactly at the edge only at special rotation angles, explaining why this class is observed less frequently. The mirror symmetry in the 2D class implies a viewing direction perpendicular to a 180° (C2/D1) rotation axis (Figure A2C) that points through the PRP.

Using restraints from our 3D reconstruction and 2D class averages, we constructed a pseudo-atomic model of a GV half-shell. Starting at the PRP, we extended the model from the D1 symmetry axis using the known helical symmetry for the cylindrical part of the GV shell and allowed transitioning into the conical tips by linearly decreasing the radius set by the 25° semi-angle of the cone and while refining structural adaption of GvpA monomers at defined hinge-points to match the experimental data (details in Methods and Figure A3). We then duplicated the half-shell by rotating around the D1 axis, leading to a complete GV model consisting of 1730 monomers and a total molecular mass of 12.2 MDa. Simulated density projections from this model closely match the experimental 2D classes (Figure A2D-E).

MOLECULAR MECHANISM OF GAS VESICLE BIOGENESIS

Our pseudo-atomic model of the GV assembly shows that half-shells interact through contacts at the GvpA β-turns around the circumference of the seam, as well as at the PRP where the GvpA2 rib reverses its polarity (Figure 3.3C). The pattern of side-by-side contacts between β-sheets of GvpA2 monomers (d=d=d=d) along a rib is identical everywhere except at the PRP, where β-hairpins align inversely (d=d-p=p). The PRP is therefore a unique point in the GV assembly that may be recognized by the molecular machinery that facilitates GV growth, and is likely the point at which new GvpA molecules are inserted during GV growth. Expansion of the GV assembly could occur either by inserting two oppositely oriented monomers, leading to symmetric expansion of both GV half shells; or by stochastic insertion of monomers into either half shell. If GV growth occurs by insertion of dimers, the PRP should always be located exactly at the midpoint of the cylindrical segment. Instead, we observe that the PRP can be located away from the

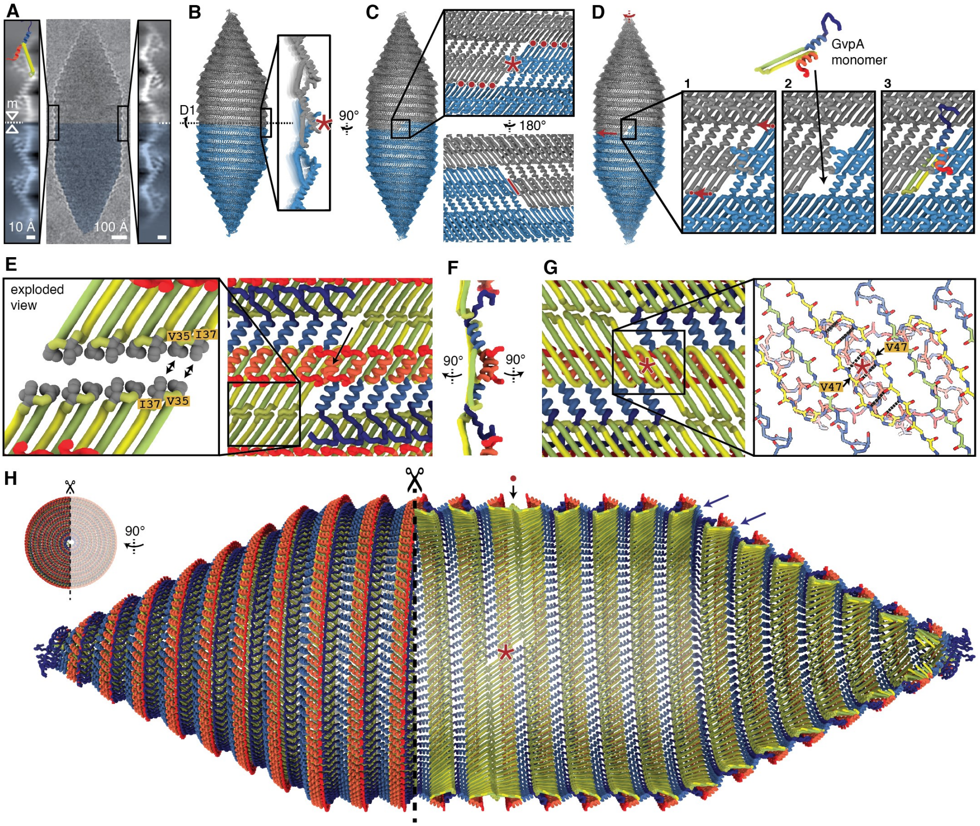

Figure 3.3: Pseudo-atomic model of a gas vesicle with two half shells of inverted orientation. (A) Raw cryo-EM image of a single GV (with inverted contrast). β-hairpins of GvpA2 (cartoon) always point towards the seam at the center of the GV cylinder. Two different types of 2D class averages of the seam (left and right) are observed. The mirror symmetry (mirror axis: m) suggests a 180° symmetry axis (D1) at the point where two inversely oriented GV half shells meet. (B) Pseudo-atomic model of a GV constructed from two identical halves (gray, blue) with close-up side view of the polarity reversal point (PRP, red asterisk). (C) Close-up view onto the GvpA2 lattice around the PRP (red asterisk). Red dots indicate molecular contacts along the GV circumference where β-turns contact. The red line indicates contact between parts of hairpin strands β2 at the PRP. (D) Model of monomer insertion at the PRP. The two GV halves rotate against each other, with the β-hairpin contacts sliding over each other (red arrow) in a ratcheting fashion to allow monomer insertion in the resulting gap. Insertion of the monomer in the opposite orientation than depicted is geometrically equivalent and would enlarge the other GV half. (E) View onto the seam between the two GV halves with color scheme as in Figure 3.2B The seam is sealed by contacting β-turns and the hydrophobic side chains Val35 and Ile37 (exploded view in inset). The lateral orientation of the hairpins is not uniquely determined by the data. An unresolved sterical clash between α2-helices from GvpA monomers around to the PRP is marked by an arrow. (F) Side-view of the PRP with same color-scheme. (G) View of the PRP from inside the gas vesicle. Oppositely oriented monomers next to the PRP are connected by 6 hydrogen bonds formed between the backbones of the β2-strands, with amino acid Val47 being located around the D1-symmetry axis (red asterisk). (H) Enlarged, sideways rotated and cut open GV model with PRP (asterisk) and seam (dot) annotated. The proposed hinging motion of the N-terminus required for adaption to the cylinder-to-cone transition and the reducing diameter of the tip is shown (blue arrows).

midpoint of the helical GV segment (Figure 3.1B), consistent with previous observations [166]. We therefore propose that insertion of new monomers on either side of the PRP occurs stochastically through ratcheting of the two GV half-shells by rotation relative to each other, generating a single monomer gap at the PRP (Figure 3.3D). This would involve breaking the lateral hydrogen bonds between the two monomers around the PRP, along with breaking and re-establishing hydrophobic contacts (Val35, Ile37) of the β-turns at the seam with no net loss in energy (Figure 3.3E). In our model, two factors suggest that the PRP represents the weakest point in the assembly. First, the monomer orientation at the PRP leads to steric hindrance by the α2 helices of the two symmetry-related monomers (Figure 3.3E). Second, the two oppositely oriented monomers at the PRP are connected by only 6 hydrogen bonds between segments of strand β2 around Val47 as compared to 11 hydrogen bonds formed between monomers along the rib (Figure 3.3G). We propose that the energetic disadvantage of this conformation facilitates opening of the seam for addition of new monomers during growth.

If the GV grows by adding monomers at the PRP, backward extrapolation starting from a mature GV leads to a state at which the seam forms between two conical half-shells (Figure 3.4A). This is the point where conical growth transitions into cylindrical growth. This transition requires adaption of the relative orientation of adjacent ribs, which we propose is mediated through a hinging motion of the N-terminus relative to helix α1 to accommodate for the reduction in diameter at the transition point and along the cone towards the tip (Figure 3.3H).

Continuing this extrapolation leads to a biconical nucleus which must initially form to start GV biogenesis. According to our model, the original nucleus would remain at the cone tips on both half-shells after maturation. The 2D classes and the fitted pseudo-atomic model suggest that N-terminal residues of GvpA2 monomers crowd together at the tip (Figure 3.4B-C). At diameters lower than 50 Å, the 2D class averages of these cone tips display weak density (Figure A2F) sealing off the opening. The fuzzy appearance of the density at the tip is indicative of structural heterogeneity in the nucleating monomers.

CONSERVATION OF GV SHELL ARCHITECTURE

Sequence alignments between GvpAs of three evolutionary diverse bacterial and archaeal species producing gas vesicles reveal a high degree of sequence conservation in the structural parts of GvpA, suggesting that the overall mode of GvpA shell assembly must be similar. This is supported by computational predictions using AlphaFold2, revealing highly similar assemblies (ribs) of GvpA oligomers for the evolutionarily distant GvpAs in firmicutes (*B. megaterium*), cyanobacteria (*A. flos-aquae*) and the archaeon H.salinarum, that all resemble our experimental structure (Figure 3.5A-B).

To verify these predictions, we employed cryo-EM to image GVs of *A. flos-aquae*. Differences in the GvpA sequences between *A. flos-aquae* and *B. megaterium* GvpA2 locate mainly to the N-terminal and C-terminal regions of the folded core (Figure 3.5C). *A. flos-aquae* GVs formed cone-ended cylinders with mean diameter of 87±7 nm, consistent with previous observations [161]. Despite significant effort, 3D refinement using a similar helical reconstruction strategy as for *B. megaterium* did not converge. Closer inspection of full-length GVs revealed them to flatten in the thin ice of the cryo-EM sample, breaking symmetry assumptions of helical reconstruction. We therefore resorted to obtain

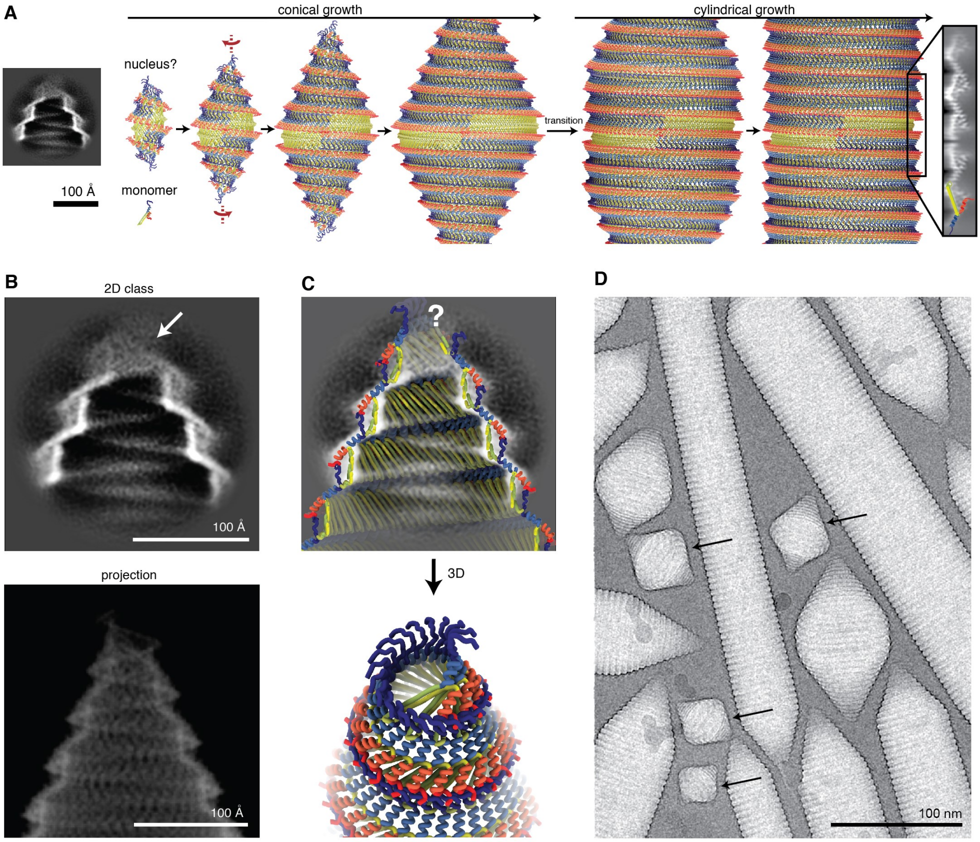

Figure 3.4: Model of GV growth from initial nucleus. (A) GV growth from a hypothetical nucleus to mature GVs. Transition from conical to cylindrical growth is annotated. A 2D class of GV tips with proposed nucleus remnants is shown to scale. (B) Class average of the GV tip shows no molecular order at diameters lower than 50 Å towards the cone end. 2D projection of the pseudo-atomic model is shown to scale. (C) 2D class overlaid with cut-through of the pseudo-atomic model, and 3D view onto the tip. The simplified model of a helix with linearly decreasing radius breaks down at the very tip, leading to clashes between the main chains. N-termini from GvpA monomers at the tip come into proximity and might close off the gas space. (D) Cryo-EM micrograph with immature GV bicones (arrows).

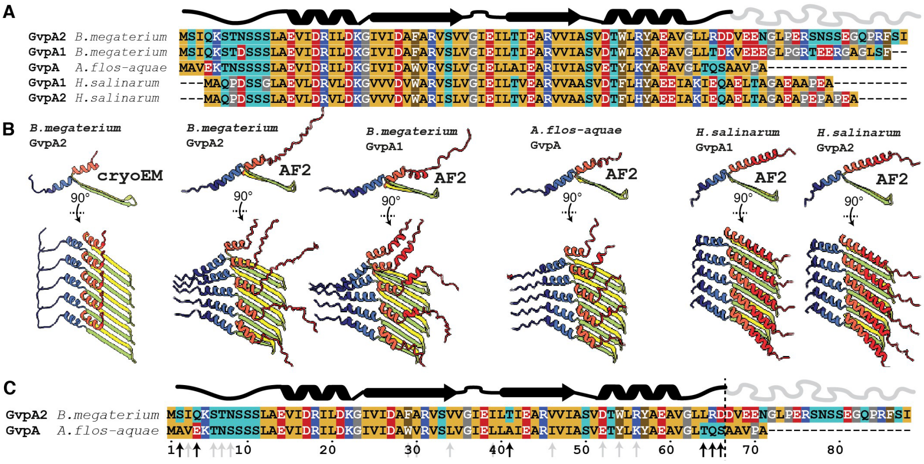

Figure 3.5: Highly conserved GvpA from *B. megaterium* and *A. flos-aquae* adopt the same fold and assembly. (A) Sequence alignment of *B. megaterium* (Mega) GvpA1 (GvpA) and GvpA2 (GvpB), *A. flos-aquae* (Ana) GvpA and *H. salinarum* (Halo) GvpA1 and GvpA2 show high degree of conservation despite forming gas vesicles of different diameters. (B) AF2 prediction of GvpA 5-mers for selected genes compared to the cryo-EM structure. Only the middle monomer is shown in side-view. AF2 predicts the general arrangement of a GvpA rib and the angle between the β-hairpin and α-helix 1 accurately. The N-terminal coil appears different, and the distance between α-helix 1 (where gas pores are located) is not accurately modeled by AF2. (C) Protein sequences of wall-forming protein GvpA from both *B. megaterium* and *A. flos-aquae* are very similar. Black arrows show six property changing mutations, gray arrows twelve property-conserving mutations in the ordered part of the structure.

high-resolution structural information from 2D classification. Class averages of GV edges showed a corrugated zig-zag pattern of the 2 nm thick wall formed by GvpA (Figure A4A). Another set of 2D class averages, obtained from collapsed GVs also present in the data, revealed the *A. flos-aquae* GV wall to consist of a periodic array of ribs consisting of dense 5.0 x 1.25 nm GvpA subunits tilted at -36° relative to the long axis of the cylinder (Figure A4B). The class averages with a resolution of better than 4.8 Å allow discerning the α-helical repeat of helix α1 bridging the gap of adjacent ribs, and the individual β-strands of the polymerizing β-hairpin. A cumulative Fourier spectrum computed from in-plane rotated GV segments showed a typical Fourier transform of a helix (Figure A4C), consistent with our 3D reconstruction from *B. megaterium* GVs (Figure A4D). We compared the *A. flos-aquae* 2D classes of GV wall side and top views with equivalent projections of the *B. megaterium* GV structure. On the level of the main-chain fold, the two GV shell assemblies are indistinguishable, hence confirming the conserved architecture of GvpA assembly of the GV shell (Figure 3.6). Our model of two contacting half-shells also applies to *A. flos-aquae* GVs as we observe similar contacting β-turns in 2D class averages of the seam (Figure 3.6C,G). More generally, our results establish that 2D classification of GV edges in cryo-EM data can give valuable structural insight into gas vesicle architecture for cases when 3D reconstruction is out of reach. This is due to the small unit cell of the GV wall,

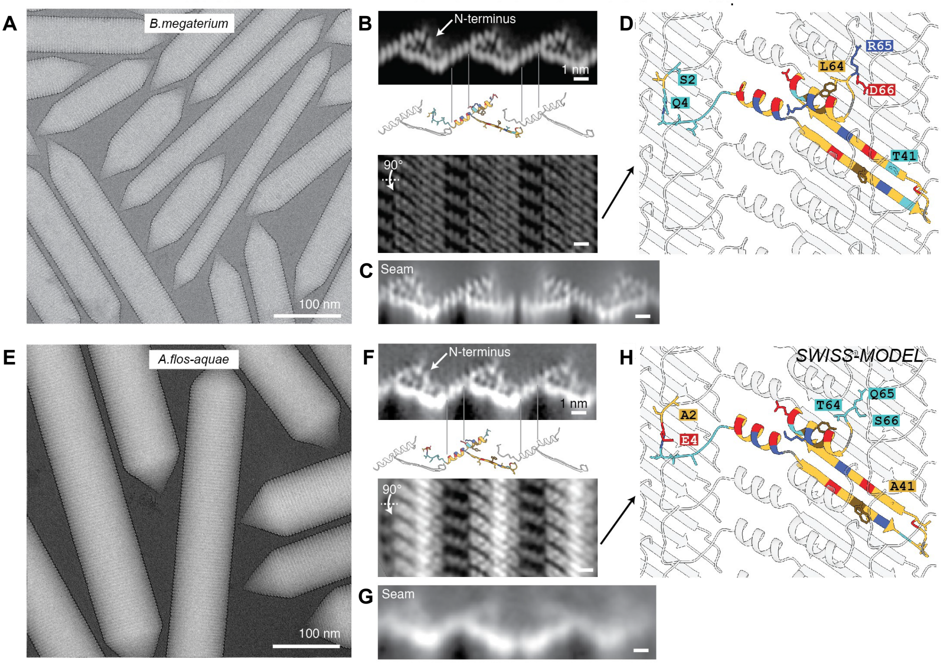

Figure 3.6: (A) Representative cryo-EM micrograph of *B. megaterium* GVs. (B) 2D-projected side view and top view of the 3.2 Å cryo-EM density of *B. megaterium* GVs. (C) 2D class average of seam between two GV half shells. (D) Atomic model of *B. megaterium* GV wall with different side chains between both species displayed and property-changing mutations highlighted by one-letter-code. Residues are colored according to side chain chemistry.(E,F,G,H) Same data for A.flos-aquae GVs shows the high degree of conservation of GvpA fold and assembly. The 2D views in (F) are computed by 2D classification of GV edges and collapsed GVs and have a resolution better than 5.4 Å or 4.8 Å as the α-helical pitch or the β-strands are resolved. The homology model of the A.flos-aquae GV wall was computed using SWISS-MODEL.

where not many structural features overlap in side views at the GV edges. 2D class averages can be computed to sufficient resolution to see secondary structure elements and even large side chains. We suggest that this approach can be used for comparative studies of GVs from different species with larger sequence divergence to reveal different assembly modes, such as resulting from differences in binding modes of the evolutionarily less conserved GvpA N-terminus (Figure A5A).

REINFORCEMENT OF THE GV SHELL BY GVPC

Many GV gene clusters contain a second structural gas vesicle protein GvpC, which is absent from our model GV from *B. megaterium* [167]. GvpC binds on the outside of GVs and increases the critical collapse pressure of GVs [16, 168]. While the essential role of GvpC has been firmly established, how it binds to and reinforces GVs has remained elusive. We acquired cryo-EM datasets of *A. flos-aquae* GVs, and to investigate the structural role of

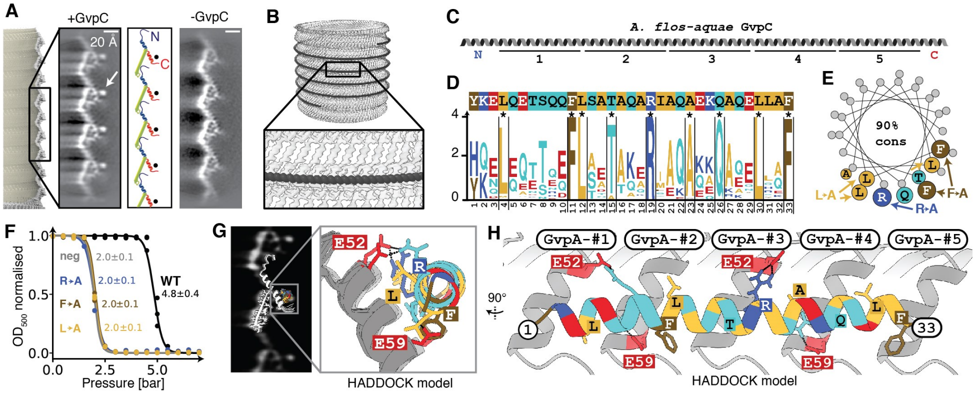

Figure 3.7: The secondary wall protein GvpC binds along the GvpA ribs of *A. flos-aquae* GVs. (A) Comparison of 2D class averages of GV edges with (left) and without GvpC (right) reveal an additional circular density. A cartoon model of GvpA helps locate the GvpC density to helix α2. (B) Artist impression of GvpC molecules wrapping around GVs. (C) Predicted secondary structure and 33 amino acid repeats 1-5 of *A. flos-aquae* GvpC. (D) Consensus sequence of the GvpC repeats with logo representation of evolutionary conservation reveals nine highly conserved residues. The height of the characters depicts the degree of conservation (information content in bits). (E) Helical wheel plot of highly conserved amino acids reveal that there is one highly conserved face of the α-helical repeat. Experimentally tested GvpC mutants are indicated. (F) Critical collapse pressure measurements of *A. flos-aquae* GVs supplemented with WT GvpC, GvpC mutants or stripped of GvpC.(G) Comparison of 2D class average of GvpC-bound GVs and predicted binding mode between a GvpC consensus repeat and seven *A. flos-aquae* GvpA monomers. (H) Rotated view of binding model with predicted interactions of residues.

GvpC, we imaged the GVs in the presence and absence of GvpC and compared 2D class averages of the GV edges (Figure 3.7A).

The class average containing GvpC shows an additional dot-like density (approx. 10 Å diameter) located in vicinity to helix α2 (Figure 3.7A). This feature and its dimensions are consistent with the projection of an α-helix viewed along its helical axis. Indeed, GvpC is predicted to be all α-helical [151] and consists of five 33 residue repeats (Figure 3.7B,C) that are highly similar in sequence. The class averages suggest that GvpC binds along the ribs of gas vesicles and contacts helix α2 of GvpA (Figure 3.7B), which is supported by a recent molecular envelope of the *A. flos-aquae* GV wall determined by electron tomography [169]. We analyzed the evolutionary conservation of the repeat sequence. In a set of 91 GvpC sequences (Figure A5B) from different organisms, we find nine residues to be conserved in more than 90% of those sequences, including a strongly conserved set of leucine (Leu4,12,30), phenylalanine (Phe11,33) and arginine (Arg19) residues (Figure 3.7D). A helical wheel plot of the repeat shows that all conserved residues cluster on the same face (Figure 3.7E) that likely forms the binding interface. We further confirmed the importance of these residues by designing alanine mutants for occurrences in all five repeats (Figure A6A). All GvpC mutants abrogated stabilization of GVs (Figure 3.7F). Our 2D class averages provide strong spatial restraints on the positioning of GvpC relative to the GvpA ribs, while the conservation pattern and mutants pinpoint residues essential for binding. We used these data as restraints to predict a model for GvpC binding by computational docking (Figure 3.7G, Figure A6E-H).

While our data does not allow us to decisively distinguish whether GvpC follows the left-handed spiral of the rib upwards towards the tips, or downwards, we obtained the highest scoring docking solution with the downward orientation (Figure 3.7H). A single GvpC repeat spans four monomers of GvpA. In this GvpA tetrad, glutamate residues Glu52 and Glu59 in GvpA monomers 1, 2, and 4 form hydrogen bonds with GvpC. In our model, Glu52 in monomer 3 binds to the conserved Arg19 of GvpC, while Glu59 in monomer 4 binds to the conserved Gln26. The (Leu4, Leu12, Leu30) triplet inserts between the α2 helices of the GvpA tetrad, while Phe11 and Phe33 are sandwiched in-between α2 in GvpA monomers 2 and 3 and face-on on helix α2 of monomer 4.

3.3. DISCUSSION

Gas vesicles represent a remarkable example of biomolecular self-assembly. Our results provide a canonical structural framework for the unique molecular properties of gas vesicles, including their selective permeability to gases [170], their mechanical stability [165] and their distinctive ability to grow without compromising the integrity of its shell [126]. Our work establishes an atomic resolution model of the mature GV shell formed exclusively by GvpA. A key question is how GvpA nucleates to form an elementary bicone from which the shell extends during GV growth. Besides GvpA, many GV gene clusters contain genes encoding the proteins GvpJ, GvpM or GvpS [167] that exhibit high sequence homology and predicted folds similar to that of GvpA. A dominant structural role of these homologues in mature GVs is unlikely, as none of them were found in intact gas vesicles [168], suggesting a putative role as nucleation factors. Additional support for this role comes from the observation that in some species, GvpJ and GvpM are expressed as part of a separate transcript exclusively during early exponential growth [150], whereas a transcript of gvpACNO is expressed at later stages - possibly to enlarge the formed nuclei. How the initial nucleus is structured and by which mechanism other Gvps assist in growth remain open questions [171].

In most organisms, biconical GVs transition their growth mode when reaching a certain diameter and continue extending cylindrically. This transition occurs over a range of diameters, different for each individual GV. We observed mature cylindrical *B. megaterium* GVs with a diameter of 55.5±7.3 nm corresponding to 145±19 monomers per helical turn, and mature *A. flos-aquae* GVs with diameter of 87.1±6.9 nm corresponding to 227±18 monomers per helical turn. The mechanism for the bicone-to-cylinder transition is unknown. The GvpA ribs in the cones are highly curved and may be energetically disfavoured. Insertion of new monomers in a bicone results in enlargement of the cone and reduces rib curvature. However, the expanding cone does not provide defined interactions between monomers of adjacent ribs. In contrast, cylindrical GV segments have crystalline order where the N-terminus always has identical contacts to the adjacent rib. The interplay of curvature preference and the energetic advantage of crystallinity could favour a cone-to-cyclinder transition at a certain critical diameter. This suggests that the GvpA N-terminus could play a role in determining the size distribution of GVs. Consistently, the sequence of the N-terminus is most divergent. Further evidence for the decisive role of GvpA sequence in defining the final diameter comes from a hybrid GV gene cluster where *A. flos-aquae* GvpA integrated into the native gene cluster of *B. megaterium*, resulting in GVs with diameters consistent with native *A. flos-aquae* GVs [4].

Our structure reveals that the gas permeability of the GV wall can be ascribed to a large number of molecular pores formed between α1-helices of the GvpA shell, the size of which is compatible with the collision diameters (2.65–3.64 Å) of typical atmospheric gases dissolved in the cytosol [163]. Surprisingly, the GV wall has been shown to be permeable to perfluorocyclobutane (C_4F_8) with a collision diameter (6.3 Å) exceeding the estimated pore size in our structure. While atmospheric gases appear to diffuse freely through the GV wall [170], the diffusion coefficient of C_4F_8 is consistent with a very small number (11) of such pores [149]. Based on our pseudo-atomic model, such pores would need to be located at the seam, PRP or at the conical tips. Alternatively, flexibility in the GV shell may modulate size of the regular gas pores to allow passage of C_4F_8.

We inferred a binding mode of a single 33 amino acid repeat of GvpC to four consecutive GvpA monomers assembled in the cylindrical *A. flos-aquae* GV shell. The requirement for a binding site comprised of consecutive GvpA monomers in a helical assembly is consistent with previous observations in split-GFP assays showing that monomeric GvpA and GvpC do not interact [171]. What remains open is how the five consecutive GvpC repeats are structured. It is likely that all repeats would form identical molecular contacts with the GvpA ribs. The side-by-side distance of GvpA monomers measured between identical points of the inner β-hairpins is 12.1 Å. Due to the curvature of GVs, this distance increases radially outwards across the GV wall towards the binding site for GvpC. For an average 87 nm *A. flos-aquae* GV this distance is 12.7 Å. A single perfectly α-helical repeat of GvpC would span 49.5 Å (33 x 1.5Å/residue), only slightly shorter than the 50.8 Å spanned by a stretch of four GvpA monomers. The five tandem repeats of native GvpC would bind to 20 GvpA monomers. Taking into account additional space for the N and C-termini of GvpC, this corresponds well to a previously determined 1:25 molar ratio of GvpA to GvpC [151]. The modest distance mismatch between one GvpC repeat and a GvpA tetrad could be accommodated by slight deviation of GvpC from perfect helicity. It has been previously suggested that this would also be required to maintain the relative orientation of consecutive repeats, as with perfect helicity they would be (100° x 33) % 360 = 60° rotated towards each other [151]. A small unstructured stretch would allow GvpC to adapt to different curvatures of the GvpA ribs in cylindrical and conical parts and in GVs of different diameters.

We show that GvpC binds to α2 helix of the GV wall, thereby increasing the critical collapse pressure. The wall thickness measured between the extremes of the corrugation pattern increases from 3 nm to 4 nm when GvpC is bound. Because the buckling pressure of thin-walled cylinders is proportional to the third power of the wall thickness [165], the most straightforward explanation for enhanced stability is that GvpC bound on the outside of GVs increases the wall thickness. The real picture is likely more complicated. Our structure reveals that GVs are assembled from two helical half shells that are connected by a seam. Because of its structure, it is conceivable that the seam is a weak-point of the GV where failure will occur first. In this case, GvpC would be most critical to prevent failure at the seam, which questions its requirement elsewhere on the GV shell.

Recently, GVs have been repurposed as genetically encoded acoustic reporters [4, 53].

The high contrast in density between gas-filled GVs and surrounding cellular structures makes them amenable to ultrasound imaging [3]. While native GVs display little shell deformation under ultrasound exposure, GVs that are stripped of GvpC become less stiff and scatter non-linearily above a certain pressure threshold [128]. This behavior enables amplitude modulation imaging and multiplexing of stripped and unstripped GVs in an in vivo context [128, 172]. Engineering conditional binding strength of GvpC can transform GVs into biosensors with switchable acoustic properties [11, 19]. Our insights into GvpA-GvpC interaction provide a rational basis for designing such sensors. Moreover, the high-resolution structure of the GvpA shell may enable development of designer GVs with custom mechanical shell properties through direct engineering of the GvpA sequence.

Together, our results establish the molecular basis of a widely conserved buoyancy-controlled motility apparatus in aquatic bacteria and archaea. Our study will form the foundation for addressing a multitude of open questions on gas vesicle biogenesis such as nucleation, growth, width regulation, function of other gas vesicle gene products in GV assembly and species-to-species variability of GV gene clusters.

3.4. LIMITATIONS OF THE STUDY

While our structure provides an atomic model of the main structural protein GvpA as it forms the GV wall assembly and our data allowed inferring the binding geometry of GvpC to the gas vesicle wall, the function and/or structural role of other accessory proteins in GV gene clusters in GV biogenesis is yet to be determined. Some of those proteins presumably work together to create an initial nucleus, of which the structure remains unknown. We also report a pseudo-atomic model of an entire gas vesicle. The precise structure of the GvpA monomer in this model is supported by cryo-EM data at 3.2 Å resolution, however the special structural features of the assembly such as the seam, polarity reversal point and tip are inferred from 2D projection views alone. The exact molecular details at these special positions can slightly deviate from the pseudo-atomic model we present.

3.5. METHODS

B. megaterium GAS VESICLE EXPRESSION AND PURIFICATION

The purification protocol for Mega GVs was derived from [160]. In brief, BL21-DE3-pLysS *E.coli* cells were transformed with the pST39-pNL29 plasmid (a gift from Mikhail Shapiro; Addgene #91696)[160] and 1 L of lysogeny broth (LB) containing 0.2% (w/v) glucose was inoculated with 10 mL of overnight culture. The culture was grown at 37°C until OD=0.5 and GV expression was induced with 20 µM IPTG. Following induction, cells were grown at 30°C for 20 hours.

The culture was centrifuged at 500 rcf for 2 hours in 50 mL Falcon tubes. The floating fraction was collected with a peristaltic pump. This process was repeated once more. The resulting 25 mL of liquid were lysed chemically by adding 5 ml of SoluLyse reagent per 50 ml of liquid, 0.25 mg/ml lysozyme and 10 µg/ml DNaseI, and slowly rotated for 1 hour at room temperature.

GVs were purified in three overnight rounds of floatation separation by centrifugation at 800 rcf in 50 mL Falcon tubes. After each centrifugation step, the GV-containing top layer was gently removed with a pipette after which the GVs were resuspended in PBS containing 6M urea (first round), and subsequently in PBS alone. Final concentration was determined as OD_{500}=3.1 by optical density measurement at 500 nm against a sonicated blank. The sample was dialysed into imaging buffer (20 mM Tris, 50 mM NaCl, pH=8) prior to cryo-EM sample preparation.

A. flos-aquae GAS VESICLE PURIFICATION

The purification protocol for gas vesicles from *A. flos-aquae* was derived from Lakshmanan *et al.* [160]. Briefly, *A. flos-aquae* (CCAP 1403/13F), also known as *Dolichospermum flos-aquae*, were grown in 250 mL G625 medium complemented by BG11 medium (Sigma C3061) for approximately 2 weeks until confluence. The culture was centrifuged at 350 rcf for 4 hours or until a floating layer of cells was observed. Subnatant was removed using a syringe before lysing the cells in 500 mM sorbitol and 10% v/v lysis buffer (SoluLyse) at 4°C for 6-8 hours while gently rotating. GVs were purified by three rounds of flotation separation with 4-6 hour centrifugation at 350 rcf. After each centrifugation, subnatant was removed by syringe after which GVs were resuspended in PBS at pH 7.4.

GVPC MUTANT PURIFICATION

Codon-optimized genes for *A. flos-aquae* wild-type and mutant (R19A;F-11,33-A; L-4,12,30-A) GvpC (Uniprot: P09413) including a C-terminal 'GSGSGS' linker and a C-terminal 6xHis-tag in a pET-28a(+) vector were obtained from Genscript (New Jersey, United States). The mutations were engineered into all five repeats.

Proteins were expressed in *E.coli* BL21-DE3 cells grown in 750 mL autoinduction medium [173] for 3 h at 37°C before the temperature was lowered to 20°C for additional 20 h. The bacteria were harvested by centrifugation and lysed by freeze-thaw cycles in lysis buffer (20 mM Tris, 500 mM NaCl, 0.1% Triton-X, 20 mM imidazole; 5 mL per gram of pellet). Lysozyme (0.15 mg/mL) and DNAseI (10 µg/ml) were added and the lysate rotated for 2 h at room temperature. Isolation of inclusion body and IMAC purification was performed as described previously [160]. Protein purity was assessed by SDS-PAGE and concentration was determined according to Bradford.

PREPARATION OF GVS WITH RECOMBINANT GVPC AND COLLAPSE PRESSURE MEASUREMENTS

A. flos-aquae GVs were stripped of GvpC by resuspending in 6 M urea and 60 mM Tris buffer, using 3 rounds of flotation separation as previously described [160]. Recombinant GvpC was added to stripped GVs according to the formulation: 2 x OD_{500} x 198 nM x GV volume (liters) = nmol GvpC. GvpC will be present in a twofold excess under the assumption of a 1:25 molar ratio of GvpC/GvpA [160]. The urea solution was then slowly replaced with PBS at pH 7.4 by 2 rounds of ≈12 hours of dialysis over a 7-10 kDA MWCO dialysis membrane. Finally, 3 rounds of floatation separation at 350 rcf removed traces of urea. GVs were diluted to OD_{500}=0.1-0.4 for collapse pressure measurements. Samples were loaded in a pressure vessel and hydrostatic pressure was increased in increments of 0.5 bar using pressurized nitrogen gas. Samples were allowed to equilibrate for 5 seconds after pressure changes before absorption was measured using a spectrophotometer (Ocean optics) at 500 nm. OD_{500} values were normalized between the minimum and maximum for each measurement. Three independent re-additions per GvpC mutant were performed and measured.

A sigmoid function with p_0 as the inflection point and k as the width was fitted to the curves using the means and standard deviations of measured triplicates (n=3) as input for the scipy *'curve_fit'* function.

$OD_{500,norm} = \frac{1}{1+e^{k(p-p_0)}}$

The error of p_0 was determined using a bootstrapping approach, performing the fit 50 times with a random set of n out of n measurement points with replacement. The parameters and their uncertainty were estimated as their mean and standard deviation over the 50 fits.

CRYO-EM OF *B. megaterium* GAS VESICLES

B. megaterium gas vesicles at OD_{500}=3.1 were applied to a freshly glow-discharged Quantifoil R2/1 grid and frozen using a Leica plunger set to 95% humidity, front-side blotting and 20°C with blot times ranging from 5-11 seconds. Micrographs were collected on a Titan Krios (Thermo Fisher Scientific) microscope at the Netherlands Center for Electron Nanoscopy (NeCEN) operated at 300 kV. Dose-fractionated movies were acquired on a Gatan K3 direct electron detector at a pixel size of 1.37 Å with 60 frames over an exposure of 30 $e^-/Å^2$ and a defocus range from -0.25 to -1.25 µm.

CRYO-EM OF *A. flos-aquae* GAS VESICLES

Native *A. flos-aquae* gas vesicles (containing GvpC) at OD_{500}=13 in imaging buffer (20 mM Tris, 50 mM NaCl, 0.5 mM EDTA, pH=8) were applied to a freshly glow-discharged Quantifoil R2/1 grid and frozen using a Leica plunger set to backside-blotting, 95% humidity and 20°C with 10 s blot time. 1273 cryo-EM micrographs at 1.288 Å pixel size were acquired on a JEOL 3200 microscope with a K2 detector using 62 e^- total exposure over 60 frames. *A. flos-aquae* GVs stripped from GvpC (OD_{500}=1, in PBS buffer) were prepared and imaged in a similar same way, using 17.6 e^- over 50 frames, 1.288 Å pixel size, acquiring 58 micrographs.

DATA PROCESSING AND STRUCTURE DETERMINATION OF *B. megaterium* GVS

4351 collected super-resolution movies were 2x binned and motion-corrected in RELION 3.1 [174]. CTF determination was performed using Gctf 1.06 [175]. 709 micrographs containing thin GVs with a diameter of 42 nm or less were identified manually. 1021 tubes were manually picked in RELION by selecting start and end coordinates. 36,295 overlapping segments with 512 pixels were extracted along the cylindrical sections with a step size of 49 Å (2x binned). 2D classification was done in RELION3.1 with the 'ignore CTFs until first peak' option turned on. The resulting 2D class averages were grouped by projecting them along the helical axis and calculating the rim-to-rim distance (Figure A2B) between the two density maxima. A class with 35.6 nm edge-to-edge distance was selected containing 2911 segments.

Analysis of in-plane rotated power spectra of the segments using Helixplorer (http://rico.ibs.fr/helixplorer/) revealed a likely helical symmetry between 90.92 to 95.92 units per helical rung, with ≈49 Å helical pitch. 2D classification was not sufficient to separate all symmetries and the final set of segments originated from several assemblies with different symmetries.

3D classification starting from a featureless cylinder and imposing candidate symmetry parameters was used to further select for segments adhering to a particular symmetry, leading to 1460 segments with symmetry of 92.93 units per turn. 3D refinement of those particles with CTF refinement and Bayesian polishing led to a resolution of 3.6 Å at FSC=0.143. Convergence of 3D refinements was only achieved when using a *'tau_fudge'* parameter of 5.

A final round of particle polishing was used to create a new particle stack extracted only from frames 1-20 (0-10 $e^-/Å^2$) of the movies. Particles were exported to cryoSPARC 3.1.0 [176] and high-pass filtered to 100 Å. 3D refinement with the helical reconstruction algorithm implemented in cryoSPARC also led to a reconstruction at 3.6 Å. To account for small deviations from helical symmetry, e.g. by flattening of the tube in ice, a mask encompassing ≈3x9 GvpA2 monomers was created in ChimeraX [177]. The particle stack expanded by helical symmetry was subjected to focused refinement in cryoSPARC using the mask, which increased the final resolution to 3.2 Å at FSC=0.143. The final maps were cropped from a box size of 512^3 voxels to a box size of 128^3 voxels centered on the refined region. Local resolution was calculated in cryoSPARC 3.1.0 [176] and mapped onto the monomer structure in ChimeraX [177].

ATOMIC MODEL BUILDING AND REFINEMENT

To build an atomic model of a GvpA2 monomer the final map density was traced de novo using COOT [178]. The monomer was expanded using helical symmetry (rise: 0.525 Å, twist: -3.87°) into a 15 subunit segment (three ribs with 5 monomers each) to account for connections between monomers and manually adjusted in ISOLDE [179] before automatic real-space refinement in PHENIX 1.13 [180]. We used phenix_real_space_refine with automatic restraint weighting to refine coordinates and atomic displacement factors against the globally sharpened experimental density map using secondary structure and non-crystallographic symmetry restraints. The central monomer of the 15 subunit segment was used as the asymmetric unit for PDB deposition. Renderings of the cryo-EM density and atomic models were made in ChimeraX 1.4 [177].

2D CLASSIFICATION OF EDGES, SEAMS AND TIPS

From the *B. megaterium* gas vesicles cryo-EM dataset, several hundred particles of either seams or tips were picked manually and used to generate a template for automated picking in cryoSPARC 3.3 [176]. Particles were high-pass filtered to 100 Å to eliminate the large negative contrast of the gas space in the GV interior. The picked particles were cleaned up by several rounds of 2D classification to give a clean set of particles of either the seam, the polarity reversal point or the tips. These particle sets were used to train a neural network for particle picking (TOPAZ v0.23 [181]), which was then applied to the micrographs to pick seams, PRPs, and tips. Those particles were cleaned by several rounds of 2D classification and led to the final presented 2D classes. For display, the 2D classes were treated in ImageJ using an 'unsharp mask' filter.

The two cryo-EM datasets of *A. flos-aquae* gas vesicles with and without GvpC were used to obtain 2D class images of the edges leading to side-views of the wall. Movies were imported into cryoSPARC v3.3 [176], motion-corrected and CTF-estimated. For both dataset, frames were used only until an exposure of ≈15 $e^-/Å^2$ because shrinking of GVs was observed for high exposures leading to GV edges blurring out. A few hundred edges were manually selected for 2D classification to generate picking references for the cryoSPARC filament tracer. Particles were extracted with 192 pixel box size and high-pass filtered to 100 Å. Several rounds of 2D classification and selection of sharp classes led to the final 2D classes of the GV edges with and without GvpC. For display, the 2D classes were treated in ImageJ using an 'unsharp mask' filter.

Similarly, 2D classes of the GvpA lattice from collapsed GVs were calculated from the *A. flos-aquae* GV dataset above including GvpC. For this, the dataset was preprocessed in RELION 3.1 [174], points on the lattice manually picked to create a 2D class, which was then used for automated particle picking. Particles were extracted with a box size of 128 pixels and aligned with 2D classification to generate a view onto the collapsed GV wall. The biggest class containing ≈34,000 particles was selected and was treated in ImageJ using an 'unsharp mask' filter.

PORE ANALYSIS

Gas pores in the gas vesicle wall were analysed using MOLE 2.5 [162]. The gap between α1 helices has a slit-type shape, enabling multiple possible routes for gas diffusion. Several start and endpoints of tunnels around both sides of the slit were selected and tunnels were computed with MOLE. The slit was modelled by three tunnels and displayed in Chimera [182]. The minimal constriction of the tunnel was calculated as the diameter of the smallest sphere in the respective tunnel model.

PSEUDO-ATOMIC MODELLING OF A COMPLETE GV

The model was generated from the solved atomic model of *B. megaterium* GvpA2. The GvpA2 monomer was placed next to the x-axis (D1 axis) manually such that a 180°, symmetry copy operation around the x-axis would reproduce a side view of the GV edge compatible with the determined 2D class average.

A left-handed parametric helix in 3D space was defined with the parameter t corresponding to turns of the helix:

$$t_{\text{cap}} = \frac{r_{max}}{P \cdot sin(\alpha)}$$

$$r(t) = \begin{cases} r_{max} & \text{if } t < t_{cyl} \\ r_{max} \cdot \left(1 - \frac{t - t_{cyl}}{t_{cap}}\right) & \text{if } t \geq t_{cyl}. \end{cases}$$

$$x(t) = r(t) \cdot cos(2\pi t)$$

$$y(t) = -r(t) \cdot sin(2\pi t)$$

$$r(t) = \begin{cases} P \cdot t & \text{if } t < t_{cyl} \\ P \cdot t_{cyl} + P \cdot cos(\alpha) \cdot (t - t_{cyl}) & \text{if } t \geq t_{cyl}. \end{cases}$$

where t_{caps} is the number of turns in the cap, $\mathrm{t}_{\mathrm{cyl}}$ is a user-parameter of how many cylindrical turns the model should have (5), P is the pitch of the helix of 48.8 Å, $\mathrm{r}_{\mathrm{max}}$ the radius of the assembly of 178.4 Å, and α is the cone angle of the tip (25°).

The starting point of the curve was adjusted to go through the pivot point (in the center of the two β-sheets between amino acid (AA) 28 and AA 42 carbonyl oxygen atom) of the placed monomer by applying a shift along the z-axis and rotation around the z-axis. Points were placed along the curve at a distance of 12.07 Å, calculated as $\sqrt{((2pr)^2 + P^2)/u_t}$, where u_t is the number of monomers per turn defined by the solved helical symmetry (92.93). 835 points were placed with the last 4 points towards the tip being omitted.

A model only with placement of monomers does not reflect the experimental 2D classes well. Four additional parameters were introduced rotating and modifying the monomer:

(1) a correction for the change of helix angle towards the ends of the tip as the helix becomes steeper with narrower radius. The rotation center is between the AA28 and AA42 carbonyl oxygen atoms, and the rotation axis normal to a fitted plane through C-α atoms of all amino acids of the β-hairpin (AA23-49).

(2) a rotation of the entire monomer to account for the tilt of monomers following the cone angle. The rotation center is carbonyl oxygen 36 and the axis normal to the plane of AA24-33 C-β atoms.

(3) a hinging motion of the two β-strands to account for the deformation visible in 2D classes of the polarity reversal point where GvpA ribs from both gas vesicles halves meet. The rotation axis is defined by a line between the AA23 C-α atom and the AA49 C-α atom, and moves the atoms of AA23-49.

(4) a hinging motion of the α-helix 1 and the N-terminus, to account for gaps in the assembly formed when monomers tilt towards the cone angle. The axis is defined as in (3), and the rotation moves the atoms of AA2-23.

For the purpose of illustrating GV growth from nuclei to mature cylinders, the model was replicated in Blender 3.0 in a simplified form (without modifications of the monomer) and animated using varying parameters for the diameter and the t_{cyl} parameter.

AlphaFold2 structure predictions

Complexes of five monomers of GvpA corresponding to a rib section of the GV wall were predicted using AlphaFold2 [183] run in a Google Colab environment [184] with each five generated models per run and six recycles. The highest-scoring model was selected and displayed in ChimeraX [177].

Bioinformatics analysis

The sequences of the five 33 AA repeats of *A. flos-aquae* GvpC (Uniprot P09413) was converted into a consensus sequence 'YKELQETSQQFLSATAQARIAQAEKQAQELLAF' using the software 'cons' from the EMBOSS package [185]. The sequence was used as input for the ConSurf Server [186] to search the UniRef90 database with the HMMER web server [187] using one iteration, resulting in 91 sequences. The resulting sequence alignment was displayed and consensus sequences calculated in MView [188]. A sequence logo was calculated from the sequence alignment using WebLogo [189]. Helical wheel plots were generated in Heliquest [190].

HADDOCK modelling of GvpC binding to *A. flos-aquae* gas vesicles

A α-helical model of the 33 residue consensus repeat of *A. flos-aquae* GvpC ('YKELQETSQQFLSATAQARIAQAEKQAQELLAF') was generated in ChimeraX [177] using ideal α-helical backbone dihedral angles φ=-57° and ψ=-47°. A homology model of the *A. flos-aquae* GvpA monomer was generated using SWISS-MODEL [191] based on the structure of *B. megaterium* structure GvpA2 and the *A. flos-aquae* sequence for GvpA (UniProt: P10397). The homology model was extended with the symmetry parameters from the *B. megaterium* assembly in ChimeraX [177] into a rib of 7 adjacent monomers.

Both models were used as input for HADDOCK 2.4 [192]. For GvpC, residues 4, 11, 12, 15, 19, 23, 26, 30, 33, which all are >90% conserved in the bioinformatics analysis were chosen as active residues. For GvpA, residues 51-61 of GvpA, part of helix α2 and adjacent to the GvpC density in the 2D classes, were chosen as active residues. All remaining settings were used at default values.

The highest scoring cluster of the docking solutions (HADDOCK score: -108.4 +/- 5.0) showed GvpC binding across several GvpA monomers along the helical spiral of the rib, with the GvpC sequence oriented inversely to the direction of helical propagation (with the direction from seam to tip). A very similar cluster was found shifted by one GvpA monomer laterally with the same molecular contacts and was discarded. A second, lower scoring type of cluster (HADDOCK score: -90.7 +/- 4.6) showed GvpC binding mode with the GvpC sequence oriented to the direction of helical propagation.

Docking clusters were displayed in ChimeraX [177] and hydrogen bonds between GvpA and GvpC highlighted with the ’hbonds’ command. The highest-scoring solution was manually fitted into a 2D class of the *A. flos-aquae* GV wall with GvpC.

4

ACOUSTIC PH BIOSENSOR FOR DYNAMIC ULTRASOUND IMAGING OF INTRACELLULAR ACIDIFICATION

Genetically encoded pH sensors based on fluorescent proteins enable dynamic optical imaging of cellular processes such as endocytosis and exocytosis. To date, light scattering in thick tissue as well as photobleaching of fluorescent proteins prevent deep cellular imaging over sustained periods of time. To visualize intracellular pH variations across opaque organs, we introduce a genetically encoded acoustic pH sensor dubbed 'pHonon'. We modified the outer gas vesicle protein (GvpC) of echogenic protein nanostructures via histidine point mutations. At low pH, engineered gas vesicles exhibit an increased shell stiffness which switched their acoustic response from nonlinear to linear. By combining pHonons with nonlinear ultrasound imaging, we captured dynamic deep tissue images of lysosomal acidification by macrophages in murine liver. The combination of pHonon with nonlinear ultrasound creates the possibility for basic studies of endocytic activity in deep tissue of living opaque organisms.

Terwiel, D., Park, B.M., Heiles, B., Waasdorp, R., Munoz-Ibarra, E., Ara, T., Gazzola, V. and Maresca, D. (2025). Acoustic pH sensor for dynamic ultrasound imaging of cellular acidification. bioRxiv, pp.2025-01.

4.1. INTRODUCTION

pH regulation plays a crucial role in maintaining the homeostasis of cellular environments in healthy organisms. Disruptions of the pH balance are associated with numerous pathologies, including cancer [31, 32], cardio- and cerebrovascular damage [33] or ischemia-reperfusion injury [34]. The development of methods to visualize intracellular or extracellular pH variations in living tissue is therefore an active field of research [35–39]. Because of light scattering in thick tissue, optical pH imaging methods are limited to studying thin specimens and cannot easily monitor pH variations at the organ scale. On the other hand, magnetic resonance pH imaging is sensitive to extracellular pH levels but cannot observe intracellular events.

In comparison, ultrasound provides an interesting trade-off between spatiotemporal resolution, coverage, scalability, and availability of genetically encoded probes [3, 53]. Acoustic waves in the MHz range travel centimeters deep within opaque tissue while providing a resolution ranging from approximately 1 mm to 100 µm. Another advantage is that ultrasound imaging is performed with a single lightweight probe for transmission/reception, which provides easier access to specimens than microscopes or MRI scanners. Finally, the recent development of acoustic reporter genes and biosensors based on genetically encoded gas vesicles (GVs) [4, 10] redefines the ability of ultrasound to visualize cellular function.

Assembled GVs consist of two structural proteins, gas vesicle protein A (GvpA) and gas vesicle protein C (GvpC) [12, 169, 193]. GvpA forms the outer wall of GVs in a helical chain, while GvpC provides mechanical reinforcement and rigidity to the shell. GvpC is currently the focal point for engineering GV acoustic sensors [11, 30]. Previous studies have shown that removal of GvpC results in a weakening of the GV shell [16, 19], which allows GV shell buckling under acoustic pressure and triggers nonlinear ultrasound backscattering [20]. The recent development of the first GV-based biosensor showed that the inclusion of protease recognition motifs in GvpC allowed proteases to cleave GvpC, thereby creating an ultrasound sensor that switched its acoustic response from linear to nonlinear in the presence of enzyme activity [11]. More recently, a first ultrasonic calcium indicator based on GVs was reported [30]. This sensor, which borrows design elements of fluorescent calcium indicators, relied on the inclusion of calmodulin in GvpC and of a calmodulin binding peptide linked through a flexible linker to the C-terminus of GvpC [30]. In practice, binding of the calmodulin binding peptide to calmodulin and the subsequent deformation of GvpC causes GvpC to detach from GvpA, leading to a nonlinear acoustic response of the indicator in the presence of calcium.

Here, we present the development of the first GV-based acoustic pH biosensor for ultrasound imaging of intracellular acidification, dubbed ’pHonon’. Leveraging insights from pH-sensitive fluorescent proteins as pHluorins [35] and our own analysis of the Cryo-EM structure of GVs [12], we inserted pH-sensitive amino acids into the GvpC sequence. Histidine is a polar amino acid that is often involved in pH-dependent protein activity in nature [194–196]. The reason is that the chemical properties of the protonated and deprotonated histidine side chains are very different. At neutral pH the His side chain is uncharged, hydrophilic and apolar, while at low pH (<6) the side chain is positively charged, hydrophilic and polar. By replacing amino acids with histidine on the non-binding side of GvpC using structural insights from Cryo-EM [12, 169], we aimed to trigger an allosteric conformational change in GvpC that would alter the GV wall stiffness and, eventually, modulate nonlinear ultrasound scattering of engineered GVs in response to a change in pH.

We designed and screened a small library of rationally engineered GvpCs with histidine point mutations and show that one of these mutants exhibits a pH-sensitive behavior under hydrostatic pressure and nonlinear ultrasound imaging. We characterized this sensor, dubbed 'pHonon', to unravel its presumed mechanistic behavior, report its kinetics, and present its performance in combination with nonlinear ultrasound imaging. To demonstrate the in vivo potential of pHonon biosensors, we performed ultrasound imaging of phagolysosomal acidification in liver macrophages [142]. We show that pHonons are responsive to lysosomal acidification and report these changes in nonlinear ultrasound images. The parallel development of pHonon biosensors and volumetric imaging methods such as nonlinear sound-sheet microscopy [9] paves the way for deep and dynamic imaging of intracellular acidification in health and disease.

4.2. RESULTS

PH-SENSITIVE ACOUSTIC BIOSENSOR DESIGN AND SCREENING

To achieve a pH-dependent modulation of GV stiffness, we engineered the reinforcing protein GvpC with histidine substitutions on the solvent-facing side (Figure 4.1a). A recombinant GvpC gene was expressed in *Escherichia coli* (*E. coli*), while GVs were purified from their native species (*Dolichospermum flos-aquae*) and stripped of GvpC. The GvpA shell and heterologously expressed GvpC were reconstituted in vitro (Figure 4.1b) following a GV engineered pipeline developed by Lakshmanan *et al.* [11]

We assembled a small library of 9 GvpC variants with different histidine substitutions (Figure 4.1c). The locations of the histidine substitutions were chosen to be on the solvent-facing side of the GvpC, and determined by computational models of GvpC docking to GvpA [12]. The position of each substitution was conserved with respect to the start of each repeat, meaning that each histidine occupies roughly the same position in each repeat regardless of the original amino acids' physicochemical properties. Among the 9 different variants, only variant 5, dubbed 'pHonon,' exhibited an increased hydrostatic collapse pressure post-acidification (Figure 4.1d, Figure S4.1). pHonon has a total of 25 histidine substitutions, five in each repeat: H10, H14, H17, H28, and H32 (Figure 4.1e-h). A conceptual sketch of the acoustic pH sensor behavior is provided in Figure 4.1i.

CHARACTERIZATION AND MECHANISTIC STUDIES OF PHONON

In order to facilitate further engineering of pHonon biosensors, we explored the mechanism conferring pH-dependent GV shell strengthening. Contrary to wild-type and GVs without GvpC (ΔGvpC), pHonon biosensors exhibit an increased collapse pressure midpoint $Cp_{1/2}$ at pH 5 (Figure 4.2a-c) [12]. pHonon shows a continuous strengthening over a time span of ~20 hours, but 30% of the change in $Cp_{1/2}$ occurs during the first 30 minutes after exposure to pH 5 (Figure 4.2d). Experimentally, we observed batch variability with regards to pHonon $Cp_{1/2}$ values at 20 hours, with one outlier that reached a $\Delta Cp_{1/2}$ of 150 kPa. Despite positioning all histidine substitutions on the solvent-facing side of GvpC binding residues, pHonons consistently showed a lower collapse pressure at pH 7 than

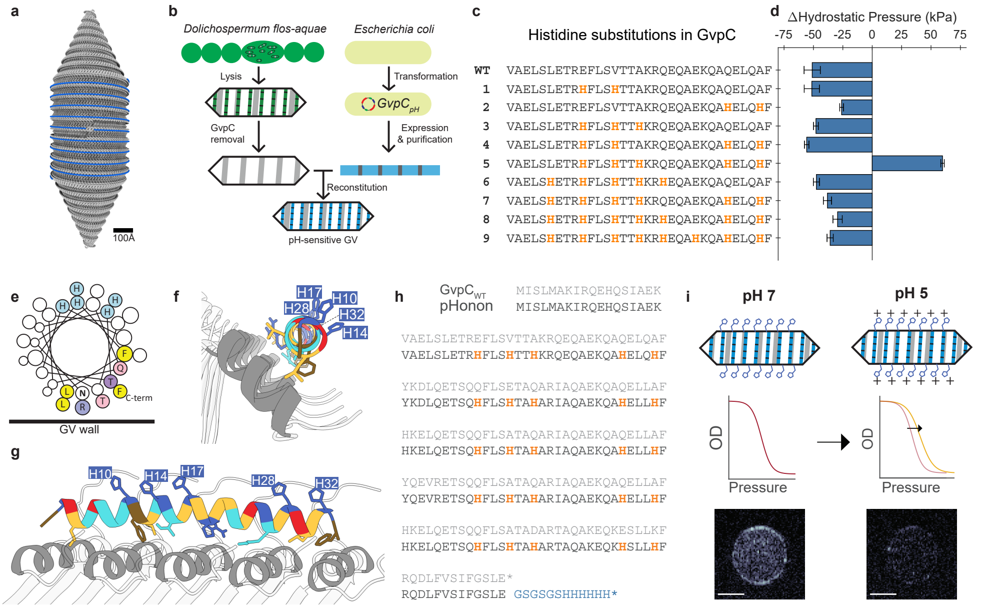

Figure 4.1: pH-sensitive GV design and screening. **a**, Molecular model of a GV; Grey: GvpA. Blue: GvpC. (adapted with permission[12]). **b**, Schematic representation of production and reconstitution of recombinant GvpC on a stripped GvpA shell from *D. flos-aquae*. **c**, List of GvpC variants; only the amino acid sequence of the first repeat of GvpC is shown. Histidine mutations are shown in yellow. **d**, Change in the midpoint of hydrostatic collapse pressure between pH 7 (n=3) and pH 5 (n=3) for each GV variant. **e**, Helical wheel representation of variant 5, further referred to as 'pHonon'. **f,g**, a 3D representation of a single repeat of pHonon bound to the GV wall (**f**, longitudinal plane; **g**, transverse plane). Amino acids are colored according to physico-chemical properties; Blue: Lys, Arg, His. Yellow: Met, Ile, Leu, Ala, Val. Light blue: Ser, Thr, Gln, Asn. Brown: Phe, Trp, Tyr. Red: Glu, Asp. **h**, Full amino acid sequence of wildtype *D. flos-aquae* GvpC (GvpC$_{WT}$) and pHonon GvpC. Yellow: histidine mutations. Blue: Gly-Ser linker and His-tag. **i**, Schematic overview of pHonon function: low pH results in a positive charge on His residues. The resulting change in GvpC binding and conformation leads to a stiffer GV. The increase in stiffness reduces the contrast in non-linear ultrasound images.

wildtype GVs and GVs reconstituted with his-tagged GvpC.

We used computational docking [197, 198] to gain insights into possible binding orientations of pHonon GvpC with GvpA at physiological and acidic pH (Figure 4.2e,f). To limit the computational complexity of the docking we used Cryo-EM data [12] to constrain the GvpA residues involved in binding to alpha-helix 2 (I37 to I46), and the GvpC binding residues to residues 4, 10, 11, 12, 14, 15, 17, 19, 23, 26, 28, 30, 32, 33 (highly conserved residues plus the newly introduced histidine mutations). At physiological pH, the highest scoring cluster (Figure 4.2e) has a very similar orientation to wildtype GvpC, as previously reported [12]. A higher docking score was observed for pHonon, which we primarily attribute to a slight tilt of pHonon GvpC, allowing E59 on GvpA2 to form hydrogen bridges with K2 on GvpC. Histidine point mutations point outward in relation to the GV

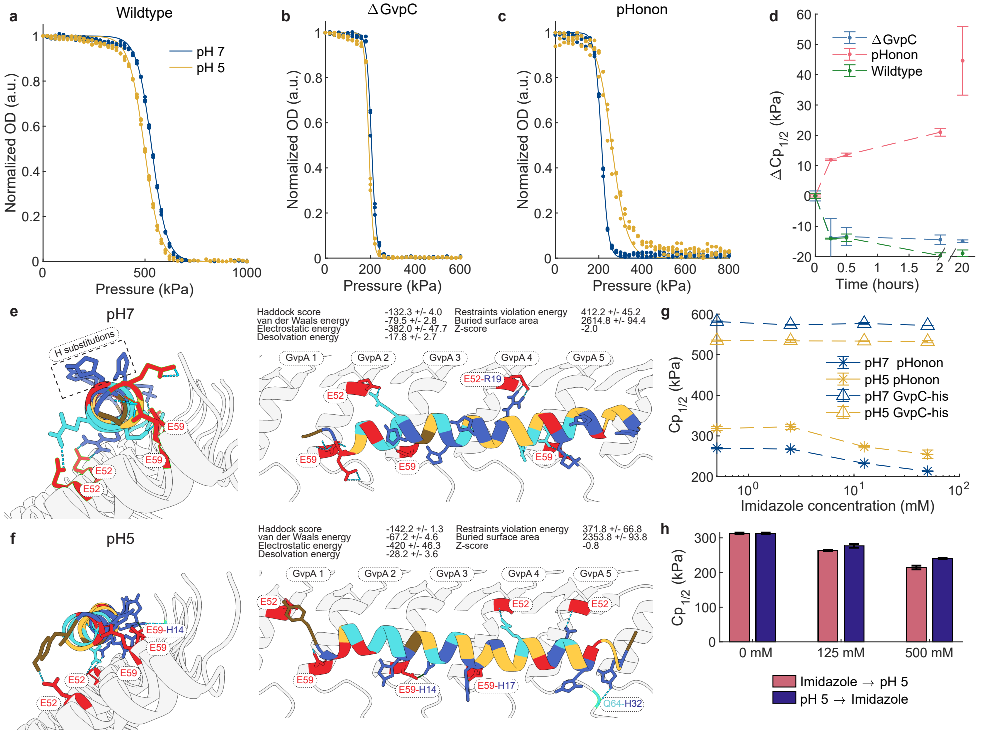

Figure 4.2: pHonon characterization and mechanism. **a-c**, Hydrostatic collapse pressure of wildtype GVs, ΔGvpC GVs and pHonon at pH 7 (blue) and pH 5 (yellow) (n = 3). The line is a sigmoidal fit. **d**, Time course of the hydrostatic collapse midpoint ($Cp_{1/2}$) of wildtype GVs (green), ΔGvpC GVs (blue) and pHonon (red). $Cp_{1/2}$ was determined using a weighted sigmoidal fit.**e**, Computational docking model of pHonon at pH 7 generated using HADDOCK 2.4. **f**, Computational docking model of pHonon at pH 5 generated using HADDOCK 2.4 **g**, $Cp_{1/2}$ for different concentrations of imidazole present during the reconstitution of GvpA and GvpC. **h**, Imidazole competition assay. The effect of imidazole competing with His substitutions in GvpC for binding- and interaction sites on the surface of GvpA is shown by comparing the effect of adding the competitor (imidazole) before the hypothetical allosteric conformation change (red) or after (blue).

wall as anticipated.

Acidic pH was simulated by manually changing histidine protonation states to fully protonated, i.e., with a positively charged side-chain. The highest score for pHonon at pH 5 shows GvpC rotated along its long axis (Figure 4.2f). Histidine substitutions now point parallel or inwards towards GvpA alpha-helix 2. Salt-bridges are predicted between E59 on GvpA2 and GvpA3 with H14 and H17 respectively. Hydrogen bridges are also predicted between GvpA1:E52-F1 , GvpA2:E59-K3, GvpA4:E52-Q22 and GvpA5:E52-K25. The hydrogen bridge GvpA5:Q64-H32 may be inaccurate as the N-terminal tail is unfolded and can take any orientation or conformation, but was here modeled as a rigid structure. A second high scoring structure was found with a similar orientation at pH 7. Follow-up studies should investigate whether both structures exist and are in competition, or whether only one of the two occurs experimentally.

To determine if the docking model at pH 5 (Figure 4.2f) is plausible, we performed two competition assays with the histidine analog imidazole to investigate interactions between histidine and GvpA. According to the most likely docking, adding imidazole at pH 7 should not interfere with any bond formation as none of the histidine substitutions show an interaction.

In the first competition assay (Figure 4.2g), we added imidazole during the reconstitution of GvpC-his and pHonon respectively. Increased concentrations of imidazole during the reconstitution process led to lower pHonon collapse pressure by 40 kPa (Figure 4.2g). Collapse pressures at pH 5 were measured to be consistently 40 kPa higher than the collapse pressure at pH 7. Imidazole had no effect on GvpC-his reconstitution. Based on the docking results, we did not expect imidazole to affect pHonon reconstitution. However, solubility might be a confounding factor in these measurements as solubility of GvpC-his at pH 7 is significantly higher than that of pHonon (Figure S4.2). We suspect that a considerable amount of pHonon GvpC may precipitate out of solution as urea is removed before it gets to bind GvpA. Interestingly, this result shows that we can control the initial collapse pressure of pHonon at pH 7 and therefore modulate the initial level of nonlinear scattering that a pHonon biosensor would have. Preparing pHonon sensors with different initial collapse pressures would enable multiplexing [27].

The second competition assay aimed to investigate whether the rotated GvpC docking is realistic (Figure 4.2h). If pHonon GvpC truly rotates at acidic pH, imidazole should compete with the newly formed salt-bridges (E59-H14, E59-H17) and diminish the characteristic strengthening of pHonon. Imidazole was added either before or after incubation at pH 5 for 20 hours, and the collapse pressure was evaluated. Adding imidazole before changing the pH resulted in a lower collapse pressure than adding imidazole after changing the pH (Figure 4.2h). We interpret this result as imidazole partially blocking the formation of salt-bridges (E59-H14, E59-H17), leading to a lower collapse pressure. When imidazole was added after changing the pH, the already formed bond blocked an interaction with imidazole and the resulting GV had a higher collapse pressure. While these computational docking results produce intriguing and stable structures, it is important to note that they remain largely speculative. For example, the assumption of a uniform pH - where all amino acids experience the same pH level - is almost certainly inaccurate. The biochemical microenvironment of each amino acid likely exposes it to significantly different pH levels. Furthermore, the assumption that a higher HADDOCK score corresponds to a stiffer GV may not hold true, as higher association energies do not necessarily imply changes in the protein's mechanical properties. Nevertheless, the proposed dockings provide a robust starting point for a more detailed exploration of the molecular mechanisms underlying pHonon.

DYNAMIC ULTRASOUND IMAGING OF ACIDIFICATION

We performed ultrasound imaging of pHonon and control nanoparticles (ΔGvpC GVs) embedded in 2% agarose phantoms using a nonlinear cross amplitude modulation pulse sequence (xAM)[20] (Figure 4.3a).

Linear ultrasound images revealed a similar echogenicity for both ΔGvpC GVs and pHonon across the pH 8 to 4 range (Figure 4.3b). Under nonlinear ultrasound exposure,

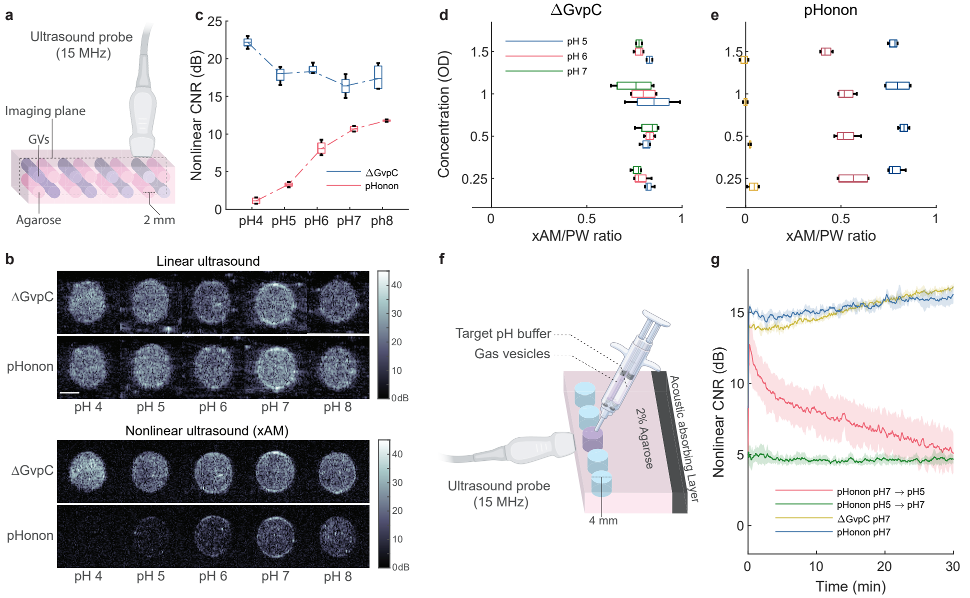

Figure 4.3: In vitro ultrasound characterization of pHonon. **a**, Schematic view of GV phantom imaging. **b**, Linear (top) and nonlinear (bottom) ultrasound images of Δ GvpC and pHonon GVs (OD = 1) after overnight incubation at the target pH and immobilized in 2% agarose. **c**, Nonlinear contrast-to-noise ratio (CNR) of ΔGvpC (blue) and pHonon (red) (n = 4). The region of interest(ROI) was selected over the entire well, and the noise level was determined using an equally sized ROI over a well filled with 2% agarose. **d**, The ratio of nonlinear (xAM)/linear (plane wave(PW)) CNR of phantom images of ΔGvpC and pHonon (n = 4) (**e**) for a range of pH values from 5 to 7 and concentrations from OD 0.25 to OD = 1.5. **f**, A schematic view of the kinetics measurement setup where a 4mm well in 2% agarose is filled from a dual-barrel syringe with equal volume OD = 1.5 GVs and 0.3 M McIlvaine buffer at the target pH. Imaging is performed at a frame rate of ~2 Hz and the probe is coupled with ultrasound gel. Blue wells are filled with demiwater to minimize reflection artifacts **g**, Nonlinear CNR over time with the injection and mixing of GVs with a target pH buffer at time 0 . pHonon is exposed to pH 5 (red) and subsequently to pH 7 (green). pHonon and ΔGvpC at constant pH (blue,yellow) were used as controls. (n = 5)

we observed a 10.6 ± 0.4 dB decrease in the non-linear contrast-to-noise ratio (CNR) of pHonon at pH 4 (Figure 4.3c) whereas control GVs remained echogenic through the pH range explored. The ecliptic behavior of engineered pHonon nanoparticles is unique and aligns with findings from collapse pressure measurements reported in (Figure 4.2). We also measured an increase of the CNR of ΔGvpC GVs of 4.8 ± 1.3 dB at pH 4. This drop in CNR coincides with a weakening of the pHonon nanoparticles observed in hydrostatic collapse pressure measurements (Figure 4.2a). Development of a quantitative ultrasound readout of pH levels in tissue is critical if we are to use pHonon for deep tissue imaging. Two physical effects in particular can lead to confounding effects: depth-dependent ultrasound attenuation in tissue and local variations in GV concentration. We developed a ratiometric measure, the cross amplitude over plane wave ratio (xAM/PW), that normalizes nonlinear scattering of GVs by their linear scattering which is proportional to GV concentration (Figure 4.3d-e). The xAM/PW ratios of control ΔGvpC GVs were constant for any GV concentration (OD 0.25 to 1.5) or pH (5 to 7) tested, as expected from a nanoparticle which is not pH sensitive (Figure 4.3d). For pHonon, xAM/PW ratios were independent of concentration but dependent on pH, with ratios varying from 0.80 at pH 7, 0.51 at pH 6, and 0.02 at pH 5 (Figure 4.3e).

We measured the switching kinetics of pHonon using a custom-built experimental setup (Figure 4.3f). In our experimental configuration, a 2% agarose phantom with 4 mm diameter open wells was molded as an acoustically transparent propagation medium. A 2x 1mL dual-barrel syringe allowed the rapid mixing of 0.3 M pH 5 McIlvaine buffer with GVs at OD 3 in 0.05% PBS, followed by the direct injection of this mixture into a well. Ultrasound imaging of the mixed solution was conducted at a 2 Hz framerate over 30 minutes to monitor changes in nonlinear contrast caused by the rapid exposure to a target pH value (Figure 4.3g). Upon quasi-instantaneous exposure to pH 5, the xAM CNR of pHonon decreased by 2.2 ± 1.1 dBs in 90s, 4.7 ± 0.3 dBs in 10 min and 6.1 ± 0.85 dBs in 20 min. We assessed the reversibility of our pH-sensitive GVs by exposing pHonon incubated at pH5 for 20 minutes to a quasi-instantaneous pH 7 buffer. We observed that xAM CNR remained constant at its pH5 value over the course of 30 minutes, indicating that our sensor design is not reversible between pH 7 and pH 5. ΔGvpC controls did not show any pH dependence as expected from imaging results.

IN VIVO ULTRASOUND IMAGING OF LYSOSOMAL ACIDIFICATION IN LIVER MACROPHAGES

After characterizing pHonon in vitro, we assessed the ability of pHonon biosensors to report on intracellular acidification in living tissue. We chose to perform dynamic imaging of phagolysosomal acidification in liver macrophages, as macrophage uptake of intravenously administered GVs is well documented [4, 142]. Kupffer cells, the liver's primary phagocytic macrophages, are primarily found in the sinusoidal spaces of the liver [199]. Foreign particles such as GVs are captured on the surface of Kupffer cells and subsequently phagocytosed. Next, the phagosome, now containing GVs, merges with lysosomes and gets acidified down to a pH of 4.5[200]. It is acknowledged that the pH within phagolysosomes drops from 7 to approximately 5 over the course of 10 to 20 minutes [201, 202]. Previously reported biomolecular ultrasound experiments also show that GVs circulating in the blood stream primarily accumulate in the liver [142]. Following intravenous injection, ultrasound contrast generated by GVs builds up in the liver over the course of 10 minutes before nearly disappearing after 60 minutes [142].

A jugular vein catheter was placed in anaesthetized C57BL/6 mice. After preparation of the animal, the left lateral lobe was found by using ultrafast Doppler. When possible, the caudate lobe was left out of the imaging plane. An xAM imaging sequence operating at a framerate of 2 Hz was used to record data for 45 minutes. After two minutes, the animal received a 150 μL bolus of either pHonon or control ΔGvpC GVs at OD = 50 through the catheter (Figure 4.4a).

For ΔGvpC GVs, we measured a rapid increase in xAM signal due to the bolus injection and the intravascular circulation of GVs in liver vessels. This was immediately followed by a slower increase in xAM signal in the liver plane of interest over 20 minutes post-bolus,

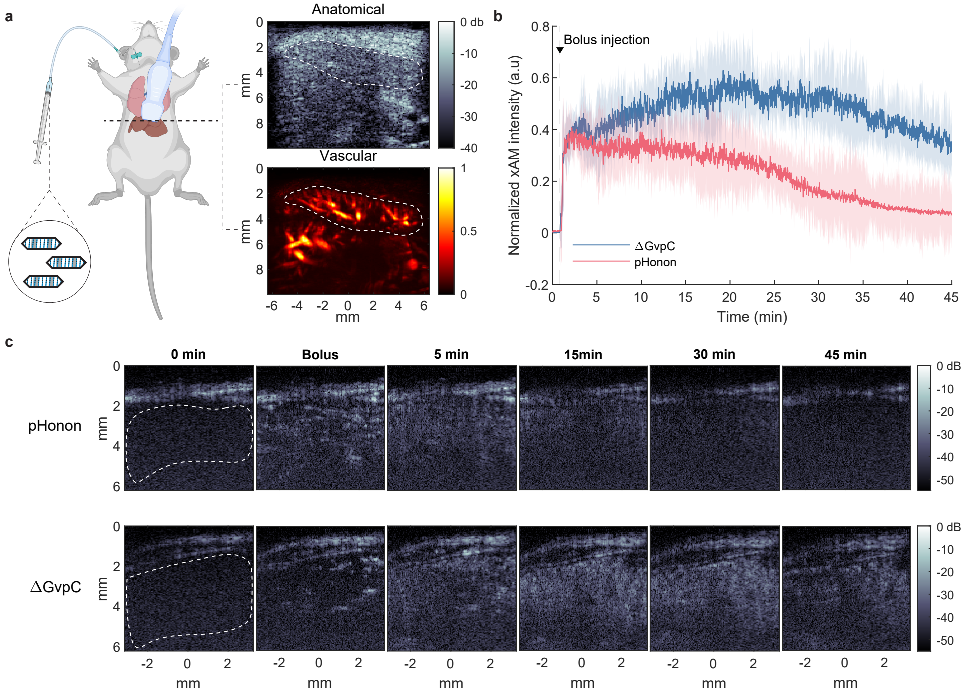

Figure 4.4: In vivo nonlinear imaging of lysosomal acidification in mice livers. **a**, Schematic showing the experimental setup. Shown top right is a representative anatomical (planewave) ultrasound image, and lower right a vascular (doppler) ultrasound image of a mouse liver. **b**, Average normalized nonlinear (xAM) signal intensity in the liver after bolus injection of ΔGvpC (blue) or pHonon (red) GVs (n = 4). **c**, Representative nonlinear ultrasound images of ΔGvpC (bottom) or pHonon (top) GVs in murine livers of two different animals at different time points. The ROI for these specific mice is indicated at t = 0 minutes with a white dotted line.

and followed by a slow decrease until the end of the 45 minute recordings (Figure 4.4b,c). This observation is in agreement with values found in literature [142].

For pHonon on the other hand, after the initial increase in xAM signal due to the bolus injection and the intravascular circulation of pHonon in liver vessels, we measured a steady decline of the xAM signal in the liver plane of interest until the end of the 45 minutes recordings. At the peak of the bolus, a "spotty" xAM signal was observed which we attributed to perfusion of the sinusoidal spaces. At this stage, GVs are thought to be confined in the vascular space rather than internalized in liver macrophages (Figure 4.4c). Over the next 5 minutes the xAM signal spread out through the plane as GVs get internalized into phagosomes. Phagosomal acidification is a biological process that takes place during and shortly after the initial lysosomal merging. In our experiments, pHonon biosensors clearly displayed a lower level of xAM signal compared to ΔGvpC GVs as of 15 mins.

Note that for ΔGvpC GVs, the loss of xAM signal after 20 minutes is caused by proteolytic degradation of the GVs rather than acidification. Together, our results indicate that phagolysosomal acidification takes place within the initial 20 minutes of the experiment, which is only slightly longer than the literature reports of acidification times of 17 min, 15 min, and 10 min respectively [200–202]. Altough it should be remarked that most of these studies found large variations in overal acidification times as well. This result is also consistent with the ecliptic behaviour of the sensor reported in Figure 4.3. Representative xAM images at different time points of the recording are reported in Figure 4.4c.

4.3. DISCUSSION

We successfully engineered an acoustic pH biosensor capable of reporting lysosomal acidification in ultrasound images. Our approach consisted of assembling a small library of nine recombinant GvpCs containing histidine point mutations, because this amino acid has the desired pKa for a sensor of endocytosis. We introduced histidine at positions that do not interfere with binding of GvpC to GvpA and screened for engineered GV variants that would show an increased shell stiffness when exposed to a target pH of 5, which is the acidic value reached in late phagolysosomes [200–203]. One of the engineered GV variants dubbed pHonon showed a 45 kPa increase in hydrostatic collapse pressure at low pH and was selected for further analysis. All other variants of the library showed weakening at low pH. Computational modeling provided insights into the potential sensing mechanism of our pH sensor. Protein docking scores indicated that at pH 7, pHonon GvpC residues form hydrogen bridges with GvpA . At pH 5, pHonon GvpC rotated along its axis to form salt bridges and hydrogen bridges with GvpA, further strengthening the shell . Interestingly, the addition of a histidine analog during pHonon reconstitution conferred a handle to modulate the biosensor shell stiffness at pH 7. Because the collapse pressure mid-point is directly related to the level of nonlinear scattering at pH 7, multiplexed biomolecular ultrasound imaging [27] could be investigated in the future. pHonon biosensors successfully reported pH variations in ultrasound images, exhibiting a 10.6 dB dynamic range between nonlinear ultrasound contrast at pH 7 and pH 4. In terms of kinetics, a 6 dB drop in nonlinear ultrasound contrast was measured in 20 min. This ecliptic sensor behavior is similar to pH-sensitive fluorescent proteins developed by Miesenbock et. al [35]. Normalizing the nonlinear acoustic response of pHonon with their linear acoustic response enabled ratiometric imaging of pHonon biosensors at pH 7, pH 6 and pH 5 respectively. Future work will evaluate this approach in an in vivo context to test the feasibility of parametric ultrasound mapping of pH levels in tissue. We demonstrated the potential of acoustic pH biosensors by imaging lysosomal acidification in liver macrophages. Following intravenous injection, the amplitude of nonlinear pHonon signals in the liver decreased steadily because of internalization in macrophages and exposure to low pH conditions. Control GVs showed a steady increase in nonlinear signal until 20 minutes before decreasing due to enzymatic protein degradation.

While we succeeded in engineering a pH-sensitive GV and imaged cellular acidification in vivo, pHonon should be seen as a first step towards a class of pH-sensitive GV-based biosensors. Our semi-rational engineering will serve as a basis for further optimization and the development of acoustic pH sensors with enhanced sensitivity, different pH transitions, potentially faster kinetics or reversibility, similarly to the successive improvements of optical pH sensors similarly to the successive improvements of optical pH sensors [35, 36, 203–206]. Interestingly, pHonon is the first GV-based sensor to show a shell strengthening, as opposed to a shell weakening seen in other GV-based biosensors [11, 30], providing a new mechanistic cue for GV engineering. While our current approach relied on a limited screening library, the recent development of high-throughput directed evolution assays for GV engineering [207] could expand this variant-space.

The exact pH sensing mechanism of pHonon biosensors remains to be elucidated. The present study reports plausible mechanisms based on a computational docking model and limited experimental data. Several questions remain open. For example, it would be interesting to investigate why structurally similar GvpC mutants of our library did not lead to pH-dependent shell strengthening. Current docking models seem to point at H14 and H17 as key positions, which is a combination of mutations that also occurred in variants 3 and 6-9 of our library. A combination of further mutagenic study, combined with computational models and high-resolution microscopy techniques might provide novel insights.

The clinical relevance of these pHonon biosensors was not the aim of this study but it will be interesting to revisit molecular ultrasound imaging methods such as ischemic memory imaging [34] and to explore new avenues for molecular ultrasound imaging such as monitoring of impaired lysosomal function in neurodegenerative diseases [208].

In conclusion, our results demonstrate that protein-based acoustic pH sensors can enable dynamic ultrasound imaging of intracellular acidification in intact opaque organisms and paves the way for biomolecular ultrasound imaging of organelle function.

4.4. METHODS

All chemicals were purchased from Merck (Sigma Aldrich) unless specified.

GAS VESICLE PRODUCTION

Dolichospermum flos-aquae (CCAP 1403/13F; Culture Collection of Algae and Protozoa) was cultured according to previously published protocol [160]. *D. flos-aquae* was cultivated for two weeks in G625 medium (5.84 mM $NaNO_3$, 224 μM KH_2PO_4, 304 μM $MgSO_3 \cdot 7H_2O$, 208 μM $Na_2SiO_3 \cdot 9H_2O$, 189 μM $NaCO_3$, 10 mM $NaHCO_3$, 245 μM $CaCl_3$, 31 μM citric acid and 3 μM EDTA) supplemented with BG-11 freshwater medium (Sigma Aldrich, C3061) at 25 °C, 120 rpm and 1% CO_2. The culture was illuminated at 5000 lux on a 14 h light, 10 h dark cycle. Cultures were allowed to settle for 24-48 hours, and the floating cell layer was collected. Harvested cells were lysed in the following buffer 10% v/v harvested cells, 10% v/v Solulyse^{TM} bacterial lysis agent (Genlantis, L200500), and 500mM sorbitol for 6-8h on a rotary mixer at room temperature. GVs were separated from the lysate by centrifugation at 350g for 12h. GVs are in the floating white layer, the subnatant was removed and discarded. The floating GV layer was topped up with phosphate buffered saline, pH 7.4 (PBS). The centrifugation and subnatant discard were repeated 4 times in total. GvpC was removed from GVs by 3 subsequent rounds of centrifugation at 350 g for 12 hours, subnatant discard and buffer top up, using PBS supplemented with 6 M urea as the buffer. GV concentration was measured by optical density measurements at 500 nm with a spectrophotometer (Ocean optics, STS-VIS).

CLONING METHODS

All gene sequences were codon-optimized for E. coli expression and inserted into pET28a plasmid via Gibson assembly. Enzymes were purchased from New England Biolabs and primers from Sigma Aldrich. The resulting plasmids were transformed into *E. coli* BL21(DE3) for expression.

HETEROLOGOUS EXPRESSION OF GVPC IN *E. coli*

Seed culture was prepared by inoculating LB with transformed colonies of BL21(DE3) and grown overnight at 37 °C, 220 rpm. The overnight seed culture was inoculated into auto-induction Terrific Broth (TB). Auto-induction TB medium is composed of 24 g/L yeast extract, 12 g/L tryptone, 2.9 g/L lactose and 7.6 g/L glucose[209]. The medium was sterilized via autoclave, and supplemented with 2% w/v lactose, 0.5% w/v glucose, and 100 μg/L ampicillin. Cultures were collected and centrifuged at 3000 g for 15 mins. The resulting cell pellet was resuspended in bacterial lysis buffer (50 mM Tris-HCl pH 8, 100 mM NaCl, 1% v/v Triton X-100, 10 mg/mL lysozyme) and rotated for 1-2 hours at room temperature. The lysate was centrifuged at 18000 g for 40 minutes, and the supernatant was discarded. Inclusion body solubilization buffer (6 M Urea, 50 mM Tris, 100 mM NaCl) was used to resuspend the centrifuged pellet, and the resuspension was centrifuged at 18000 g for 40 minutes. The His-tagged GvpC proteins were purified using Ni-NTA affinity chromatography (HisPur, Thermo Fisher, 88221) following the manufacturer's protocol. Protein concentration was determined using Bradford assay (Thermo Fisher, 23238) according to the manufacturer's protocols, bovine serum albumin was used to make the standard curve.

RECONSTITUTION OF GV WITH GVPC

GvpC was re-added to ΔGvpC GVs in a 20x mole excess (GvpC:GvpA) according to the formula $20 \times OD_{500\,nm} \times 198\,nM \times$ volume (in liters) of GVs = nmol of recombinant GvpC[160]. The ΔGvpC GV and GvpC protein mixture was dialyzed twice against 2 L of PBS with a 6 kDa MWCO dialysis membrane. followed by 3 rounds of centrifugation at 350 g for 12 hours, subnatant discard and buffer top-up, using PBS as the buffer.

HYDROSTATIC COLLAPSE PRESSURE MEASUREMENTS

Hydrostatic collapse pressures were determined using the setup outlined previously [160]. GVs were diluted to an $OD_{500\,nm}$ of 0.2 with the appropriate buffer. McIlvaine buffer (citric acid, Na_2HPO_4) was used for all pH-dependent collapse pressure studies. A pressure controller (PC series; Alicat Scientific) connected to a 1.5 MPa nitrogen gas source was used to vary the hydrostatic pressure in a flow-through cuvette (Hellma, article no.1767001510-40). A pressure step of 20 kPa and an equilibration time of 5 seconds were used before the optical density at 500 nm was recorded using a spectrophotometer (STS-VIS; Ocean Optics). The pressure controller and spectrophotometer were controlled using MATLAB. All measures were done in triplicate and the average and 1 standard deviation are reported.

COMPUTATIONAL DOCKING

A docking model was generated using the online environment (https://rascar.science.uu.nl/haddock2.4/) for HADDOCK 2.4 [197, 198]. Previously published atomic models for docking of GvpC to GvpA[12] were retrieved (https://doi.org/10.5281/zenodo.6867443) and used as a starting point for our docking simulations. To transform GvpC from the published model to pHonon GvpC histidine mutations were programmed in ChimeraX [210] using the 'swapaa' command. Rotamers were left to their default settings. Active residues for GvpA were limited to residues 51–61 of GvpA, similar to previously published computational docking methods for GvpC [12]. For GvpC, active residues were residues 4, 10, 11, 12, 14, 15, 17, 19, 23, 26, 28, 30, 32, 33, and selected by adding the histidine mutations to the residue list used in a previously published docking [12]. To simulate docking at pH 7 all HADDOCK settings were set to default. To simulate pH5 the histidine protonation states of GvpC were manually set to HIS+ in the HADDOCK environment. Docking clusters were displayed in ChimeraX and hydrogen bonds between GvpA and GvpC highlighted with the 'hbonds' command.

COMPETITION ASSAYS

To investigate the effect of initial imidazole concentration during reconstitution, imidazole concentration in the reconstitution mixture was varied. Purified GvpC was subjected to several rounds of dialysis against 6M Urea and PBS to reduce the imidazole concentration to < 10 μM. Dialyzed and purified GvpC was mixed with imidazole to achieve reported final imidazole concentrations. This mixture was then combined with ΔGvpC GVs in a 20x mole excess and dialyzed for 2 rounds against 2 L of PBS.

pH-dependent competition of GvpC and imidazole was investigated by switching the order of the pH drop or imidazole addition of the pHonon GV solution. Imidazole was added to the pHonon GV solution to the reported final concentrations. The pH was dropped by adding 0.1M citric acid into the pHonon GV solution to reach pH 5. The GV solution was incubated for 15 minutes at each step, and the hydrostatic pressure was measured after both pH drop and imidazole addition.

IN VITRO ULTRASOUND IMAGING

All ultrasound imaging was performed with a Verasonics Vantage 256 scanner combined with an L22-14vX Verasonics ultrasound probe (Verasonics, Kirkland, Washington, USA), with a specified pitch of 0.1 mm, an elevation focus of 8 mm, an elevation aperture of 1.5 mm and a center frequency of 18.5 MHz. For the immobilized in-vitro GV images 2% agarose phantoms were prepared in Milli-Q or PBS using custom 3D-printed molds. GV samples were diluted 2x in 2% low melting-temperature (LMT) agarose and loaded into the phantom wells. GV samples were matched at $OD_{500\,\text{nm}}$ of 2. A well filled with 1% LMT agarose was used to determine background intensity in every frame. The cross-amplitude modulation (xAM) method for non-linear imaging of contrast agents was used [20]. xBmode images were acquired using a single cross-propagating plane-wave transmission. Plane wave images were beamformed by coherent compounding of the two mirrored plane waves from the xAM pulse sequence. xAM images were acquired using three separate transmits, 2 mirrored plane waves and a cross propagating wave. Contrast-to-noise values were determined by taking the log-compressed ratio of the signal in a representative circular region of interest (ROI) in the well, and a representative noise ROI in a well filled with 1% LMT agarose. Images were displayed with an equalized noise-floor. All measures were done in quadruplicate and the average, 25% and 75% and minimum and maximum are reported.

To measure pH dependent kinetics of pHonons, a 2% agarose phantom with 4 mm wells was prepared. A dual-barrel syringe (2 x 1 mL) with a mixing tip was filled with GVs ($OD_{500\,\text{nm}} = 2$, 0.5% PBS) in one barrel and 0.3 M McIlvaine buffer in the second barrel. Buffer capacity was calibrated to be pH 5 after injection into the well of the phantom. The ultrasound probe was positioned against the phantom and acoustically coupled using ultrasound gel. GVs and pH buffer were injected into a phantom well through the syringe mixing tip. Images were recorded at an acoustic pressure of 600 kPa, with a framerate of 2 Hz for 30 minutes.

IN VIVO IMAGING OF PHAGOLYSOSOMAL ACIDIFICATION

C57BL/6 mice of ages between 3 and 5 months were anesthetized with Isoflurane (5% for induction, 1% for maintenance) and placed on a heating pad with loop control from a temperature probe and breath monitoring. The animal was equipped with a foot sensor to measure pulse (MouseStat and Physio Suite from Kent Scientific, Torrington, Connecticut, USA). Two areas were shaved and depilated: the area over the right jugular vein to prepare for catheterization and a 4cm x 3cm area from the ribs down to allow for artefact-free imaging from the hair. The area over the right jugular vein was cleaned 3:3 times with saline solution and a mix of chlorhexidine/cetrimide (Hibicet, Molnlycke Health Care, Gothenburg, Sweden). After skin incision and resection of fatty tissue, the jugular vein was isolated and a catheter was placed inside and fixed with sterile non-resorbant sutures. The catheter was flushed with a mix of saline and heparin to prevent blood clots.

Then the skin was sutured. The mice were hydrated during the imaging session through subcutaneous bolus of 0.1 mL of saline solution. Ultrasound gel was applied in the abdominal area as a coupling medium and an L22-14Vx ultrasound probe (as described in 4.4) was placed medial to the sternum. Through the use of ultrafast Doppler, the field of view was focused on the lateral left lobe and a plane containing a representative vascular tree was isolated. Non-linear xAM images were generated using 3 compounded angles (12°, 15°, 21°). A baseline ultrasound signal was established for 2 mins before a 150 µL bolus of GVs at $OD_{500\ \mathrm{nm}}$ of 50 in PBS was administered through the vein catheter.

The catheter was flushed with saline to flush the dead volume in the catheter tubing. A maximum volume of 200 μL was injected per experiment. Nonlinear images were acquired for 45 mins post-injection at a frame rate of 2 Hz.

Breathing creates a significant motion below the sternum, leading to motion artifacts. Since we are imaging in 2D, out-of-plane motion cannot be compensated for, and the imaging plane changes entirely during some periods of the breathing cycle. As our frame rate is high enough to image the relatively slow phagocytosis of the GVs and their pH-induced behavior changes, we elected to compensate for the motion by using a frame-rejection approach. The liver was manually segmented in the linear image extracted from the main pulse of the xAM and the average signal intensity within the ROI was calculated. A peak detection algorithm was used to find the signal intensities with the large deviations from the baseline. Frames were rejected at an intensity level of 50% of the average intensity of the detected peaks. To conserve uniform sampling of the nonlinear signal, rejected frame intensities were linearly interpolated from their previous and next samples. The resulting time-intensity curves were smoothed using a 5-point moving average window and normalized with respect to an average signal of the baseline set to zero and dividing by the signal maxima. Signal traces from each experimental group (pHonon n = 4, ΔGvpC n = 4) were averaged at each time point and plotted.

KEY RESOURCE TABLE

Resource	**Identifier**
Haddock 2.4[197, 198]	https://wenmr.science.uu.nl/haddock2.4/
ExPASy[211]	https://www.expasy.org/
ChimeraX 1.7[210]	https://www.rbvi.ucsf.edu/chimerax/

Generated plasmids	**Source**
pET28a-GvpC-His6	This study
pET28a-GvpC-H10.H14-His6	This study
pET28a-GvpC-H28.H32-His6	This study
pET28a-GvpC-H10.H14.H17-His6	This study
pET28a-GvpC-H10.H14.H28.H32-His6	This study
pET28a-GvpC-H10.H14.H17.H28.H32-His6	This study
pET28a-GvpC-H6.H10.H14.H17.H20-His6	This study
pET28a-GvpC-H6.H10.H14.H17.H28.H32-His6	This study
pET28a-GvpC-H6.H10.H14.H17.H20.H28.H32-His6	This study
pET28a-GvpC-H6.H10.H14.H17.H20.H24.H28.H32-His6	This study
Bacterial strains	**Source**
Dolichospermum flos-aquae CCAP 1403/13F	CCAP
Escherichia Coli BL21 (DE3)	Novagen

4.5. SUPPLEMENTARY SECTION

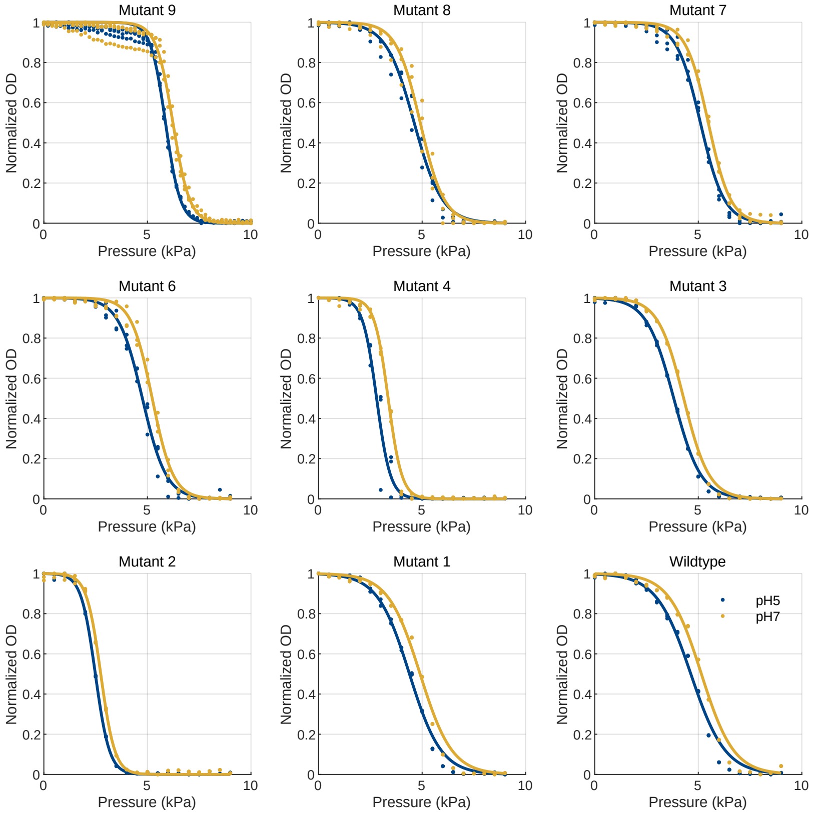

Figure S4.1: Fitted collapse pressure curves at pH7 (yellow) and pH5(blue) with raw data as scatter plot (n=3).

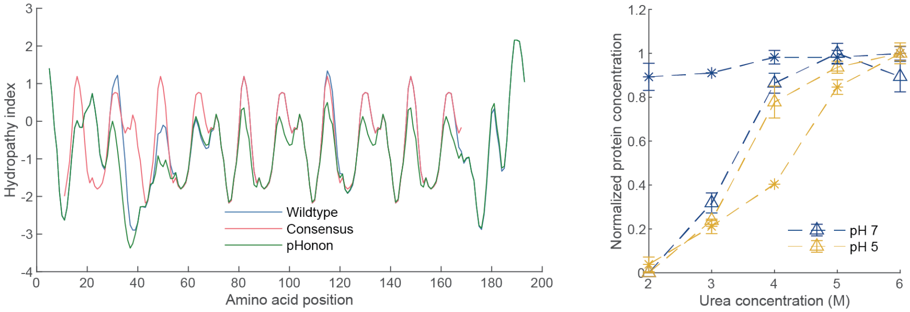

Figure S4.2: Solubility of GvpC. **a**, kyte-doolittle hydropathy index for wildtype (blue) GvpC, GvpC with a consensus sequence in each of the 5 repeats (red), and pHonon GvpC (blue). pHonon is significanlty les hydropathic than wtGvpC. **b**, normalized protein concentration measurements of pHonon (△) and GvpC-his (*) when reducing the urea concentration at pH5 (yellow) and pH7 (blue). Especially at pH7, there is almost no precipitation of GvpC-his above 2M urea, while pHonon GvpC is almost fully precipitated at 2M urea.

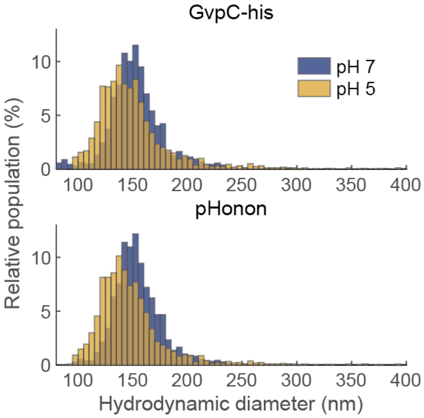

Figure S4.3: TRPS measurements of GvpC-his GVs and pHonon, at pH7 (blue) and pH5 (yellow).

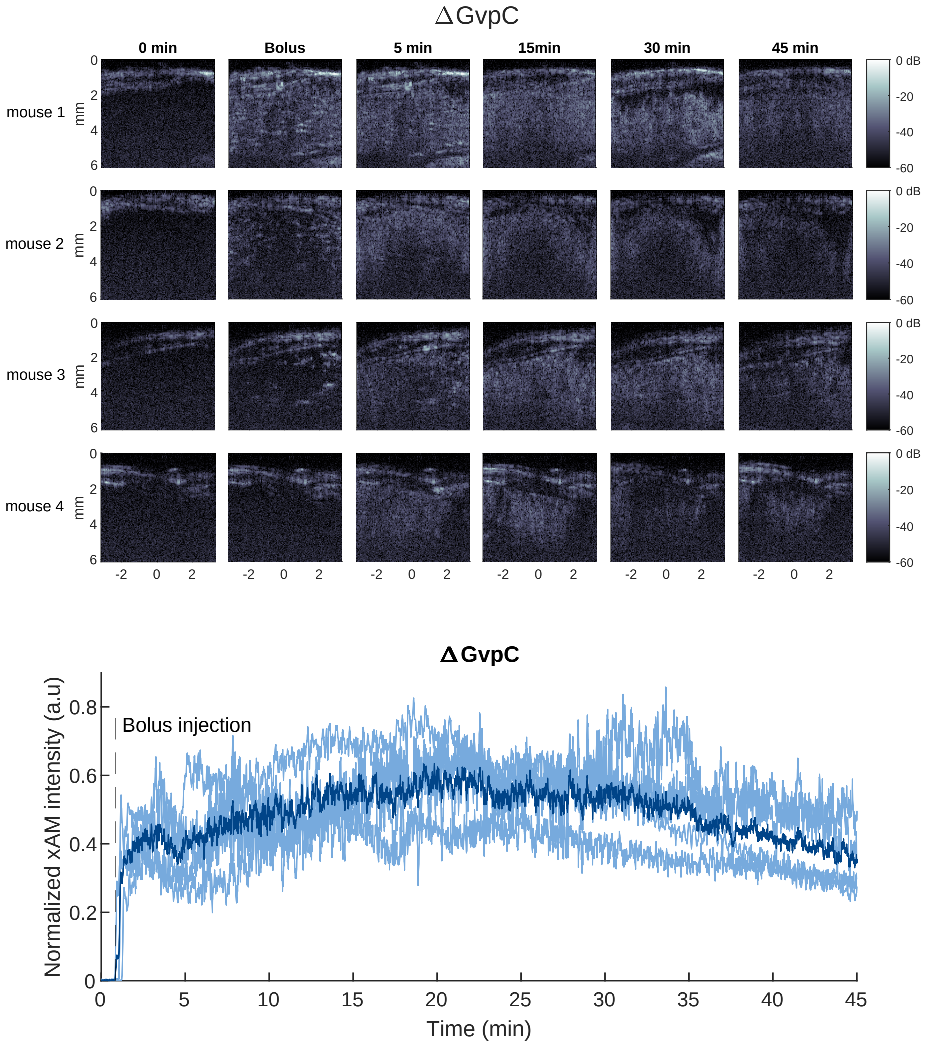

Figure S4.4: Representative images of liver and time-intensity curves for each separate mouse, with the dark line representing the mean, after injection with ΔGvpC for each of the four mice at different time-points.

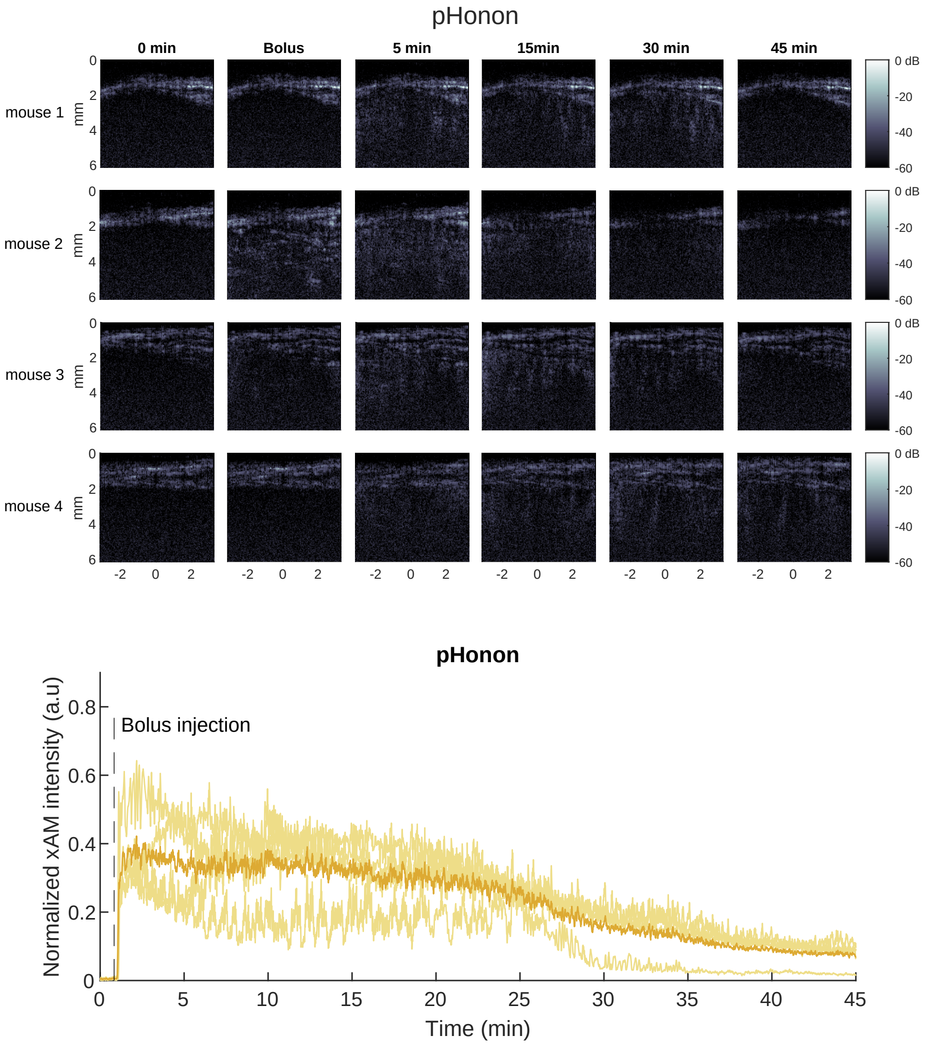

Figure S4.5: Representative images of liver and time-intensity curves for each separate mouse, with the dark line representing the mean, after injection with pHonon for each of the four mice at different time-points.

5

ACOUSTIC PROPERTIES OF AGGREGATED HOLLOW PROTEIN NANOSTRUCTURES

Functional ultrasound imaging has recently emerged as a breakthrough hemodynamic imaging method capable of visualizing whole-brain neural activity with high spatiotemporal resolution. However, deep and transcranial monitoring of brain activity remains a challenge due to skull-induced attenuation of ultrasound waves. Clinically approved microbubble (MB) contrast agents have been successfully used to raise hemodynamic contrast through the skull, but they introduce significant fluctuations to ultrasound signals and suffer from limited circulation times. A new class of genetically encoded acoustic contrast agents based on gas vesicle (GV) protein nanostructures has recently been shown to withstand higher acoustic pressures and provide smoother hemodynamic contrast than MBs. Despite these advantages, GVs are less echogenic than MBs and are taken up by liver macrophages, which limits their circulation time. Here, we take the first step toward the development of an engineered GV-based ultrasound contrast agent with enhanced echogenicity and prolonged circulation time. We show that aggregation of GVs leads to an increase in both linear and nonlinear ultrasound contrast compared to unaggregated GVs. Additionally, we demonstrate that periodic aggregation leads to a four-fold increase in nonlinear ultrasound contrast over unaggregated GVs and a two-fold increase over aperiodic aggregates. An increase in CNR was found for periodic aggregates with alginate with both ΔGvpC GVs and wild-type GVs . Linear contrast is also increased in both cases, but more so for aperiodic aggregates at frequencies up to 55 MHz. Finally, we demonstrate that it is possible to encapsulate GVs in a hydrogel matrix while maintaining the increase in contrast consistent with aggregation.

Terwiel, D., Van Leeuwen, J., Silvera, L., Garbin, V., Franceschini, E. & Maresca, D., *manuscript in preparation*

5.1. INTRODUCTION

Functional ultrasound (fUS) imaging has recently emerged as a technique for hemodynamic imaging, enabling researchers to visualize neural activity across the entire brain with remarkable spatiotemporal resolution [212]. This advancement is particularly significant in the field of neuroscience, where understanding brain function in real-time is crucial for both basic research and clinical applications. fUS imaging has several advantages over traditional imaging modalities, such as functional magnetic resonance imaging (fMRI), including greater portability, lower cost, and significantly higher temporal resolution, which is an order of magnitude greater than that offered by fMRI [46, 213–218].

Despite its potential, transcranial fUS imaging is limited in clinical and research applications due to the aberrations and attenuation caused by the skull. Skull-induced distortion and attenuation can render subtle variations in blood flow indistinguishable from background noise, thus hindering the accurate assessment of neural activity [219]. While skull-induced aberration may be corrected through techniques such as ray-tracing [220], the only way to address skull-induced attenuation is to increase the scattering amplitude of contrast agents or to decrease the attenuation of the skull. Consequently, many current fUS implementations necessitate invasive procedures, such as craniotomies [1], thinned-skull preparations [62], or the use of acoustically transparent windows [43], which can be impractical and pose additional risks to patients.

To overcome these challenges, the application of ultrasound contrast agents has been explored as a means to enhance the visibility of vascular structures and improve signal quality in transcranial fUS imaging. Clinically approved lipid-shelled microbubbles (MBs) have demonstrated a capacity for significant hemodynamic signal enhancement; however, they come with notable drawbacks. Specifically, MBs introduce substantial fluctuations to ultrasound signals, reducing the sensitivity of fUS imaging, and are characterized by limited circulation times due to gas escape and organ retention [94, 221, 222].

In response to these limitations, a novel class of hemodynamic ultrasound signal enhancers has been developed based on genetically encoded gas vesicles (GVs) [4]. GVs are air-filled protein nanostructures, typically ranging from 100 to 600 nm in length [126], and have been shown to produce robust ultrasound contrast across the frequency ranges used in medical ultrasound. Importantly, the unique biochemical composition and genetic encodability of GVs provide opportunities for engineering their mechanical, acoustic, and physical properties, allowing for the creation of versatile and widely deployable contrast agents [19, 55].

Despite their potential, GVs exhibit lower echogenicity compared to MBs, primarily due to their smaller size. This limitation is compounded by the fact that intravenously injected GVs are rapidly taken up by liver macrophages, further constraining their circulation time [142]. To address these challenges, we propose a novel approach to enhance the echogenicity and circulation time of GVs through controlled aggregation and subsequent encapsulation of GVs. Previous research has indicated that GV aggregation can improve ultrasound contrast [4, 223], but we hypothesize that periodic aggregation may maximize ultrasound contrast effects. Periodic aggregation could shows parallels to the behaviors observed in phononic crystals, where periodically arranged inclusions can manipulate acoustic waves through complex interactions that include multiple scattering reflections, nonlinear wave propagation, and resonance effects [224–226]. Alternatively, GV aggregation might produce effects akin to those observed in ultrasound backscatter from erythrocytes [223, 227]. Moreover, periodic aggregation of GVs can be achieved through depletion interactions with larger molecules, such as those used to form hydrogels. Alginate hydrogel encapsulation, commonly employed in biomedical and pharmaceutical applications, can immobilize particles, enhance biocompatibility, and extend the circulation time of therapeutics within the bloodstream [228–230].

The primary goal of this research is to investigate various GV aggregation strategies and their impact on the resulting nonlinear acoustic signals. We will evaluate the effects of alginate encapsulation on GVs in mesoscale beads and utilize a flow-focusing microfluidic approach to encapsulate GVs in sub-millimeter-scale alginate beads. Through acoustic imaging and optical analysis using phase contrast microscopy, we aim to characterize the properties of these engineered ultrasound contrast agents and assess their potential for future applications in functional ultrasound imaging.

5.2. RESULTS

GV AGGREGATION CHARACTERIZATION

GVs without GvpC (harmonic GVs, hGVs) were aggregated using two distinct methods: fusion proteins (biotin and streptavidin) and depletion interactions with alginate. Negative stain transmission electron microscopy (TEM) images of harvested GVs suspended in 2 mg/ml alginate indicated that alginate promotes periodic GV aggregation, while biotinylated GVs with a 10,000 molar excess of streptavidin displayed random aggregation patterns (Figure 5.1a). The periodicity of these aggregates was quantified using normalized angular distributions presented in polar histograms. The standard deviation of angles for GVs aggregated in alginate (±13.7°, ±6.9°, ±3.7°) was approximately six times lower than that of the biotin-streptavidin aggregates (±48.8°, ±47.4°, ±45.4°). wildtype GVs (GVs with bound GvpC, WT GVs) exhibit the increased alignment when aggregated through depletion interactions (Figure S5.4)

Negative stain TEM imaging, while useful, is invasive as it introduces uranyl salts, which can cause unwanted aggregation and interact with alginate to promote crosslinking. To more accurately assess aggregate sizes, we employed Tunable Resistive Pulse Sensing (TRPS) (Figure 5.1b). Peaks are observed at 150 nm for all samples and at 500 nm for Biotin-streptavidin and alginate mediated aggregation. A significant increase in particle counts exceeding 1.5 μm was observed for aggregated GVs, with biotin-streptavidin aggregation contributing the highest counts in this range.

The largest particle population measured had a hydrodynamic diameter of 150 nm, consistent with published values for individual GVs [12, 161, 169]. Aggregated GVs, corresponding to the second observed peak, exhibited a minimum hydrodynamic radius of approximately 500 nm, corresponding to roughly 37 standard-sized GVs, irrespective of whether they were aggregated periodically. Observations indicated a shift in the relative population toward larger particles across a diameter range from 500 nm to 4000 nm, suggesting a broad distribution of aggregate sizes. Biotin-streptavidin interactions yielded the largest aggregates, as seen in both TEM images, and in the relative probability of particles over 1.5 μm

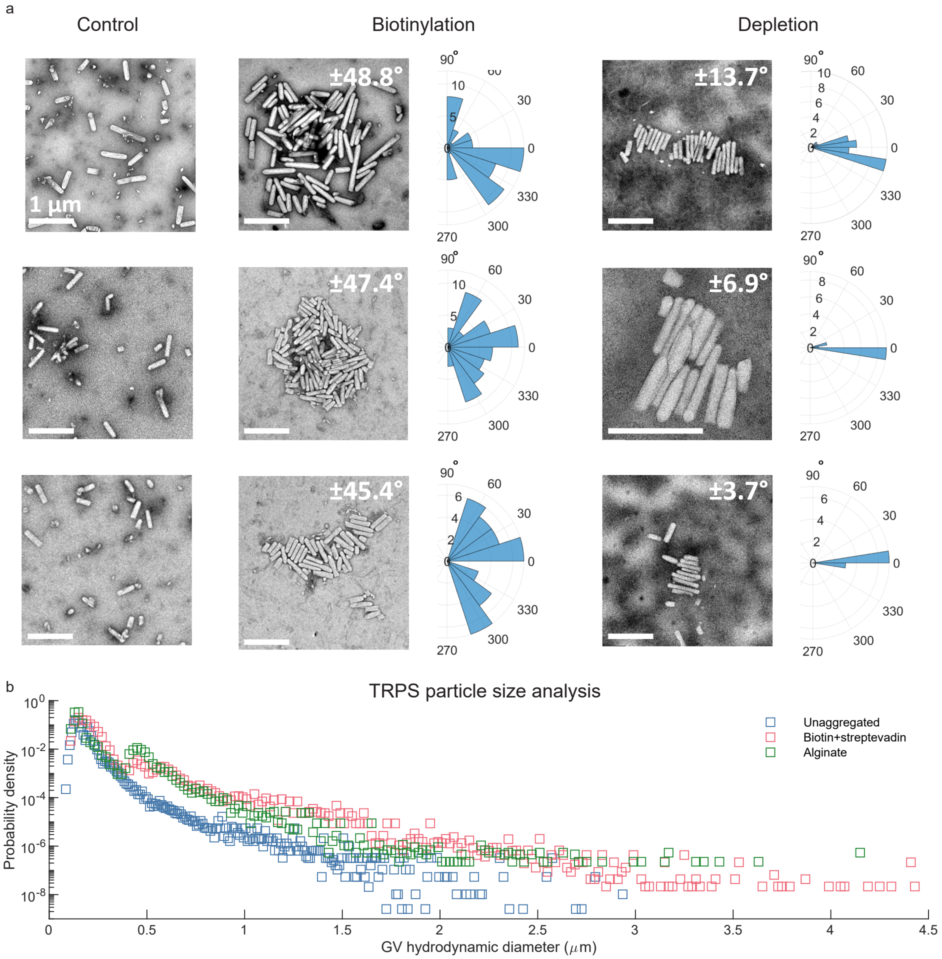

Figure 5.1: Engineered aggregation of purified GVs. (a) hGVs in HEPES buffer (control) show minimal aggregation when observed with TEM. Biotinylated hGVs with a 10.000 molar excess of streptavidin are aggregated in random configurations, demonstrated by the wide distribution of GV angles in the polar histograms. hGVs in 2 mg/ml alginate are aggregated periodically, which is confirmed by the narrow distribution of angles centered around 0° in the polar histogram. Values at the top right of each TEM image indicate the standard deviation of angles in each assembly. All control and biotinylated images were digital zooms from the original images. (b) Scatter plot of probability distributions resulting from TRPS measurements of 1500 particles per sample.

AGGREGATION-INDUCED NONLINEAR CONTRAST ENHANCEMENT

Previous studies have established that aggregation can enhance contrast when induced through biotin-streptavidin crosslinking [4]. We hypothesized that radially stacked periodic GV aggregates would exhibit even higher echogenicity. To test this, we immobilized aggregated and non-aggregated hGVs in agarose phantoms and imaged them using

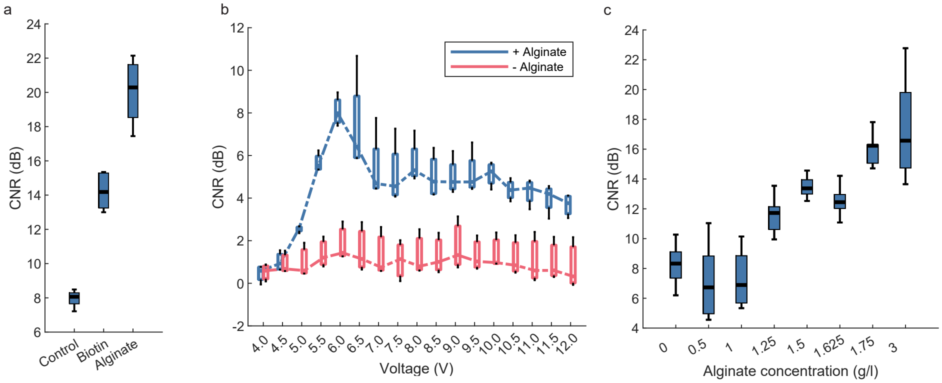

Figure 5.2: Non-linear contrast enhancement from aggregation (a) average CNR (n=8) of aggregated hGVs measured in agarose well phantoms filled with GVs at OD = 2 and imaged using an xAM pulse sequence scheme. (b) Average CNR of periodically aggregated wild-type GVs (wtGVs) and unaggregated wtGVs (n=4) at different imaging voltages, and (c) representative images.

a nonlinear (xAM) technique (Figure 5.2a). Randomly aggregated GVs showed an approximate 6 dB increase in contrast over control samples. In contrast, periodically aggregated GVs achieved a nonlinear ultrasound contrast enhancement of 12 dB (from 8.0 dB to 20.1 dB), underscoring the substantial impact of aggregation periodicity on the nonlinear contrast produced by hGV aggregates.

Typically, WT GVs do not exhibit nonlinear contrast due to their increased stiffness, which prevents significant buckling under collapse pressure. However, we noted that periodically aggregated WT GVs suspended in 2 mg/ml alginate demonstrated a marked increase in nonlinear contrast over controls (Figure 5.2b). This enhancement was observed at transducer transmit voltages ranging from 5 V to 12 V, with a peak contrast difference of approximately 6 dB at 6 V. Beyond this voltage, a decline in CNR was noted as GVs began to collapse, plateauing at 5 dB for WT GVs in alginate. These findings indicate that alginate-induced periodic GV aggregation significantly boosts the nonlinear ultrasound contrast generated by both hGVs and WT GVs, presenting an innovative method for designing GV-based biosensors, where the switch between linear and nonlinear scattering is crucial for functionality. CNR increase is dependent on alginate concentration (Figure 5.2b). It can be observed that the threshold alginate concentration for OD = 2 GV depletion interactions is roughly 1.25 mg/ml, as the contrast increase is 3 dBs compared to lower concentrations and the control. At 1.75 mg/ml of alginate, a plateau in contrast enhancement is reached.

Additionally, we examined linear scattering enhancements. GVs were immobilized in agarose slabs and imaged using linear B-mode ultrasound, scanning the imaging plane with single transducer elements at their respective centre frequencies. Similar to nonlinear imaging outcomes, aggregated GVs demonstrated enhanced linear backscatter signals compared to non-aggregated GVs (Figure 5.3). Notably, biotinylation produced a higher CNR than depletion interactions at 10 MHz and 22 MHz, a reversal of the nonlinear scenario, although not at 55 MHz. This behaviour may be attributed to the larger aggregates formed during biotinylation (Figure 5.1). Scattered power scales linearly with particle concentration, but backscattered power scales super-linearly with particle size, leading to more intense backscatter from larger aggregates [231]. We also observed a frequency-dependent increase in CNR, with measured contrast enhancements for depletion or biotinylation being 4.1 dB and 8.2 dB at 10 MHz, 5.3 dB and 9.7 dB at 22 MHz, and 18.3 dB and 18.1 dB at 55 MHz, respectively.

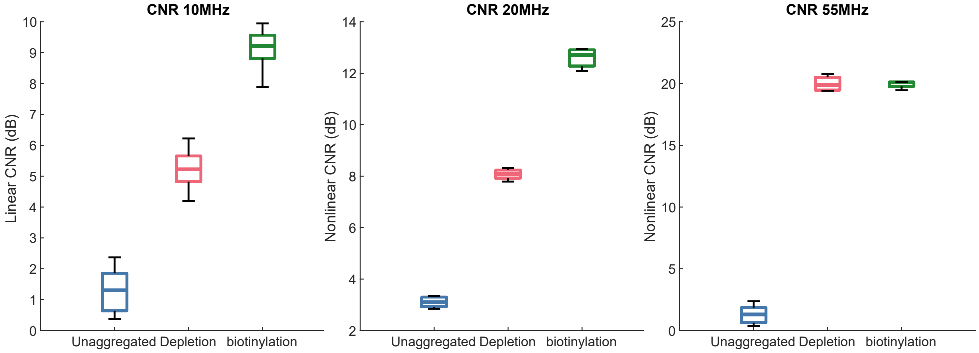

Figure 5.3: linear contrast enhancement Linear CNR in 1% agar slabs at different imaging frequencies. CNR's were derived from images generated line-by-line from a single element transducer. n = 3 images were used for each sample.

GV ENCAPSULATION IN ALGINATE BEADS

Following the successful aggregation of GVs and observation of ultrasound contrast enhancements, we proceeded to encapsulate the periodically aggregated GVs. This encapsulation was performed at two scales: initially, mesoscale beads were created by using a syringe and dropping small droplets of a mixture of 1.75 mg/ml alginate and GVs in a calcium bath, followed by microscale beads generated with a microfluidic chip.

Ultrasound imaging revealed that the mesoscale beads were teardrop-shaped, measuring approximately 2 mm in diameter (Figure 5.4). The beads containing hGVs were visible in both linear B-mode and nonlinear xAM imaging modes, while those with WT GVs appeared only in the linear imaging mode. Empty alginate beads were not detected in the nonlinear imaging mode and only faintly appeared in linear imaging.

In the microfluidic setup, we observed spherical, monodisperse droplets approximately 125 μm in size within the chip under an inverted optical microscope. The droplets were produced at a rate of 600 beads per second (Figure 5.5a). After gelation, the microscale beads exhibited various shapes, confirmed through phase contrast microscopy (Figure 5.5b). The average final bead sizes were 241 μm for beads without GVs, 248 μm for those with WT GVs, and 245 μm for those with hGVs. The presence of GVs within the beads was indicated by the positive phase contrast observed, as GVs appeared white against a transparent background. Conversely, beads without GVs did not exhibit this white contrast. Notably, higher concentrations of GVs resulted in larger and more crowded final beads (Figure S5.7,Figure S5.6)

To sum up, ultrasound imaging of mesoscale beads verifies the successful encapsulation of WT and hGVs, and phase contrast microscopy images corroborate the encapsulation of WT and hGVs within microscale alginate beads. We have illustrated a straightforward proof-of-concept for microfluidic encapsulation of GV aggregates in alginate hydrogel. Regrettably, the ultrasound imaging of these microscale beads has not yet yielded conclusive results and continues to be the primary obstacle in advancing this research.

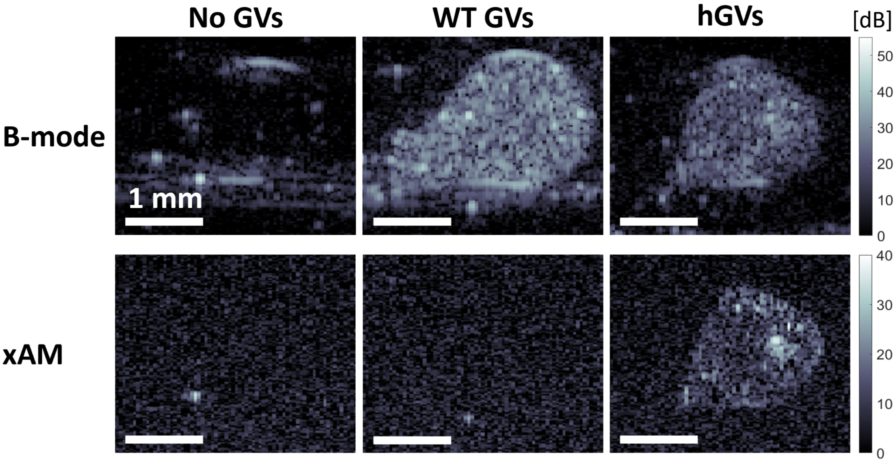

Figure 5.4: Ultrasound imaging of mesoscale alginate beads. Top row: linear B-mode ultrasound images of an empty bead and beads containing WT and hGVs, respectively. Bottom row: nonlinear xAM ultrasound images of the same three beads. WT GVs in alginate beads only appear in linear B-mode images, while hGVs appear in both linear B-mode and nonlinear xAM images. The interface of the bead without GVs faintly appears in linear B-mode images and does not appear in nonlinear xAM images.

5.3. DISCUSSION AND OUTLOOK

Our results provide a foundation for developing novel GV-based ultrasound contrast agents with enhanced echogenicity and potentially prolonged circulation times in the bloodstream. In vitro experiments confirmed our hypothesis that GVs can aggregate into periodic assemblies when suspended in an alginate solution above a certain threshold concentration, likely due to depletion interactions [232]. Moreover, we demonstrated that periodically aggregated hGVs yield significantly higher nonlinear ultrasound contrast enhancement compared to those aggregated randomly (20 dB vs. 14 dB). While this matches our initial hypothesis, based on effects seen in phononic meta-materials [224, 233], this study provides no verification that the same fundamental processes underlie our observations. Further study should focus on modelling of periodic aggregates, expanding on the work by Salahshoor *et al.* [24] which describes the dynamic response of GVs to acoustic pressure waves by including inter-GV interactions. Besides the acoustic properties of each aggregate, interactions between aggregates may also contribute to the unique be-

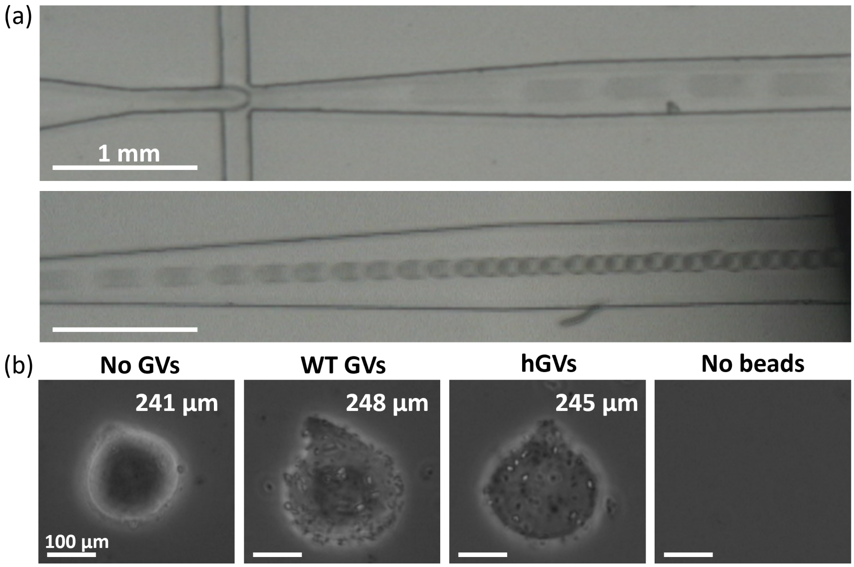

Figure 5.5: Microfluidic fabrication of microscale alginate beads. (a) Two single frame snapshots through an inverted light microscope showing droplet generation and flow at the flow focusing orifice (top) and the end of the microfluidic chip (bottom). (b) Phase contrast microscopy images of a bead without GVs, beads containing hGVs and WT GVs, respectively, and the empty background. WT and hGVs appear white in phase contrast microscopy, while the empty beads show no white contrast. Values at the top represent average bead size (N = 10), considering only the spherical part of teardrop-shaped beads.

haviours described in this work. A promising future direction would be to approach this problem using the theoretical framework developed for erythrocyte aggregates [223, 227].

Our findings reveal that nonlinear contrast enhancement initiates at an alginate concentration of 1.25 mg/ml for GVs at an optical density (OD) of 2, which corresponds to a GV concentration of 224 pM [160]. This concentration likely represents the threshold at which depletion interactions commence among GVs at this OD. Higher concentrations of alginate resulted in increased CNR until reaching a plateau at 1.75 mg/ml. Yao *et al.* [232] showed that GV assembly size correlates directly with depletant concentration. Consequently, the observed increase in contrast and subsequent plateau may relate to an increase in GV assembly size until a maximum size is achieved. Our results also indicate that periodically aggregated WT GVs in alginate exhibit significant nonlinear ultrasound contrast enhancement compared to controls at higher transmit voltages (+6 dB at 6 V).

Microscale beads were fabricated using a high-throughput, droplet-based microfluidic technique. Phase contrast microscopy revealed a distinct visual difference between beads containing either WT or hGVs, which exhibited a white contrast, compared to the empty alginate beads. The resulting alginate beads displayed a range of shapes, with an average size of approximately 245 µm. This observed size and shape contrast with the initial 125 µm spherical droplets formed inside the microfluidic chip, likely due to the gelation process. Off-chip gelation of alginate droplets in divalent ion baths creates polydisperse beads with varied shapes, influenced by multiple parameters [234].

Future work should explore alternative microfluidic chip designs and alginate gelation strategies to address these issues. On-chip alginate gelation methods have demonstrated the ability to produce beads with minimal size and shape variability [235]. This method would eliminate the need for a divalent ion bath, leading to a higher concentration of alginate beads in the collected solution. Additionally, smaller chip dimensions and solvent-extraction techniques have been shown to produce alginate beads measuring a few microns, comparable to conventional MB contrast agents [236].

5.4. CONCLUSION

In conclusion, our results illustrate the significant enhancement in nonlinear contrast produced by periodically aggregated GVs. Furthermore, we utilized a high-throughput microfluidic approach to fabricate sub-millimeter-scale GV-containing alginate beads rapidly. With further engineering of the microfluidic encapsulation strategy, we could potentially reduce the size of these innovative ultrasound contrast agents to match that of conventional MBs and mitigate the formation of unwanted air-filled cavities.

Once the size of the alginate beads is minimized to several microns and in vitro ultrasound experiments validate their enhanced echogenicity, in vivo studies should be conducted to confirm the prolonged circulation time of these alginate beads in the bloodstream.

In the future, these novel GV-based ultrasound contrast agents, featuring improved echogenicity, reduced random signal fluctuations, and extended circulation times, may become essential for non-invasive transcranial fUS imaging and other contrast-enhanced ultrasound imaging applications. For instance, the genetic and biochemical engineering of GV acoustic and targeting properties could facilitate highly specific molecular imaging of enzyme activity and detection of pH changes linked to inflammation.

5.5. MATERIALS AND METHODS

GAS VESICLE PREPARATION

Wild-type GVs (WT GVs) were isolated and purified from *Anabaena flos-aqueae* cyanobacteria following previously established protocols [160]. Nonlinear harmonic GVs (hGVs), which lack the structural reinforcement protein GvpC on their outer surface, were prepared by treating WT GVs with a 6 M urea solution, followed by two rounds of centrifugally assisted purification. The GV concentration was determined by measuring optical density (OD) at 500 nm using a spectrophotometer (Ocean Insight, Orlando, FL, USA). For both WT and hGVs, OD = 1 equates to a GV concentration of 114 pM in aqueous solution [160].

GAS VESICLE AGGREGATION

Periodic GV aggregation was facilitated through depletion interactions. A depletion force arises between impermeable particles suspended in a solution of depletants, solutes preferentially excluded from the immediate vicinity of the particles [232]. The periodic stacking of cylindrical GVs minimizes gaps, optimizing the available space for depletants and maximizing translational entropy. Sodium alginate (Mw = 216.12 g mol_{-1}, Sigma-Aldrich, St. Louis, MO, USA) served as the depletant, a biopolymer that forms biocompatible hydrogels through cross-linking with divalent cations like Ca_{2+}. We anticipated GV (OD = 2) aggregation at alginate concentrations equal to or exceeding 1.5 mg/ml, as GVs suspended in these solutions demonstrated increased buoyancy likely related to aggregation.

Nonperiodic GV aggregation was achieved by suspending GVs in a 100 mM solution of calcium chloride ($CaCl_2$, Sigma Aldrich, St. Louis, MO, USA) or through GV biotinylation followed by the addition of a 10,000 molar excess of streptavidin relative to GVs [4]. $CaCl_2$ and similar electrolytes induce GV aggregation by screening the net negative surface charge, facilitating attractive Van der Waals interactions. Biotinylation was performed using EZ-Link Sulfo-NHS-biotin (Thermofisher Scientific, Waltham, MA, USA) for four hours under gentle rotation, followed by two rounds of dialysis with HEPES buffer and two rounds of centrifugally assisted purification.

TRANSMISSION ELECTRON MICROSCOPY (TEM)

GV configurations were visualized via transmission electron microscopy (TEM) using a JEM-1400plus microscope (JEOL, Ltd., Tokyo, Japan) operating at 120 kV. Cu400 carbon support film TEM grids (Quantifoil Micro Tools GmbH, Großlöbichau, Germany) were glow discharged with a GloQube glow discharge system (Quorum Technologies, Lewes, UK) to render the grid surface hydrophilic. We added 3.6 µl of GV solution (OD = 1) with HEPES buffer (control), 2 mg/ml alginate, 100 mM $CaCl_2$, or biotinylated GVs (OD = 1) with or without a 10,000 molar excess of streptavidin to the TEM grid. After one minute, solutions were removed by wicking with filter paper. In all cases except alginate, a subsequent staining with 3 µl of 2% uranyl acetate for 30 seconds was performed. Alginate samples were not stained due to the uranyl ions causing alginate gelation. All TEM grids were allowed to air-dry before imaging.

TUNABLE RESISTIVE PULSE SENSING (TRPS)

TRPS measurments were performed using the Izon Exoid (Izon, Christchurch, New-zealand) nanopore device. Protocols can be found at the Izon academy website (https://academy.izon.com/) but will be described here in brief. GVs were aggregated using either 1.75 mg/ml alginate, or biotin-streptavadin. A 2000x molar excess streptavidin/biotin was used. Samples were diluted in buffer solution until a desirable count-rate was measured (500-1500 counts/min). Dilution buffers consisted of PBS or alginate (1.75 mg/ml) and PBS, depending on the sample being tested.

ULTRASOUND PHANTOM PREPARATION

Linear on nonlinear phantom imaging was performed in different setups and as such different phantom preparation was used.

NONLINEAR IMAGING PHANTOMS

Ultrasound imaging phantoms were prepared by melting a 2% agarose (Thermofisher Scientific, Waltham, MA, USA) solution in buffer, poured into a DNA gel holder. A custom 3D-printed male mold created cylindrical wells within the agarose measuring 5 mm in length and 2 mm in diameter. GV samples were mixed with 2% low melting temperature agarose for a final GV concentration of OD = 2 and incubated at 45 °C for one minute. Wells were filled with 20 µl of GV sample or 1% low melting temperature agarose for background noise measurements.

LINEAR IMAGING PHANTOMS

Ultrasound imaging phantoms were prepared by melting a 2% agarose (Thermofisher Scientific, Waltham, MA, USA) solution in buffer. GV samples were mixed with 2% low melting temperature agarose for a final GV concentration of OD = 2 and incubated at 45 °C for one minute. Three agarose layers were poured subsequently: a base layer of agarose, a middle layer of GVs + agarose, and a top layer of agarose.

ULTRASOUND IMAGING

Linear and nonlinear ultrasound imaging was performed in different setups:

NONLINEAR ULTASOUND IMAGING

Ultrasound imaging was conducted using a Verasonics Vantage 256-channel system with an L22-14V ultrasound probe (Verasonics Inc., Redmond, WA, USA). The probe is a linear array comprising 128 elements with a 0.10 mm pitch, a 1.5 mm elevation aperture, an 8 mm elevation focus, and a center frequency of 18.5 MHz (Vermon S.A., Tours, France). We employed a custom imaging sequence for both linear B-mode (brightness) ultrasound imaging and nonlinear cross-amplitude modulation (xAM) ultrasound imaging. Images were acquired with coherent compounding at angles of 10.5°, 16°, and 21°. Raw RF data collected from 10 acquisitions per field of view (FOV) was beamformed and summed offline.

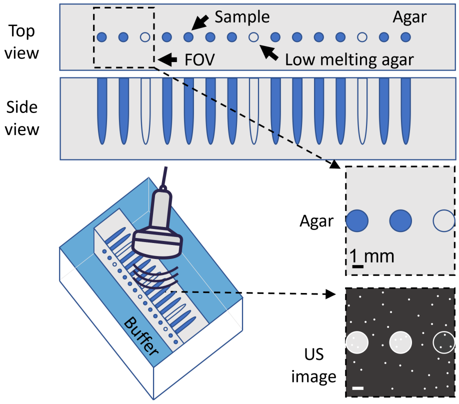

Figure 5.6: Phantom used for ultrasound characterization of GVs. The wells are created by inserting a mold in liquid agarose, which is removed once the agarose has solidified. Wells can then be filled with either GV samples mixed with agarose (blue) or just agarose (gray), as displayed here, such that in every field-of-view (FOV) there is always at least 1 agarose well for background noise measurements. Once solidified, the phantom can then be imaged on its side to obtain ultrasound images of well cross sections.

LINEAR ULTRASOUND IMAGING

Experiments were conducted with two seperate flat transducers with center frequencies of 10 MHz, and 35 MHz. The transducer was used in emission/reception and the transducer focus was positioned at the interface of the phantom agar slab. Two phantoms were used per sample,at two different imaging depths (4 mm and 8 mm). The pulse-echo acquisition system was composed of an Olympus model 5072 PR (5073PR for 55MHz transducer) pulser-receiver and a high-speed acquisition card (Gagescope). The raw RF data was digitizied at a sampling frequency of 250MHz. At least four positions were scanned per sample, B-mode images were constructed from the acquired RF echoes (180 RF lines per position). The signals were gated with a rectangular window around the focal zone The power spectra of the four echoes were averaged. This procedure was repeated for each transducer for each sample.

ALGINATE BEAD PRODUCTION AND CHARACTERIZATION

For mesoscale bead production, WT and hGVs (OD = 2) or HEPES buffer (control) were suspended in a 1% alginate solution (10 mg/ml). The solutions were gradually ejected from a syringe with a G23 needle into a bath of 0.5 M $CaCl_2$ from a height of 5 cm. The acoustic properties of the mesoscale beads were assessed using linear B-mode and non-linear xAM ultrasound imaging after trapping them in a 2% agarose phantom. The microscale beads were examined acoustically and optically using an IX71 inverted light microscope (Olympus Corp., Tokyo, Japan) equipped with a 20x phase contrast objective and DCC1645C digital camera (Thorlabs Inc., Newton, NJ, USA). Phase contrast microscopy was selected since GVs generate positive phase contrast [237, 238]. This was confirmed by comparing OD = 2 WT GVs pre- and post-collapse. The average bead diameters for droplet-shaped meso- and microscale beads were estimated by considering only the spherical portions of each bead.

5.6. SUPPLEMENTARY SECTION

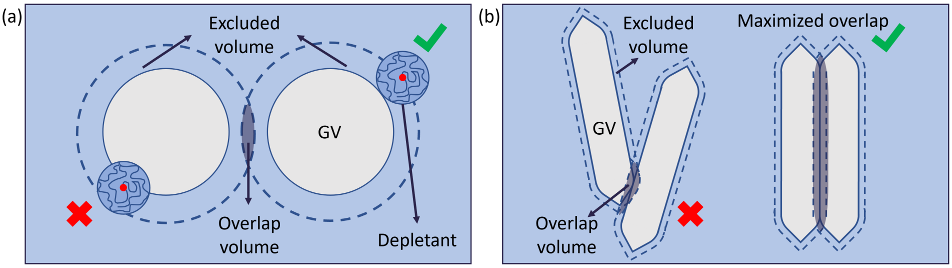

Figure S5.1: Schematic representation of depletion interactions on GVs. (a) Depletants such as alginate are preferentially excluded from the vicinity (i.e. the excluded volume) of impermeable GVs. (b) To minimize the gap between GVs and thus maximize the free space for depletants, maximal overlap of the excluded volume is achieved through periodic, side-by-side stacking.

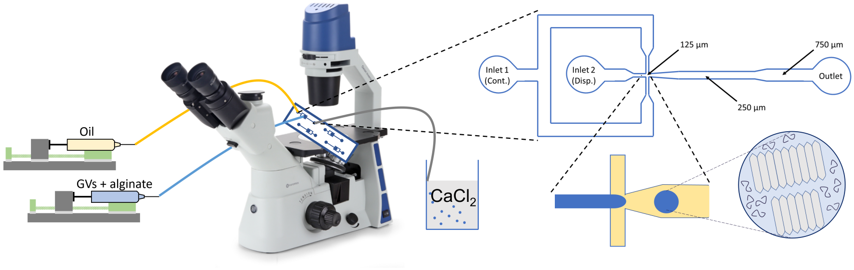

Figure S5.2: Sketch of the microfluidic bead fabrication setup and the flow focusing chip design used for droplet generation. The continuous phase (oil and surfactant) is supplied to inlet 1 and the dispersed phase (alginate with or without WT or hGVs) is supplied to inlet 2. The flowrates are controlled using syringe pumps. Droplets are collected from the outlet in a calcium bath.

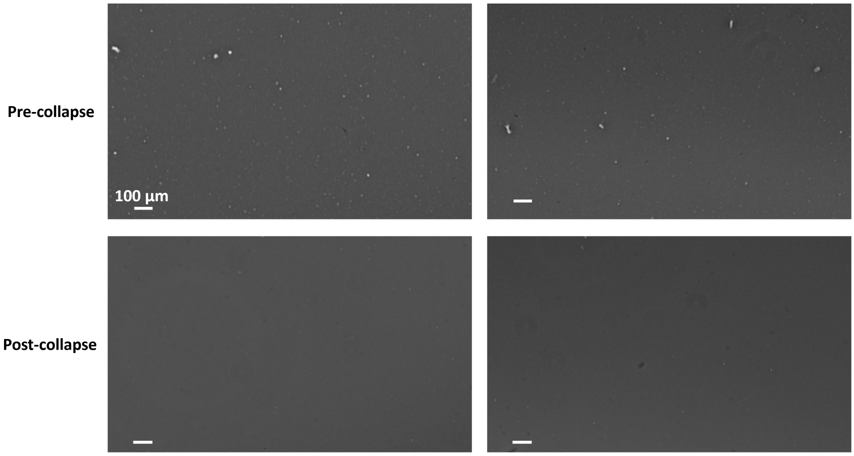

Figure S5.3: Phase contrast microscopy images of WT GVs pre- and post collapse. Using phase contrast microscopy, OD = 2 WT GVs were compared before and after collapse. GV collapse was induced by applying 10 bar hydrostatic pressure to the solution. Pre-collapse, white contrast is observed in the phase contrast microscopy images, whereas the white contrast is absent in the post-collapse images.

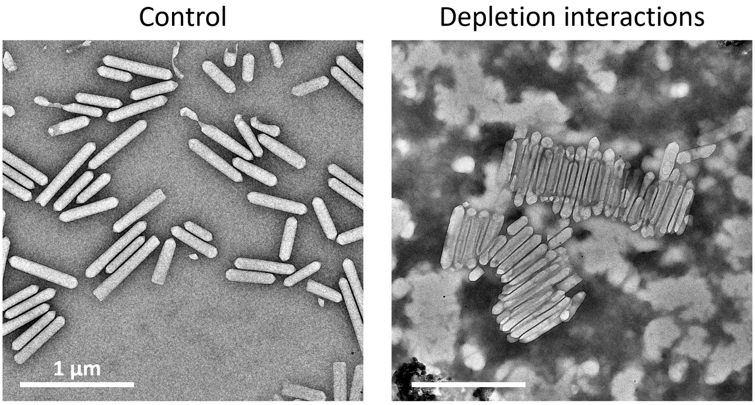

Figure S5.4: Alginate-induced periodic WT GV aggregation. TEM images of WT GVs (OD = 1) suspended in 1 mg/ml alginate show periodic GV aggregation when compared to the control, similar to hGVs (Figure 5.1).

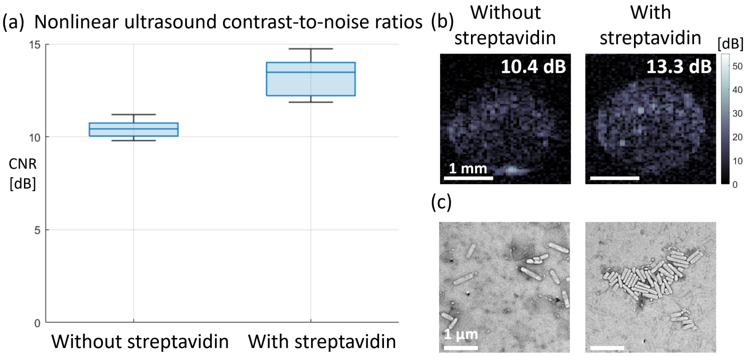

Figure S5.5: Nonlinear ultrasound contrast for biotinylated GVs with and without streptavidin. (a) Box plots of the CNR values for biotinylated hGVs (OD = 2) with and without a 10.000 molar excess of streptavidin. Lower and upper box boundaries represent the 25th and 75th percentiles, while the middle line represents the median. Lower and upper error lines represent the 10th and 90th percentiles. (b) Representative xAM ultrasound images and (c) TEM images of the samples described above. Streptavidin induces aggregation of biotinylated GVs, which enhances nonlinear ultrasound contrast by 3 dB compared to unaggregated biotinylated hGVs. Values in the top right corner of each ultrasound image indicate the average contrast per sample. Scale bars in ultrasound images represent 1 mm, while in TEM images they represent 1 µm. In all cases, N = 8.

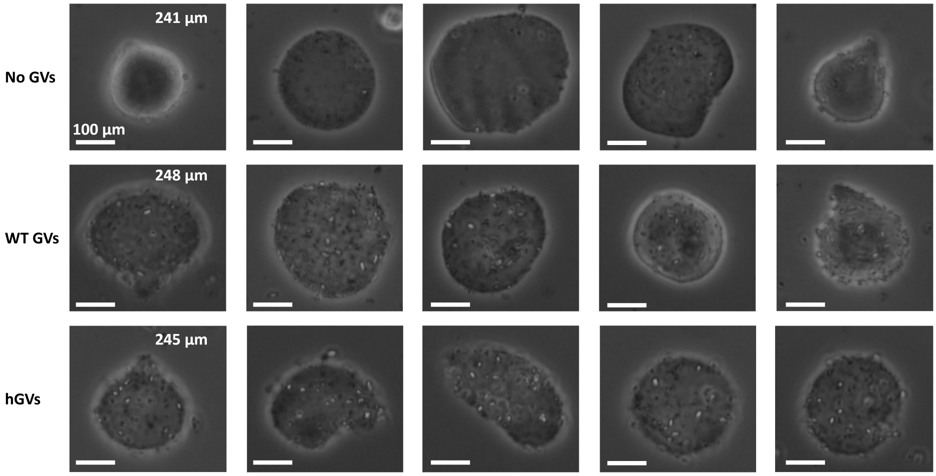

Figure S5.6: Phase contrast microscopy images of microscopic beads. Top row: beads without GVs. Middle row: beads with WT GVs (OD = 2). Bottom row: beads with hGVs (OD = 2). Beads containing GVs showed the presence of GVs as white contrast, whereas the beads without GVs appeared empty. The beads had various shapes and sizes. Values in the top right of the first column indicate the average size of N = 10 beads.

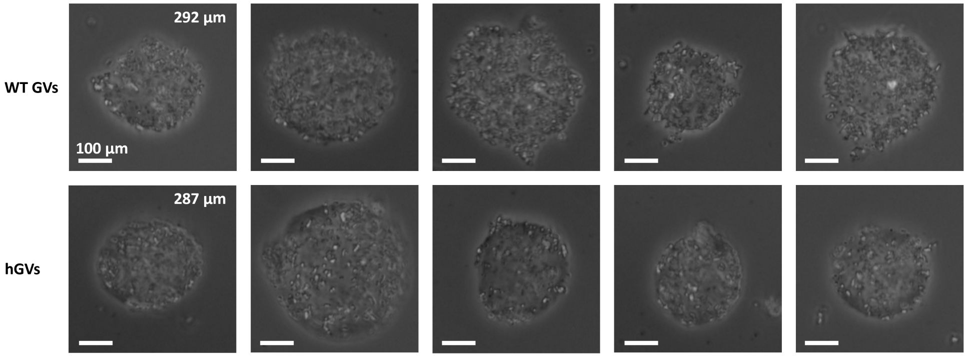

Figure S5.7: Phase contrast microscopy images of microscopic beads containing OD 8 WT and hGVs. Top row: beads with WT GVs. Bottom row: beads with hGVs. Beads containing a higher OD GVs appear more crowded, but were also larger than beads with OD = 2 GVs. Values in the top right of the first column indicate the average size of N = 10 beads.

6

DISCUSSION AND OUTLOOK

SUMMARY OF RESULTS

The goal of this thesis was to develop the first ultrasound biosensor for pH based on gas vesicles (GVs). This work builds upon the pioneering proof-of-concept by Lakshmanan et al. [11], who demonstrated the feasibility of engineering GV-based ultrasound biosensors. By advancing to second-generation biosensors, this thesis focuses on clinically and scientifically relevant biomarkers.

chapter 3 establishes the structural foundation of GVs using cryo-electron microscopy (cryo-EM) to develop a high-resolution atomic model. This work primarily examines the folding and conformation of the GvpA shell protein while conducting a conservancy screening of GvpC sequences. The proposed folding and binding mechanism for GvpC provides crucial insights into how it maintains GV integrity. These findings serve as a critical foundation for biosensor engineering by elucidating the molecular architecture of GVs and enabling targeted modifications to enhance their acoustic properties.

Building on this foundation, chapter 4 introduces pHonon, the first GV-based pH biosensor for ultrasound imaging. The structural insights from chapter 3 informed the identification of specific sites on GvpC for targeted mutations, where histidine substitutions conferred pH sensitivity. These mutations leveraged the pH-dependent ionization properties of histidine residues while preserving GvpC structural integrity. Validation experiments demonstrated pHonon's ability to visualize pH dynamics *in vitro* and in vivo, offering a novel and noninvasive approach to monitor intracellular and extracellular acidification. This innovation has potential applications in both clinical diagnostics and basic research, although further optimization is needed to improve sensitivity and applicability.

chapter 5 explores an alternative approach to enhancing GV performance through physical aggregation rather than genetic modifications. Using biotin-streptavidin interactions and depletion interactions to induce GV clustering, the study showed that aggregated GVs exhibited enhanced ultrasound contrast, with significant boosts in linear and nonlinear signals. Remarkably, even wild-type GVs, typically too stiff to deform under insonification, demonstrated nonlinear scattering when aggregated. This method offers a versatile, complementary strategy for improving GV performance in high-contrast imaging applications.

Together, these chapters present a comprehensive exploration of GVs' structural and functional capabilities. They establish GVs as powerful tools for molecular and cellular ultrasound imaging while opening new avenues for biosensor development and engineering. From structural characterization to biosensor innovation and performance enhancement, this work marks a significant advancement in the field of biomolecular ultrasound imaging.

FUTURE WORK AND RECOMMENDATIONS

While this thesis demonstrates the potential of pHonon as a pH biosensor, further refinement is required to address specific challenges and broaden its applicability.

CHALLENGES FOR ENGINEERING GAS VESICLES AS MOLECULAR CONTRAST AGENTS

Gas vesicles (GVs) have been explored for two main applications in ultrasound imaging: as intracellular reporters and as injectable contrast agents. Each of these applications faces specific engineering challenges.

CHALLENGES FOR INTRACELLULAR REPORTERS

The primary hurdle for using GVs as intracellular reporters in mammalian cells, particularly in vivo, is the metabolic burden associated with their heterologous expression. GVs are massive protein complexes, with a molecular weight roughly 100 times greater than Titin, the largest known human protein [239]. Expressing these large structures places a significant metabolic strain on sensitive mammalian cell lines, which can compromise cell viability and alter normal cellular behavior.

This metabolic load makes it difficult to engineer stable, GV-expressing cell lines for research. While this may be less critical for applications like solid tumor imaging, where imaging occurs over several hours and tumor dynamics are slow, it becomes a major limitation for advanced applications. For instance, in sensitive dynamic processes like calcium sensing in neurons, the metabolic stress can significantly distort the very cellular activities being measured.

Additionally, the large genetic constructs required for GV expression are often unwieldy and unstable. Although efforts have been made to create minimal gene clusters and improve genetic constructs [240, 241], a significant knowledge gap remains. The function of many genes within the GV cluster and the biomechanics of the vesicles themselves are not yet fully understood. This is not entirely surprising, given the diversity of known GV genes and the complexity of their interactions [17], but it represents a key area for future research.

CHALLENGES FOR INJECTABLE CONTRAST AGENTS

When used as injectables, GVs face a different set of challenges, particularly related to the immune response. GVs are highly immunogenic and trigger the production of a wide range of antibodies [6]. Although small-animal studies have not yet reported adverse effects, comprehensive health and safety studies have not been performed, representing a critical area of concern. This immunogenicity also leads to shortened circulation times, though GVs still circulate for longer than traditional microbubbles. This limits their potential for applications that require sustained vascular reporting.

APPLICATIONS, PATHOLOGIES, AND FUTURE DIRECTIONS FOR PHONON

Disruption of pH homeostasis is a key biomarker in many pathologies, but its manifestations vary in location and severity, making some conditions more suited to GV-based ultrasound imaging than others. One promising application is revisiting ischemic memory imaging [34, 242], a technique reliant on the inflammatory response following ischemic reperfusion. In brief, the method relies on functionalized microbubbles with surface ligands specifically targeted at inflammatory surface proteins on endothelial cells. Image acquisition has three parts: An image is acquired after thorough perfusion, followed by destruction of the microbubble population within the imaging window, and concluded with a second image shortly after reperfusion. The assumption is that the first image contains both bound and unbound microbubbles, whereas the second image will only have unbound microbubbles, and the difference between these images shows a map of only the bound microbubbles. This method is limited by low reproducibility, particularly in low-perfusion organs like the brain, and is restricted to imaging vascular inflammation. pHonon could overcome these limitations by being internalized by endocytic cells at the injury sites, enabling tracking of immune cells as they report endosomal acidification. This mitigates the need for a destructive pulse, allowing longitudinal observation of inflammation, as well as tracking of immune cells as they migrate throughout tissue.

Another exciting application is the imaging of solid tumors. Tumors exhibit the Warburg effect, where cancer cells produce excess lactic acid, leading to extracellular acidosis [243]. This local acidosis is associated with a poor prognosis, increased metastases, and resistance to therapy [244]. Ultrasound's high resolution and accessibility make it suitable for tumor imaging. Additionally, it has been shown that GVs readily extravasate in the characteristically leaky vasculature of tumor tissue [245]. However, the current sensitivity of pHonon is insufficient to resolve the subtle pH changes in acidotic tumor environments (typically pH 6.4–7.2), necessitating enhancements in sensitivity. Additionally, and perhaps more challenging, this necessitates re-engineering the linear to nonlinear transition point of pHonon.

Neurodegenerative illnesses, like Alzheimer's disease (AD), represent another potential application. AD often involves defects in the endo-lysosomal system, which is responsible for removing excess proteins and deposits in the brain [246]. Deficiencies in the V-ATPase complex, which maintains low endo-lysosomal pH, have been implicated in AD as the cause for the build-up of amyloid plaques [247, 248]. pHonon could serve as a valuable tool to investigate these defects, shedding light on the disease's pathophysiology.

Despite these promising applications, several challenges remain. First, pHonon's sensitivity must be increased. While the biosensor currently discriminates between pH 5, 6, and 7, tumor environments require significantly higher sensitivity to resolve pH variations accurately. Second, the kinetics of pHonon are relatively slow, operating on the scale of minutes. While this timescale aligns with endo-lysosomal acidification, it can be a confounding factor in dynamic in vivo pH measurements. A potential solution involves high-throughput screening of closely related mutants to refine pHonon's design.

Finally, developing a specific imaging mode tailored to pHonon remains a critical task. The proposed ratiometric method in chapter 4 is limited in vivo, as tissue echogenicity variations can distort B-mode contrast normalization. A dedicated imaging mode for pHonon would need to account for spatial and temporal signal changes, stabilize motion, and correct for concentration-based variations.

In summary, pHonon holds immense promise for various applications, from inflammation imaging to tumor and Alzheimer's research. Addressing these design limitations and developing tailored imaging protocols will unlock its full potential and significantly advance its clinical and scientific utility.

GV AGGREGATION, MINIATURIZATION, AND AGGREGATION-BASED BIOSENSORS

While GVs offer many benefits over microbubble contrast agents, they suffer from a significantly reduced echogenicity due to their small size. While this problem is partly mitigated during high-concentration intravenous administration, it becomes more problematic in low-concentration applications, such as ULM or functional imaging of small vessels. In chapter 5, we showed that GV aggregates could be suitable to address this problem, due to their higher echogenicity. By tuning aggregate sizes, one would theoretically be able to obtain a balance between access to small vasculature and contrast agent signal intensity. The primary challenge then lies in how to stabilize such contrast agents, particularly those forming through depletion interactions. We proposed using microfluidic droplet-forming devices to encapsulate the aggregates in a hydrogel (e.g., alginate), an approach derived from certain delayed-delivery pharmaceuticals [228]. While we were able to prove the concept with large droplet sizes, one of the biggest challenges lies in miniaturization of the technology.

Microfluidic chips have been shown to be capable of making alginate beads down to a diameter of 5 μm, on a similar scale to microbubbles [236, 249, 250]. However, to truly reap the benefits of the GV aggregates, droplet diameters would have to be reduced to around 1 μm. Sub-micron Alginate bead generation methods exist that use oil in water techniques, such as electrospraying [251] or ultrasonic atomization [252]. However, it is not known whether the shear forces inside a microfluidic device or spray system exceed the stability of the GV shell, or whether the acoustic properties of the aggregate are affected by the surrounding hydrogel.

While increasing brightness at the cost of particle size is very interesting for applications in ULM or functional imaging, the increase in nonlinear ultrasound contrast arising from aggregation in fundamentally linearly scattering particles (wtGVs) found in chapter 5 has some interesting implications for the design of GV biosensors. While most of the GV engineering work has focused on engineering the binding interaction between GvpC and GvpA, primarily through edits in GvpC, we could alternatively look at ways to induce aggregation. By engineering the C-terminal tail of GvpA that faces into the cytosol, we could theoretically promote aggregation in the presence of certain biomarkers. Alternatively, engineering of, or appending to, the C- or N-terminal tail of GvpC could yield the same result.

The main challenge resides in engineering a way to mimic the organized periodic aggregation observed from depletion interactions that gives rise to the clear increase in nonlinear ultrasound contrast. To achieve this, it is key to avoid aggregation interactions on the tips and conical ends of GVs, a challenging proposal as the conical ends are thought to be structurally identical to the cylindrical wall [12, 17, 169, 171, 253].

Finally, it should be remarked that aggregation-based GV biosensors would have to overcome another recently discovered challenge: unwanted in vivo aggregation. Ling *et al.* [6] found that both red blood cells (RBCs) and other components in serum cause GV aggregation in vivo. While they also demonstrate that a methoxypoly(ethylene glycol) (mPEG) surface coating can successfully prevent significant aggregation or RBC adsorption, combining this with biosensing aggregation strategies will be problematic.

CONCLUSIONS

The collective advancements reported in this thesis underscore the transformative potential of GVs as biomolecular tools for molecular ultrasound imaging. The integration of structural insights, functional engineering, and innovative aggregation techniques provides a versatile platform for addressing longstanding challenges in biomolecular ultrasound imaging.

Looking forward, expanding the range of GV-based biosensors to target additional biomarkers, such as oxidative stress, enzymes, or metabolites, could significantly broaden their applicability. Moreover, combining GV technology with complementary imaging modalities, such as photoacoustics, MRI, or PET, may unlock new possibilities for multimodal imaging. Addressing challenges related to biosensor sensitivity, aggregation control, and in vivo stability will be critical for translating these innovations into clinical and industrial settings.

This thesis introduces novel tools that advance the emerging field of biomolecular ultrasound imaging, expanding the capabilities of ultrasound at the nanoscale. As part of the first generation of gas vesicle-based nanoscale ultrasound biosensors, these innovations overcome traditional resolution constraints, enabling dynamic and longitudinal visualization of cellular—and even molecular—processes deep within opaque specimens. By harnessing the unique properties of these biosensors, researchers can now explore biological systems with unprecedented depth and clarity. Propelled by this first wave of dynamic gas vesicle biosensors, the field is poised for remarkable breakthroughs, unlocking new frontiers in imaging and revolutionizing our ability to study life at the molecular level.

BIBLIOGRAPHY

1. Mace, E. *et al.* Functional ultrasound imaging of the brain. *Nature Methods* **8,** 662–664. ISSN: 1548-7105 (Aug. 2011).
2. Renaudin, N. *et al.* Functional ultrasound localization microscopy reveals brain-wide neurovascular activity on a microscopic scale. *Nature methods* **19,** 1004–1012. ISSN: 1548-7091 (2022).
3. Heiles, B., Terwiel, D. & Maresca, D. The advent of biomolecular ultrasound imaging. *Neuroscience* **474,** 122–133. ISSN: 0306-4522 (Mar. 2021).
4. Shapiro, M. G. *et al.* Biogenic gas nanostructures as ultrasonic molecular reporters. *Nature Nanotechnology* **9,** 311–316. ISSN: 1748-3395 (Mar. 2014).
5. Farhadi, A. *Acoustic Reporter Genes for Noninvasive Imaging of Cellular Function* English. PhD thesis (United States – California, 2020), 179. ISBN: 9798379857059.
6. Ling, B. *et al.* Gas Vesicle–Blood Interactions Enhance Ultrasound Imaging Contrast. *Nano Letters* **23,** 10748–10757. ISSN: 1530-6984 (Dec. 2023).
7. Wang, G. *et al.* Surface-modified GVs as nanosized contrast agents for molecular ultrasound imaging of tumor. *Biomaterials* **236,** 119803. ISSN: 18785905 (Apr. 2020).
8. Hurt, R. C. *et al.* Genomically mined acoustic reporter genes for real-time in vivo monitoring of tumors and tumor-homing bacteria. *Nature Biotechnology 2023 41:7* **41,** 919–931. ISSN: 1546-1696 (Jan. 2023).
9. Heiles, B. *et al.* Nonlinear sound-sheet microscopy: imaging opaque organs at the capillary and cellular scale. *bioRxiv,* 2024.07.31.605825 (Jan. 2024).
10. Bourdeau, R. W. *et al.* Acoustic reporter genes for noninvasive imaging of microorganisms in mammalian hosts. *Nature* **553,** 86–90. ISSN: 14764687 (Jan. 2018).
11. Lakshmanan, A. *et al.* Acoustic Biosensors for Ultrasound Imaging of Enzyme Activity. *Nature Chemical Biology* **16,** 988–996. ISSN: 15524469 (Sept. 2020).
12. Huber, S. T. *et al.* Cryo-EM structure of gas vesicles for buoyancy-controlled motility. *Cell* **186,** 975–986. ISSN: 10974172 (2023).
13. Zhu, J., He, X. & Chen, Z. Perspective: Current challenges and solutions of Doppler optical coherence tomography and angiography for neuroimaging. *APL Photonics* **3,** 120902. ISSN: 2378-0967 (Dec. 2018).
14. Lee, H. *et al. Microbubbles used for contrast enhanced ultrasound and theragnosis: a review of principles to applications* May 2017.
15. Wang, S., Hossack, J. A. & Klibanov, A. L. Targeting of microbubbles: contrast agents for ultrasound molecular imaging. *Journal of Drug Targeting* **26,** 420–434. ISSN: 1061-186X (May 2018).

16. Walsby, A. E. & Hayes, P. K. The minor cyanobacterial gas vesicle protein, GVPc, is attached to the outer surface of the gas vesicle. *Microbiology* **134,** 2647–2657. ISSN: 1350-0872 (1988).
17. Iburg, M. *et al.* Elucidating the assembly of gas vesicles by systematic protein-protein interaction analysis. *The EMBO Journal* **43,** 4156–4172. ISSN: 0261-4189 (Oct. 2024).
18. Ling, B. *et al.* Truly Tiny Acoustic Biomolecules for Ultrasound Imaging and Therapy. *Advanced Materials* **36,** 2307106. ISSN: 0935-9648 (July 2024).
19. Lakshmanan, A. *et al.* Molecular Engineering of Acoustic Protein Nanostructures. *ACS Nano* **10,** 7314–7322. ISSN: 1936-086X (Aug. 2016).
20. Maresca, D. *et al.* Nonlinear X-Wave Ultrasound Imaging of Acoustic Biomolecules. *Physical Review X* **8,** 041002. ISSN: 21603308 (Oct. 2018).
21. Rabut, C. *et al.* Ultrafast amplitude modulation for molecular and hemodynamic ultrasound imaging. *Applied Physics Letters* **118,** 244102. ISSN: 0003-6951 (June 2021).
22. Nayak, R. *et al.* Harmonic imaging for nonlinear detection of acoustic biomolecules. *bioRxiv,* 2024.06.18.599141 (Jan. 2024).
23. Cherin, E. *et al.* Acoustic Behavior of Halobacterium salinarum Gas Vesicles in the High-Frequency Range: Experiments and Modeling. *Ultrasound in Medicine & Biology* **43,** 1016–1030. ISSN: 0301-5629 (2017).
24. Salahshoor, H. *et al.* Geometric effects in gas vesicle buckling under ultrasound. *Biophysical Journal* **121,** 4221–4228. ISSN: 0006-3495 (Nov. 2022).
25. Renaud, G. *et al.* Increasing specificity of contrast-enhanced ultrasound imaging using the interaction of quasi counter-propagating wavefronts: A proof of concept. *IEEE Transactions on Ultrasonics, Ferroelectrics, and Frequency Control* **62,** 1768–1778. ISSN: 08853010 (Oct. 2015).
26. Sawyer, D. P. *et al.* Ultrasensitive ultrasound imaging of gene expression with signal unmixing. *Nature Methods* **18,** 945–952. ISSN: 1548-7091 (2021).
27. Nyström, N. N. *et al.* Multiplexed Ultrasound Imaging of Gene Expression. *bioRxiv,* 2024.10.30.621148 (Jan. 2024).
28. Buss, M. T. *et al.* Probiotic acoustic biosensors for noninvasive imaging of gut inflammation. *bioRxiv,* 2024.09.23.614598 (Jan. 2024).
29. Shivaei, S. *et al.* Non-invasive imaging of cell-based therapies using acoustic reporter genes. *bioRxiv,* 2024.11.01.621111 (Jan. 2024).
30. Jin, Z. *et al.* Ultrasonic reporters of calcium for deep tissue imaging of cellular signals. *bioRxiv,* 2023.11.09.566364 (Jan. 2023).
31. Warburg, O., Wind, F. & Negelein, E. The metabolism of tumors in the body. *Journal of General Physiology* **8,** 519–530. ISSN: 15407748 (Mar. 1927).
32. Potter, M., Newport, E. & Morten, K. J. The Warburg effect: 80 years on. *Biochemical Society Transactions* **44,** 1499. ISSN: 14708752 (Oct. 2016).
33. Steinback, C. D. & Poulin, M. J. Cardiovascular and cerebrovascular responses to acute isocapnic and poikilocapnic hypoxia in humans. *Journal of Applied Physiology* **104,** 482–489. ISSN: 87507587 (Feb. 2008).

34. Villanueva, F. S. *et al.* Myocardial ischemic memory imaging with molecular echocardiography. *Circulation* **115,** 345–352. ISSN: 00097322 (Jan. 2007).

35. Miesenbock, G., De Angelis, D. A. & Rothman, J. E. Visualizing secretion and synaptic transmission with pH-sensitive green fluorescent proteins. *Nature* **394,** 192–195. ISSN: 00280836 (1998).

36. Mahon, M. J. pHluorin2: an enhanced, ratiometric, pH-sensitive green florescent protein. *Advances in Bioscience and Biotechnology* **02,** 132–137. ISSN: 2156-8456 (2011).

37. Zhao, R. *et al.* Phosphatidylserine-microbubble targeting-activated microglia/macrophage in inflammation combined with ultrasound for breaking through the blood–brain barrier. *Journal of Neuroinflammation* **15,** 334. ISSN: 1742-2094 (Dec. 2018).

38. Li, X. *et al.* Recent development of pH-responsive theranostic nanoplatforms for magnetic resonance imaging-guided cancer therapy. *Exploration* **3,** 20220002 (2023).

39. Yang, Z. *et al.* A pH-responsive photoacoustic imaging probe for tumor pH imaging in vivo based on polyaniline–bovine serum albumin. *Nanomedicine: Nanotechnology, Biology and Medicine* **33,** 102356. ISSN: 1549-9634 (2021).

40. Rabut, C. *et al.* Ultrasound Technologies for Imaging and Modulating Neural Activity. *Neuron* **108,** 93–110. ISSN: 0896-6273 (2020).

41. Aaslid, R., Markwalder, T.-M. & Nornes, H. Noninvasive transcranial Doppler ultrasound recording of flow velocity in basal cerebral arteries. *Journal of Neurosurgery* **57,** 769–774. ISSN: 0022-3085 (Dec. 1982).

42. Rabut, C. *et al.* 4D functional ultrasound imaging of whole-brain activity in rodents. *Nature Methods* **16,** 994–997. ISSN: 15487105 (2019).

43. Deffieux, T. *et al.* Functional ultrasound neuroimaging: a review of the preclinical and clinical state of the art. *Current Opinion in Neurobiology* **50,** 128–135. ISSN: 0959-4388 (2018).

44. Demene, C. *et al.* Functional ultrasound imaging of brain activity in human newborns. *Science Translational Medicine* **9.** ISSN: 1946-6242 (2017).

45. Imbault, M. *et al.* Intraoperative Functional Ultrasound Imaging of Human Brain Activity. *Scientific Reports* **7.** ISSN: 2045-2322 (Aug. 2017).

46. Soloukey, S. *et al.* Functional Ultrasound (fUS) During Awake Brain Surgery: The Clinical Potential of Intra-Operative Functional and Vascular Brain Mapping. *Frontiers in Neuroscience* **13.** ISSN: 1662-453X (2020).

47. Heiles, B. *et al.* Ultrafast 3D Ultrasound Localization Microscopy Using a 32 $\times$ 32 Matrix Array. *IEEE Transactions on Medical Imaging* **38,** 2005–2015. ISSN: 1558-254X (Sept. 2019).

48. Bonnefous, O. & Pesqué, P. Time Domain Formulation of Pulse-Doppler Ultrasound and Blood Velocity Estimation by Cross Correlation. *Ultrasonic Imaging* **8,** 73–85. ISSN: 1096-0910 (Apr. 1986).

49. Bercoff, J. *et al.* Ultrafast compound doppler imaging: providing full blood flow characterization. *IEEE Transactions on Ultrasonics, Ferroelectrics and Frequency Control* **58,** 134–147. ISSN: 0885-3010 (2011).

50. Kaul, S. Myocardial Contrast Echocardiography: A 25-Year Retrospective. *Circulation* **118,** 291–308. ISSN: 1524-4539 (2008).

51. Ferrara, K., Pollard, R. & Borden, M. *Ultrasound microbubble contrast agents: Fundamentals and application to gene and drug delivery* Aug. 2007.

52. Tsien, R. Y. The green fluorescent protein. *Annual Review of Biochemistry* **67,** 509–544. ISSN: 1545-4509 (1998).

53. Maresca, D. *et al.* Biomolecular ultrasound and sonogenetics. *Annual Review of Chemical and Biomolecular Engineering* **9,** 229–252. ISSN: 19475438 (2018).

54. Yu, F. T. *et al.* A local increase in red blood cell aggregation can trigger deep vein thrombosis: Evidence based on quantitative cellular ultrasound imaging. *Journal of Thrombosis and Haemostasis* **9,** 481–488. ISSN: 15387933 (Mar. 2011).

55. Farhadi, A. *et al.* Ultrasound imaging of gene expression in mammalian cells. *Science* **365,** 1469–1475. ISSN: 10959203 (Sept. 2019).

56. Wang, L. V. & Yao, J. A practical guide to photoacoustic tomography in the life sciences. *Nature Methods* **13,** 627–638. ISSN: 1548-7105 (2016).

57. Ivanov, K. P., Kalinina, M. K. & Levkovich, Y. Blood flow velocity in capillaries of brain and muscles and its physiological significance. *Microvascular Research* **22,** 143–155. ISSN: 0026-2862 (Sept. 1981).

58. Keller, D., Erö, C. & Markram, H. Cell Densities in the Mouse Brain: A Systematic Review. *Frontiers in Neuroanatomy* **12.** ISSN: 1662-5129 (2018).

59. Mcgarry, M. Mouse hematology. *Cold Spring Harbor Protocols* **2010,** pdb.rec11234. ISSN: 1559-6095 (2010).

60. Kirst, C. *et al.* Mapping the Fine-Scale Organization and Plasticity of the Brain Vasculature. *Cell* **180,** 780–795. ISSN: 0092-8674 (2020).

61. Van Raaij, M. E. *et al.* Quantification of blood flow and volume in arterioles and venules of the rat cerebral cortex using functional micro-ultrasound. *NeuroImage* **63,** 1030–1037. ISSN: 1053-8119 (Nov. 2012).

62. Errico, C. *et al.* Transcranial functional ultrasound imaging of the brain using microbubble-enhanced ultrasensitive Doppler. *NeuroImage* **124,** 752–761. ISSN: 1053-8119 (2016).

63. Pellow, C. *et al.* High frequency ultrasound nonlinear scattering from porphyrin nanobubbles. *Ultrasonics* **110,** 106245. ISSN: 0041-624X (2021).

64. Maresca, D. *et al.* Acoustic biomolecules enhance hemodynamic functional ultrasound imaging of neural activity. *NeuroImage* **209,** 116467. ISSN: 1053-8119 (Apr. 2020).

65. Tremblay-Darveau, C. *et al.* Visualizing the Tumor Microvasculature With a Nonlinear Plane-Wave Doppler Imaging Scheme Based on Amplitude Modulation. *IEEE Transactions on Medical Imaging* **35,** 699–709. ISSN: 1558-254X (2016).

66. Tanter, M. & Fink, M. Ultrafast imaging in biomedical ultrasound. *IEEE Transactions on Ultrasonics, Ferroelectrics, and Frequency Control* **61,** 102–119. ISSN: 0885-3010 (2014).

67. Bruneel, C. *et al.* Ultrafast echotomographic system using optical processing of ultrasonic signals. *Applied Physics Letters* **30,** 371–373. ISSN: 1077-3118 (Apr. 1977).

68. Montaldo, G. *et al.* Coherent plane-wave compounding for very high frame rate ultrasonography and transient elastography. *IEEE Transactions on Ultrasonics, Ferroelectrics and Frequency Control* **56,** 489–506. ISSN: 0885-3010 (2009).

69. Demene, C. *et al.* Spatiotemporal Clutter Filtering of Ultrafast Ultrasound Data Highly Increases Doppler and fUltrasound Sensitivity. *IEEE Transactions on Medical Imaging* **34,** 2271–2285. ISSN: 1558-254X (Nov. 2015).

70. Maresca, D., Tanter, M. & Pernot, M. *Ultrasound microangiography of the metacarophalangeal joint using ultrafast Doppler* in *2014 IEEE International Ultrasonics Symposium* (IEEE, Sept. 2014).

71. Ekroll, I. K. *et al.* Coherent compounding in doppler imaging. *IEEE Transactions on Ultrasonics, Ferroelectrics, and Frequency Control* **62,** 1634–1643. ISSN: 0885-3010 (Sept. 2015).

72. Demené, C. *et al.* Multi-parametric functional ultrasound imaging of cerebral hemodynamics in a cardiopulmonary resuscitation model. *Scientific Reports* **8.** ISSN: 2045-2322 (Nov. 2018).

73. Hingot, V. *et al.* Early Ultrafast Ultrasound Imaging of Cerebral Perfusion correlates with Ischemic Stroke outcomes and responses to treatment in Mice. *Theranostics* **10,** 7480–7491. ISSN: 1838-7640 (2020).

74. Brunner, C. *et al.* A Platform for Brain-wide Volumetric Functional Ultrasound Imaging and Analysis of Circuit Dynamics in Awake Mice. *Neuron* **108,** 861–875. ISSN: 0896-6273 (Dec. 2020).

75. Demené, C. *et al.* Ultrafast Doppler Reveals the Mapping of Cerebral Vascular Resistivity in Neonates. *Journal of Cerebral Blood Flow & Metabolism* **34,** 1009–1017. ISSN: 1559-7016 (2014).

76. Errico, C. *et al.* Ultrafast ultrasound localization microscopy for deep super-resolution vascular imaging. *Nature* **527,** 499–502. ISSN: 1476-4687 (Nov. 2015).

77. Couture, O. *et al.* Ultrasound Localization Microscopy and Super-Resolution: A State of the Art. *IEEE Transactions on Ultrasonics, Ferroelectrics, and Frequency Control* **65,** 1304–1320. ISSN: 1525-8955 (Aug. 2018).

78. Lin, F. *et al.* 3-D Ultrasound Localization Microscopy for Identifying Microvascular Morphology Features of Tumor Angiogenesis at a Resolution Beyond the Diffraction Limit of Conventional Ultrasound. *Theranostics* **7,** 196–204. ISSN: 1838-7640 (2017).

79. Foiret, J. *et al.* Ultrasound localization microscopy to image and assess microvasculature in a rat kidney. *Scientific Reports* **7.** ISSN: 2045-2322 (2017).

80. Song, W. *et al.* Magnetic Nanobubbles With Potential for Targeted Drug Delivery and Trimodal Imaging in Breast Cancer: an In Vitro Study. *Nanomedicine* **12,** 991–1009. ISSN: 1748-6963 (2017).
81. Harput, S. *et al.* Two-Stage Motion Correction for Super-Resolution Ultrasound Imaging in Human Lower Limb. *IEEE Transactions on Ultrasonics, Ferroelectrics, and Frequency Control* **65,** 803–814. ISSN: 1525-8955 (2018).
82. Song, P. *et al.* Improved Super-Resolution Ultrasound Microvessel Imaging With Spatiotemporal Nonlocal Means Filtering and Bipartite Graph-Based Microbubble Tracking. *IEEE Transactions on Ultrasonics, Ferroelectrics, and Frequency Control* **65,** 149–167. ISSN: 1525-8955 (2018).
83. Christensen-Jeffries, K. *et al.* Super-resolution Ultrasound Imaging. *Ultrasound in Medicine & Biology* **46,** 865–891. ISSN: 0301-5629 (Apr. 2020).
84. Christensen-Jeffries, K. *et al.* In Vivo Acoustic Super-Resolution and Super-Resolved Velocity Mapping Using Microbubbles. *IEEE Transactions on Medical Imaging* **34,** 433–440. ISSN: 1558-254X (2015).
85. Siepmann, M. *et al. Imaging tumor vascularity by tracing single microbubbles* in *2011 IEEE International Ultrasonics Symposium* (IEEE, 2011).
86. Desailly, Y. *et al.* Contrast enhanced ultrasound by real-time spatiotemporal filtering of ultrafast images. *Physics in Medicine and Biology* **62,** 31–42. ISSN: 1361-6560 (Dec. 2016).
87. Couture, O., Fink, M. & Tanter, M. Ultrasound contrast plane wave imaging. *IEEE Transactions on Ultrasonics, Ferroelectrics and Frequency Control* **59.** ISSN: 0885-3010 (Dec. 2012).
88. Muleki-Seya, P. *et al.* Ultrafast Radial Modulation Imaging. *IEEE Transactions on Ultrasonics, Ferroelectrics, and Frequency Control* **67,** 598–611. ISSN: 1525-8955 (2020).
89. Zhao, F. *et al.* A Targeted Molecular Localization Imaging Method Applied to Tumor Microvasculature. *Investigative Radiology* **56,** 197–206. ISSN: 0020-9996 (Sept. 2020).
90. Van Raaij, M. E. *et al.* Functional micro-ultrasound imaging of rodent cerebral hemodynamics. *NeuroImage* **58,** 100–108. ISSN: 1053-8119 (Sept. 2011).
91. Leow, C. H. *et al.* Flow Velocity Mapping Using Contrast Enhanced High-Frame-Rate Plane Wave Ultrasound and Image Tracking: Methods and Initial in Vitro and in Vivo Evaluation. *Ultrasound in Medicine & Biology* **41,** 2913–2925. ISSN: 0301-5629 (Nov. 2015).
92. Maresca, D. *et al.* Noninvasive Imaging of the Coronary Vasculature Using Ultrafast Ultrasound. *JACC: Cardiovascular Imaging* **11,** 798–808. ISSN: 1936-878X (2018).
93. Ten Kate, G. L. *et al.* Far-Wall Pseudoenhancement During Contrast-Enhanced Ultrasound of the Carotid Arteries: Clinical Description and In Vitro Reproduction. *Ultrasound in Medicine & Biology* **38,** 593–600. ISSN: 0301-5629 (Apr. 2012).
94. Helfield, B. A Review of Phospholipid Encapsulated Ultrasound Contrast Agent Microbubble Physics. *Ultrasound in Medicine & Biology* **45,** 282–300. ISSN: 0301-5629 (2019).

95. Szabo, T. L. in *Diagnostic Ultrasound Imaging: Inside Out* 735–763 (Elsevier, 2014). ISBN: 9780123964878.
96. Sehgal, C. M. & Greenleaf, J. F. Scattering of Ultrasound by Tissues. *Ultrasonic Imaging* **6,** 60–80. ISSN: 1096-0910 (1984).
97. Boido, D. *et al.* Mesoscopic and microscopic imaging of sensory responses in the same animal. *Nature Communications* **10.** ISSN: 2041-1723 (2019).
98. Aydin, A.-K. *et al.* Transfer functions linking neural calcium to single voxel functional ultrasound signal. *Nature Communications* **11.** ISSN: 2041-1723 (2020).
99. Masamoto, K. & Kanno, I. Anesthesia and the Quantitative Evaluation of Neurovascular Coupling. *Journal of Cerebral Blood Flow & Metabolism* **32,** 1233–1247. ISSN: 1559-7016 (Apr. 2012).
100. Ophir, J. & Parker, K. J. Contrast agents in diagnostic ultrasound. *Ultrasound in Medicine & Biology* **15,** 319–333. ISSN: 0301-5629 (1989).
101. Frinking, P. *et al.* Three Decades of Ultrasound Contrast Agents: A Review of the Past, Present and Future Improvements. *Ultrasound in Medicine & Biology* **46,** 892–908. ISSN: 0301-5629 (Apr. 2020).
102. Schneider, M. *et al.* BR1: a new ultrasonographic contrast agent based on sulfur hexafluoride-filled microbubbles. *Investigative radiology* **30,** 451–457 (1995).
103. Unger, E. *et al.* Session 8: Gas-filled lipid bilayers as ultrasound contrast agents. *Investigative Radiology* **29,** S134–S136. ISSN: 15360210 (1994).
104. Schneider, M. *et al.* BR38, a New Ultrasound Blood Pool Agent. *Investigative Radiology* **46,** 486–494. ISSN: 0020-9996 (Aug. 2011).
105. Schneider, M. *et al.* Gray-scale liver enhancement in VX2 tumor-bearing rabbits using BR14, a new ultrasonographic contrast agent. *Investigative Radiology* **32,** 410–417. ISSN: 00209996 (1997).
106. Segers, T. *et al.* Monodisperse Versus Polydisperse Ultrasound Contrast Agents: Non-Linear Response, Sensitivity, and Deep Tissue Imaging Potential. *Ultrasound in Medicine & Biology* **44,** 1482–1492. ISSN: 0301-5629 (2018).
107. Ferrara, K. W., Borden, M. A. & Zhang, H. Lipid-Shelled Vehicles: Engineering for Ultrasound Molecular Imaging and Drug Delivery. *Accounts of Chemical Research* **42,** 881–892. ISSN: 1520-4898 (2009).
108. Moestue, S. A., Gribbestad, I. S. & Hansen, R. Intravascular Targets for Molecular Contrast-Enhanced Ultrasound Imaging. *International Journal of Molecular Sciences* **13,** 6679–6697. ISSN: 1422-0067 (2012).
109. Hobbs, S. K. *et al.* Regulation of transport pathways in tumor vessels: Role of tumor type and microenvironment. *Proceedings of the National Academy of Sciences* **95,** 4607–4612. ISSN: 1091-6490 (Apr. 1998).
110. Maeda, H., Bharate, G. Y. & Daruwalla, J. Polymeric drugs for efficient tumor-targeted drug delivery based on EPR-effect. *European Journal of Pharmaceutics and Biopharmaceutics* **71,** 409–419. ISSN: 0939-6411 (2009).

111. Gao, Y. *et al.* Ultrasound molecular imaging of ovarian cancer with CA-125 targeted nanobubble contrast agents. *Nanomedicine: Nanotechnology, Biology and Medicine* **13,** 2159–2168. ISSN: 1549-9634 (2017).

112. Hamano, N. *et al.* Development of Antibody-Modified Nanobubbles Using Fc-Region-Binding Polypeptides for Ultrasound Imaging. *Pharmaceutics* **11,** 283. ISSN: 1999-4923 (2019).

113. De Leon, A. *et al.* Contrast enhanced ultrasound imaging by nature-inspired ultrastable echogenic nanobubbles. *Nanoscale* **11,** 15647–15658. ISSN: 2040-3372 (2019).

114. Fokong, S. *et al.* Ultrasound Molecular Imaging of E-Selectin in Tumor Vessels Using Poly n-Butyl Cyanoacrylate Microbubbles Covalently Coupled to a Short Targeting Peptide. *Investigative Radiology* **48,** 843–850. ISSN: 0020-9996 (Dec. 2013).

115. Li, B. *et al.* Functionalized polymer microbubbles as new molecular ultrasound contrast agent to target P-selectin in thrombus. *Biomaterials* **194,** 139–150. ISSN: 0142-9612 (2019).

116. Alzaraa, A. *et al.* Targeted microbubbles in the experimental and clinical setting. *The American Journal of Surgery* **204,** 355–366. ISSN: 0002-9610 (Sept. 2012).

117. Pochon, S. *et al.* BR55: A Lipopeptide-Based VEGFR2-Targeted Ultrasound Contrast Agent for Molecular Imaging of Angiogenesis. *Investigative Radiology* **45,** 89–95. ISSN: 0020-9996 (2010).

118. Willmann, J. K. *et al.* Dual-targeted Contrast Agent for US Assessment of Tumor Angiogenesis in Vivo. *Radiology* **248,** 936–944. ISSN: 1527-1315 (Sept. 2008).

119. Schumann, P. A. *et al.* Targeted-microbubble binding selectively to GPIIb IIIa receptors of platelet thrombi. *Investigative Radiology* **37,** 587–593. ISSN: 00209996 (Nov. 2002).

120. Wang, X. *et al.* Novel Single-Chain Antibody-Targeted Microbubbles for Molecular Ultrasound Imaging of Thrombosis: Validation of a Unique Noninvasive Method for Rapid and Sensitive Detection of Thrombi and Monitoring of Success or Failure of Thrombolysis in Mice. *Circulation* **125,** 3117–3126. ISSN: 1524-4539 (2012).

121. Hingot, V. *et al.* Microvascular flow dictates the compromise between spatial resolution and acquisition time in Ultrasound Localization Microscopy. *Scientific Reports* **9.** ISSN: 2045-2322 (2019).

122. Shih, R. *et al.* Flow-focusing regimes for accelerated production of monodisperse drug-loadable microbubbles toward clinical-scale applications. *Lab on a Chip* **13,** 4816. ISSN: 1473-0189 (2013).

123. Talu, E. *et al.* Tailoring the Size Distribution of Ultrasound Contrast Agents: Possible Method for Improving Sensitivity in Molecular Imaging. *Molecular Imaging* **6,** 7290.2007.00034. ISSN: 1536-0121 (Nov. 2007).

124. Nakatsuka, M. A. *et al.* Aptamer-Crosslinked Microbubbles: Smart Contrast Agents for Thrombin-Activated Ultrasound Imaging. *Advanced Materials* **24,** 6010–6016. ISSN: 1521-4095 (Sept. 2012).

125. Kaufmann, B. A. & Lindner, J. R. Molecular imaging with targeted contrast ultrasound. *Current Opinion in Biotechnology* **18,** 11–16. ISSN: 0958-1669 (Feb. 2007).
126. Walsby, A. E. Gas vesicles. *Microbiological Reviews* **58,** 94–144. ISSN: 01460749 (Mar. 1994).
127. Yang, Y. *et al.* Ultrasonic Characteristics and Cellular Properties of Anabaena Gas Vesicles. *Ultrasound in Medicine and Biology* **43,** 2862–2870. ISSN: 0301-5629 (Dec. 2017).
128. Maresca, D. *et al.* Nonlinear ultrasound imaging of nanoscale acoustic biomolecules. *Applied Physics Letters* **110,** 073704. ISSN: 1077-3118 (Feb. 2017).
129. Chadderdon, S. M. *et al.* Proinflammatory Endothelial Activation Detected by Molecular Imaging in Obese Nonhuman Primates Coincides With Onset of Insulin Resistance and Progressively Increases With Duration of Insulin Resistance. *Circulation* **129,** 471–478. ISSN: 1524-4539 (Jan. 2014).
130. Hamilton, A. J. *et al.* Intravascular Ultrasound Molecular Imaging of Atheroma Components In Vivo. *Journal of the American College of Cardiology* **43,** 453–460. ISSN: 07351097 (Feb. 2004).
131. Kosareva, A. *et al.* Seeing the Invisible—Ultrasound Molecular Imaging. *Ultrasound in Medicine and Biology* **46,** 479–497. ISSN: 0301-5629 (Mar. 2020).
132. Abou-Elkacem, L., Bachawal, S. V. & Willmann, J. K. Ultrasound molecular imaging: Moving toward clinical translation. *European Journal of Radiology* **84,** 1685–1693. ISSN: 0720-048X (Sept. 2015).
133. De Jong, K. *et al.* Short survival of phosphatidylserine-exposing red blood cells in murine sickle cell anemia. *Blood* **98,** 1577–1584. ISSN: 0006-4971 (Sept. 2001).
134. Garcia, J. S. *et al.* Haematological alterations in Rattus norvegicus (Wistar) experimentally infected with Echinostoma paraensei (Trematoda: Echinostomatidae). *Experimental Parasitology* **131,** 300–303. ISSN: 0014-4894 (2012).
135. Hurt, R. *et al.* Directed evolution of a genetically encoded contrast agent for ultrasound (Sept. 2021).
136. Desai, M. *et al.* Molecular imaging with engineered physiology. *Nature Communications* **7.** ISSN: 2041-1723 (Dec. 2016).
137. Ohlendorf, R. *et al.* Target-responsive vasoactive probes for ultrasensitive molecular imaging. *Nature Communications* **11.** ISSN: 2041-1723 (2020).
138. Dhanaliwala, A. H., Hossack, J. A. & Mauldin, F. W. Assessing and improving acoustic radiation force image quality using a 1.5-D transducer design. *IEEE Transactions on Ultrasonics, Ferroelectrics, and Frequency Control* **59,** 1602–1608. ISSN: 1525-8955 VO - 59 (2012).
139. Hu, C.-M. J. *et al.* Erythrocyte membrane-camouflaged polymeric nanoparticles as a biomimetic delivery platform. *Proceedings of the National Academy of Sciences* **108,** 10980–10985. ISSN: 1091-6490 (2011).
140. DeNardo, L. & Luo, L. Genetic strategies to access activated neurons. *Current Opinion in Neurobiology* **45,** 121–129. ISSN: 0959-4388 (Aug. 2017).

141. Lin, M. Z. & Schnitzer, M. J. Genetically encoded indicators of neuronal activity. *Nature Neuroscience* **19,** 1142–1153. ISSN: 1546-1726 (Aug. 2016).

142. Ling, B. *et al.* Biomolecular Ultrasound Imaging of Phagolysosomal Function. *ACS Nano* **14,** 12210–12221. ISSN: 1936-086X (Sept. 2020).

143. Brentjens, R. J. *et al.* CD19-Targeted T Cells Rapidly Induce Molecular Remissions in Adults with Chemotherapy-Refractory Acute Lymphoblastic Leukemia. *Science Translational Medicine* **5.** ISSN: 1946-6242 (2013).

144. Szurmant, H. & Ordal, G. W. Diversity in Chemotaxis Mechanisms among the Bacteria and Archaea. *Microbiology and Molecular Biology Reviews* **68,** 301–319. ISSN: 1092-2172 (2004).

145. Jarrell, K. F. & McBride, M. J. The surprisingly diverse ways that prokaryotes move. *Nature Reviews Microbiology* **6,** 466–476. ISSN: 17401526 (2008).

146. Hayes, P. K. & Walsby, A. E. The inverse correlation between width and strength of gas vesicles in cyanobacteria. **1617** (2007).

147. Blaurock, A. E. & Walsby, A. E. Crystalline structure of the gas vesicle wall from Anabaena flos-aquae. *Journal of Molecular Biology* **105,** 183–199. ISSN: 00222836 (1976).

148. Offner, S. *et al.* Structural characteristics of halobacterial gas vesicles. *Microbiology* **144,** 1331–1342. ISSN: 13500872 (1998).

149. Walsby, A. E. Permeability of gas vesicles to perfluorocyclobutane. *Journal of General Microbiology* **128,** 1679–1684. ISSN: 00221287 (1982).

150. Pfeifer, F. Distribution, formation and regulation of gas vesicles. *Nature Reviews Microbiology* **10,** 705–715. ISSN: 17401526 (Oct. 2012).

151. Buchholz, B. E. E., Hayes, P. K. & Walsby, A. E. The distribution of the outer gas vesicle protein, GvpC, on the Anabaena gas vesicle, and its ratio to GvpA. *Journal of General Microbiology* **139,** 2353–2363. ISSN: 00221287 (1993).

152. McMaster, T. J., Miles, M. J. & Walsby, A. E. Direct observation of protein secondary structure in gas vesicles by atomic force microscopy. *Biophysical Journal* **70,** 2432–2436. ISSN: 00063495 (1996).

153. Sivertsen, A. C. *et al.* Solid-State NMR Evidence for Inequivalent GvpA Subunits in Gas Vesicles. *Journal of Molecular Biology* **387,** 1032–1039. ISSN: 00222836 (2009).

154. Sivertsen, A. C. *et al.* Solid-state NMR characterization of gas vesicle structure. *Biophysical Journal* **99,** 1932–1939. ISSN: 15420086 (2010).

155. Strunk, T. *et al.* Structural model of the gas vesicle protein GvpA and analysis of GvpA mutants in vivo. *Molecular Microbiology* **81,** 56–68. ISSN: 0950382X (2011).

156. Bayro, M. J. *et al.* An amyloid organelle, solid-state NMR evidence for cross-\$$\beta$\$ assembly of gas vesicles. *Journal of Biological Chemistry* **287,** 3479–3484. ISSN: 00219258 (2012).

157. Ezzeldin, H. M., Klauda, J. B. & Solares, S. D. Modeling of the major gas vesicle protein, GvpA: From protein sequence to vesicle wall structure. *Journal of Structural Biology* **179,** 18–28. ISSN: 10478477 (2012).

158. Knitsch, R. *et al.* Mutations in the major gas vesicle protein GvpA and impacts on gas vesicle formation in Haloferax volcanii. *Molecular Microbiology* **106,** 530–542. ISSN: 13652958 (2017).

159. Li, N. & Cannon, M. C. Gas vesicle genes identified in Bacillus megaterium and functional expression in Escherichia coli. *Journal of Bacteriology* **180,** 2450–2458. ISSN: 00219193 (May 1998).

160. Lakshmanan, A. *et al.* Preparation of biogenic gas vesicle nanostructures for use as contrast agents for ultrasound and MRI. *Nature Protocols* **12,** 2050–2080. ISSN: 17502799 (2017).

161. Dutka, P. *et al.* Measuring gas vesicle dimensions by electron microscopy. *Protein Science* **30,** 1081–1086. ISSN: 1469896X (2021).

162. Sehnal, D. *et al.* MOLE 2.0: advanced approach for analysis of biomacromolecular channels. *Journal of cheminformatics* **5,** 1–13 (2013).

163. Ismail, A. F., Khulbe, K. C. & Matsuura, T. Gas separation membranes. *Switz. Springer* **10,** 973–978 (2015).

164. Horgan, C. O. & Murphy, J. G. Magic angles for fibrous incompressible elastic materials. *Proceedings of the Royal Society A* **474,** 20170728 (2018).

165. Walsby, A. E. The elastic compressibility of gas vesicles. *Proceedings of the Royal Society of London - Biological Sciences* **216,** 355–368. ISSN: 09628452 (1982).

166. Walsby, A. E. Structure and function of gas vacuoles. *Bacteriological reviews* **36,** 1–32. ISSN: 00053678 (1972).

167. Tashiro, Y. *et al.* Molecular genetic and physical analysis of gas vesicles in buoyant enterobacteria. *Environmental Microbiology* **18,** 1264–1276. ISSN: 14622920 (2016).

168. Dunton, P. G. *et al.* Analysis of tryptic digests indicates regions of GvpC that bind to gas vesicles of Anabaena flos-aquae. *Microbiology* **152,** 1661–1669. ISSN: 13500872 (2006).

169. Dutka, P. *et al.* Structure of Anabaena flos-aquae gas vesicles revealed by cryo-ET. *Structure* **31,** 518–528. ISSN: 18784186 (2023).

170. Walsby, A. E. The permeability of blue-green algal gas-vacuole membranes to gas. *Proceedings of the Royal Society of London. Series B. Biological Sciences* **173,** 235–255. ISSN: 0080-4649 (1969).

171. Völkner, K., Jost, A. & Pfeifer, F. Accessory Gvp Proteins Form a Complex During Gas Vesicle Formation of Haloarchaea. *Frontiers in Microbiology* **11.** ISSN: 1664302X (2020).

172. Maresca, D. *et al.* Nonlinear X-Wave Ultrasound Imaging of Acoustic Biomolecules. *Physical Review X* **8,** 041002. ISSN: 21603308 (Oct. 2018).

173. Studier, F. W. Protein production by auto-induction in high-density shaking cultures. *Protein expression and purification* **41,** 207–234 (2005).

174. Zivanov, J. *et al.* New tools for automated high-resolution cryo-EM structure determination in RELION-3. *Elife* **7,** e42166 (2018).

175. Zhang, K. Gctf: Real-time CTF determination and correction. *Journal of structural biology* **193,** 1–12 (2016).

176. Punjani, A. *et al.* cryoSPARC: algorithms for rapid unsupervised cryo-EM structure determination. *Nature methods* **14,** 290–296 (2017).

177. Goddard, T. D. *et al.* UCSF ChimeraX: Meeting modern challenges in visualization and analysis. *Protein Science* **27,** 14–25 (2018).

178. Emsley, P. *et al.* Features and development of Coot. *Acta Crystallographica Section D: Biological Crystallography* **66,** 486–501 (2010).

179. Croll, T. I. ISOLDE: a physically realistic environment for model building into low-resolution electron-density maps. *Acta Crystallographica Section D: Structural Biology* **74,** 519–530 (2018).

180. Liebschner, D. *et al.* Macromolecular structure determination using X-rays, neutrons and electrons: recent developments in Phenix. *Acta Crystallographica Section D: Structural Biology* **75,** 861–877 (2019).

181. Bepler, T. *et al.* Positive-unlabeled convolutional neural networks for particle picking in cryo-electron micrographs. *Nature methods* **16,** 1153–1160 (2019).

182. Pettersen, E. F. *et al.* UCSF Chimera—a visualization system for exploratory research and analysis. *Journal of computational chemistry* **25,** 1605–1612 (2004).

183. Jumper, J. *et al.* Highly accurate protein structure prediction with AlphaFold. *Nature* **596,** 583–589 (2021).

184. Mirdita, M. *et al.* ColabFold: making protein folding accessible to all. *Nature Methods* **19,** 1–4 (2022).

185. Rice, P., Longden, I. & Bleasby, A. EMBOSS: the European molecular biology open software suite. *Trends in genetics* **16,** 276–277 (2000).

186. Ashkenazy, H. *et al.* ConSurf 2016: an improved methodology to estimate and visualize evolutionary conservation in macromolecules. *Nucleic acids research* **44,** W344–W350 (2016).

187. Finn, R. D., Clements, J. & Eddy, S. R. HMMER web server: interactive sequence similarity searching. *Nucleic acids research* **39,** W29–W37 (2011).

188. Brown, N. P., Leroy, C. & Sander, C. MView: a web-compatible database search or multiple alignment viewer. *Bioinformatics (Oxford, England)* **14,** 380–381 (1998).

189. Crooks, G. E. *et al.* WebLogo: a sequence logo generator. *Genome research* **14,** 1188–1190 (2004).

190. Gautier, R. *et al.* HELIQUEST: a web server to screen sequences with specific $α$-helical properties. *Bioinformatics* **24,** 2101–2102 (2008).

191. Waterhouse, A. *et al.* SWISS-MODEL: homology modelling of protein structures and complexes. *Nucleic acids research* **46,** W296–W303 (2018).

192. Van Zundert, G. C. P. *et al.* The HADDOCK2. 2 web server: user-friendly integrative modeling of biomolecular complexes. *Journal of molecular biology* **428,** 720–725 (2016).

193. Walsby, A. E. & Hayes, P. K. Gas vesicle proteins. *Biochem. J* **322,** 313–322 (1989).

194. Rötzschke, O. *et al.* A pH-sensitive histidine residue as control element for ligand release from HLA-DR molecules. *Proceedings of the National Academy of Sciences* **99,** 16946–16950. ISSN: 0027-8424 (2002).

195. Zhuang, T. *et al.* NMR-based conformational ensembles explain pH-gated opening and closing of OmpG channel. *Journal of the American Chemical Society* **135,** 15101–15113. ISSN: 0002-7863 (2013).

196. Hu, X. *et al.* High-resolution design of a protein loop. *Proceedings of the National Academy of Sciences of the United States of America* **104,** 17668–17673. ISSN: 00278424 (Nov. 2007).

197. Van Noort, C. W., Honorato, R. V. & Bonvin, A. M. J. J. Information-driven modeling of biomolecular complexes. *Current Opinion in Structural Biology* **70,** 70–77. ISSN: 0959-440X (2021).

198. Honorato, R. V. *et al.* Structural biology in the clouds: the WeNMR-EOSC ecosystem. *Frontiers in molecular biosciences* **8,** 729513. ISSN: 2296-889X (2021).

199. Surewaard, B. G. J. & Kubes, P. Measurement of bacterial capture and phagosome maturation of Kupffer cells by intravital microscopy. *Methods* **128,** 12–19. ISSN: 1046-2023 (2017).

200. Dragotakes, Q. *et al.* Macrophages use a bet-hedging strategy for antimicrobial activity in phagolysosomal acidification. *The Journal of Clinical Investigation* **130,** 3805–3819. ISSN: 0021-9738 (July 2020).

201. Lee, S., Zhang, Z. & Yu, Y. Real-Time Simultaneous Imaging of Acidification and Proteolysis in Single Phagosomes Using Bifunctional Janus-Particle Probes. *Angewandte Chemie International Edition* **60,** 26734–26739. ISSN: 1433-7851 (Dec. 2021).

202. Canton, J. *et al.* Contrasting phagosome pH regulation and maturation in human M1 and M2 macrophages. *Molecular Biology of the Cell* **25,** 3330–3341. ISSN: 1059-1524 (Aug. 2014).

203. Shen, Y. *et al.* pHuji, a pH-sensitive red fluorescent protein for imaging of exo- and endocytosis. *Journal of Cell Biology* **207,** 419–432. ISSN: 0021-9525 (Nov. 2014).

204. Shen, Y. *et al.* Rational Engineering of an Improved Genetically Encoded pH Sensor Based on Superecliptic pHluorin. *ACS Sensors* **8,** 3014–3022 (Aug. 2023).

205. Liu, A. *et al.* pHmScarlet is a pH-sensitive red fluorescent protein to monitor exocytosis docking and fusion steps. *Nature Communications* **12,** 1413. ISSN: 2041-1723 (2021).

206. Tantama, M., Hung, Y. P. & Yellen, G. Imaging Intracellular pH in Live Cells with a Genetically Encoded Red Fluorescent Protein Sensor. *Journal of the American Chemical Society* **133,** 10034–10037. ISSN: 0002-7863 (July 2011).

207. Hurt, R. C. *et al.* Directed Evolution of Acoustic Reporter Genes Using High-Throughput Acoustic Screening. *bioRxiv,* 2024.03.30.587094 (Jan. 2024).

208. Krabbe, G. *et al.* Functional impairment of microglia coincides with Beta-amyloid deposition in mice with Alzheimer-like pathology. eng. *PloS one* **8,** e60921. ISSN: 1932-6203 (Electronic) (2013).

209. Tahara, N. *et al.* Boosting auto-induction of recombinant proteins in Escherichia coli with glucose and lactose additives. *Protein and Peptide Letters* **28,** 1180 (2020).

210. Meng, E. C. *et al.* UCSF ChimeraX: Tools for structure building and analysis. *Protein Science* **32,** e4792. ISSN: 0961-8368 (2023).

211. Gasteiger, E. *et al.* ExPASy: the proteomics server for in-depth protein knowledge and analysis. *Nucleic acids research* **31,** 3784–3788. ISSN: 1362-4962 (2003).

212. Montaldo, G., Urban, A. & Macé, E. Functional ultrasound neuroimaging. *Annual Review of Neuroscience* **45,** 491–513. ISSN: 0147-006X (2022).

213. Bimbard, C. *et al.* Multi-scale mapping along the auditory hierarchy using high-resolution functional ultrasound in the awake ferret. *eLife* **7,** 1–14. ISSN: 2050084X (2018).

214. Blaize, K. *et al.* Functional ultrasound imaging of deep visual cortex in awake non-human primates. *Proceedings of the National Academy of Sciences of the United States of America* **117,** 14453–14463. ISSN: 10916490 (2020).

215. Mace, É. *et al. Whole-Brain Functional Ultrasound Imaging Reveals Brain Modules for Visuomotor Integration* 2018.

216. Rau, R. *et al.* 3D functional ultrasound imaging of pigeons. *NeuroImage* **183,** 469–477. ISSN: 10959572 (2018).

217. Tiran, E. *et al.* Transcranial Functional Ultrasound Imaging in Freely Moving Awake Mice and Anesthetized Young Rats without Contrast Agent. *Ultrasound in Medicine and Biology* **43,** 1679–1689. ISSN: 1879291X (2017).

218. Urban, A. *et al.* Chronic assessment of cerebral hemodynamics during rat forepaw electrical stimulation using functional ultrasound imaging. *NeuroImage* **101,** 138–149. ISSN: 10959572 (2014).

219. Pinton, G. *et al.* Attenuation, scattering, and absorption of ultrasound in the skull bone. *Medical Physics* **39,** 299–307. ISSN: 00942405 (2012).

220. Waasdorp, R. *et al.* Adaptive transcranial ultrasound Doppler imaging of the brain. *bioRxiv,* 2025.05.27.656275 (2025).

221. Chômas, J. E. *et al.* Mechanisms of contrast agent destruction. *IEEE Transactions on Ultrasonics, Ferroelectrics, and Frequency Control* **48,** 232–248. ISSN: 08853010 (2001).

222. Emmer, M. *et al.* Radial modulation of single microbubbles. *IEEE Transactions on Ultrasonics, Ferroelectrics, and Frequency Control* **56,** 2370–2379. ISSN: 08853010 (2009).

223. Chinchilla, L. *et al.* Numerical investigations of anisotropic structures of red blood cell aggregates on ultrasonic backscattering. *The Journal of the Acoustical Society of America* **149,** 2415–2425 (2021).

224. Deymier, P. A. *Acoustic metamaterials and phononic crystals* ISBN: 9783642312311 (Springer Heidelberg, 2013).

225. Leroy, V. *et al.* Transmission of ultrasound through a single layer of bubbles. *European Physical Journal E* **29,** 123–130. ISSN: 12928941 (2009).

226. Matalliotakis, A. & Verweij, M. D. Polydisperse versus monodisperse microbubbles: A simulation study for contrast-enhanced ultrasound imaging (May 2024).

227. De Monchy, R. *et al.* Coherent and incoherent ultrasound backscatter from cell aggregates. *The Journal of the Acoustical Society of America* **140,** 2173–2184. ISSN: 0001-4966 (Sept. 2016).

228. Lee, K. Y. & Mooney, D. J. Alginate: Properties and biomedical applications. *Progress in Polymer Science (Oxford)* **37,** 106–126. ISSN: 00796700 (2012).

229. Dhamecha, D. *et al.* Applications of alginate microspheres in therapeutics delivery and cell culture: Past, present and future. *International Journal of Pharmaceutics* **569,** 118627. ISSN: 18733476 (2019).

230. Hu, T. & Lo, A. C. Y. Collagen–alginate composite hydrogel: Application in tissue engineering and biomedical sciences. *Polymers* **13.** ISSN: 20734360 (2021).

231. De Jong, N. in *Advances in Echo Imaging Using Contrast Enhancement* 39–64 (Springer Netherlands, 1997).

232. Yao, Y. *et al.* Self-assembly of protein superstructures by physical interactions under cytoplasm-like conditions. *Biophysical Journal.* ISSN: 00063495 (May 2021).

233. Leroy, V. *et al.* Design and characterization of bubble phononic crystals. *Applied Physics Letters* **95,** 1–4. ISSN: 00036951 (2009).

234. Hu, Y. *et al.* Shape controllable microgel particles prepared by microfluidic combining external ionic crosslinking. *Biomicrofluidics* **6,** 1–9. ISSN: 19321058 (2012).

235. Moreira, A. *et al.* Production of hydrogel microparticles in microfluidic devices: a review. *Microfluidics and Nanofluidics* **25,** 1–24. ISSN: 16134990 (2021).

236. Pittermannová, A. *et al.* Microfluidic fabrication of composite hydrogel microparticles in the size range of blood cells. *RSC Advances* **6,** 103532–103540. ISSN: 20462069 (2016).

237. Bar-Zion, A. *et al. Acoustically Detonated Biomolecules for Genetically Encodable Inertial Cavitation* 2019.

238. Farhadi, A. *et al.* Genetically Encoded Phase Contrast Agents for Digital Holographic Microscopy. *Nano Letters.* ISSN: 15306992 (2020).

239. Opitz, C. A. *et al.* Damped elastic recoil of the titin spring in myofibrils of human myocardium. eng. *Proceedings of the National Academy of Sciences of the United States of America* **100,** 12688–12693. ISSN: 0027-8424 (Print) (Oct. 2003).

240. Howells, A. R. *et al.* A drug-selectable acoustic reporter gene system for human cell ultrasound imaging. *Bioengineering & Translational Medicine* **9,** e10584. ISSN: 2380-6761 (Mar. 2024).

241. Fu, M. *et al.* Genetic Modulation of Biosynthetic Gas Vesicles for Ultrasound Imaging. *Small* **20,** 2310008. ISSN: 1613-6810 (Aug. 2024).

242. Mott, B. *et al.* Echocardiographic Ischemic Memory Imaging Through Complement-Mediated Vascular Adhesion of Phosphatidylserine-Containing Microbubbles. *JACC: Cardiovascular Imaging* **9,** 937–946. ISSN: 1936-878X (2016).

243. Anemone, A. *et al.* Imaging tumor acidosis: a survey of the available techniques for mapping in vivo tumor pH. *Cancer and Metastasis Reviews 2019 38:1* **38,** 25–49. ISSN: 1573-7233 (Feb. 2019).

244. Pillai, S. R. *et al.* Causes, consequences, and therapy of tumors acidosis. *Cancer and Metastasis Reviews 2019 38:1* **38,** 205–222. ISSN: 1573-7233 (Mar. 2019).

245. Rabut, C. *et al.* Acoustic tumor paint for real-time imaging, surgical guidance and recurrence monitoring of brain tumors with ultrasound. *bioRxiv,* 2024.12.22.629782 (Jan. 2024).

246. Lai, S. S. M. *et al.* Endosomal-lysosomal dysfunctions in Alzheimer's disease: Pathogenesis and therapeutic interventions. *Metabolic Brain Disease* **36,** 1087–1100. ISSN: 1573-7365 (2021).

247. Harrison, J. S. *et al.* Role of Electrostatic Repulsion in Controlling pH-dependent Conformational Changes of Viral Fusion Proteins. *Structure (London, England : 1993)* **21,** 1085 (July 2013).

248. Colacurcio, D. J. & Nixon, R. A. Disorders of lysosomal acidification—The emerging role of v-ATPase in aging and neurodegenerative disease. *Ageing Research Reviews* **32,** 75–88. ISSN: 1568-1637 (2016).

249. Seemann, R. *et al.* Droplet based microfluidics. *Reports on Progress in Physics* **75.** ISSN: 00344885 (2012).

250. Zhang, C. *et al.* Preparation of alginate hydrogel microparticles using droplet-based microfluidics : a review of methods (2021).

251. Ahenkorah, C. K., Zaitoon, A. & Lim, L.-T. Electrospraying of submicron alginate beads in Canola oil. *Food Hydrocolloids* **150,** 109673. ISSN: 0268-005X (2024).

252. Jonović, M. *et al.* *Immobilized Alcalase on Micron- and Submicron-Sized Alginate Beads as a Potential Biocatalyst for Hydrolysis of Food Proteins* 2021.

253. Winter, K., Born, J. & Pfeifer, F. Interaction of haloarchaeal gas vesicle proteins determined by split-GFP. *Frontiers in Microbiology* **9,** 1–11. ISSN: 1664302X (2018).

A

APPENDIX

Table A1: Cryo-EM Data Collection and Model Refinement Statistics (Related to Figure 3.2)

Data Collection	
Microscope	Titan Krios (Thermo Fisher Scientific)
Magnification	64,000
Voltage (kV)	300
Electron exposure ($e^-/\text{Å}^2$)	30
Exposure time (s)	2.4
Number of fractions	60
Number of movies	4351
Defocus range (µm)	0.25–1.25
Pixel size (Å)	1.37
Detector	K3 (Gatan)
Dose rate detector (e^-/pix/s)	24
Data Processing	
Helical rise (Å)	0.525
Helical twist (°)	-3.874
Final no. of asym. Units	135,780
Global map resolution (Å)	3.2 (FSC=0.143, masked)
Resolution range (local, Å)	3.0–3.5
Map sharpening B-factor (Å^2)	60.8
Model refinement	De-novo
Sequence	GvpB (GvpA2) – Uniprot O68677
Model Composition	
Non-hydrogen atoms	497
Protein residues	65
Validation	
MolProbity score	0.69
Clashscore	0
Rotamer outliers (%)	0
Bond angles RMSD (°)	0.87
Bond lengths RMSD (Å)	0.52
B-factors (Å^2)	77–107
CC values	0.76/0.75 (CC mask/CC volume)
Ramachandran plot	
Favored (residues)	61
Allowed (residues)	1
Disallowed (residues)	1 (V35)

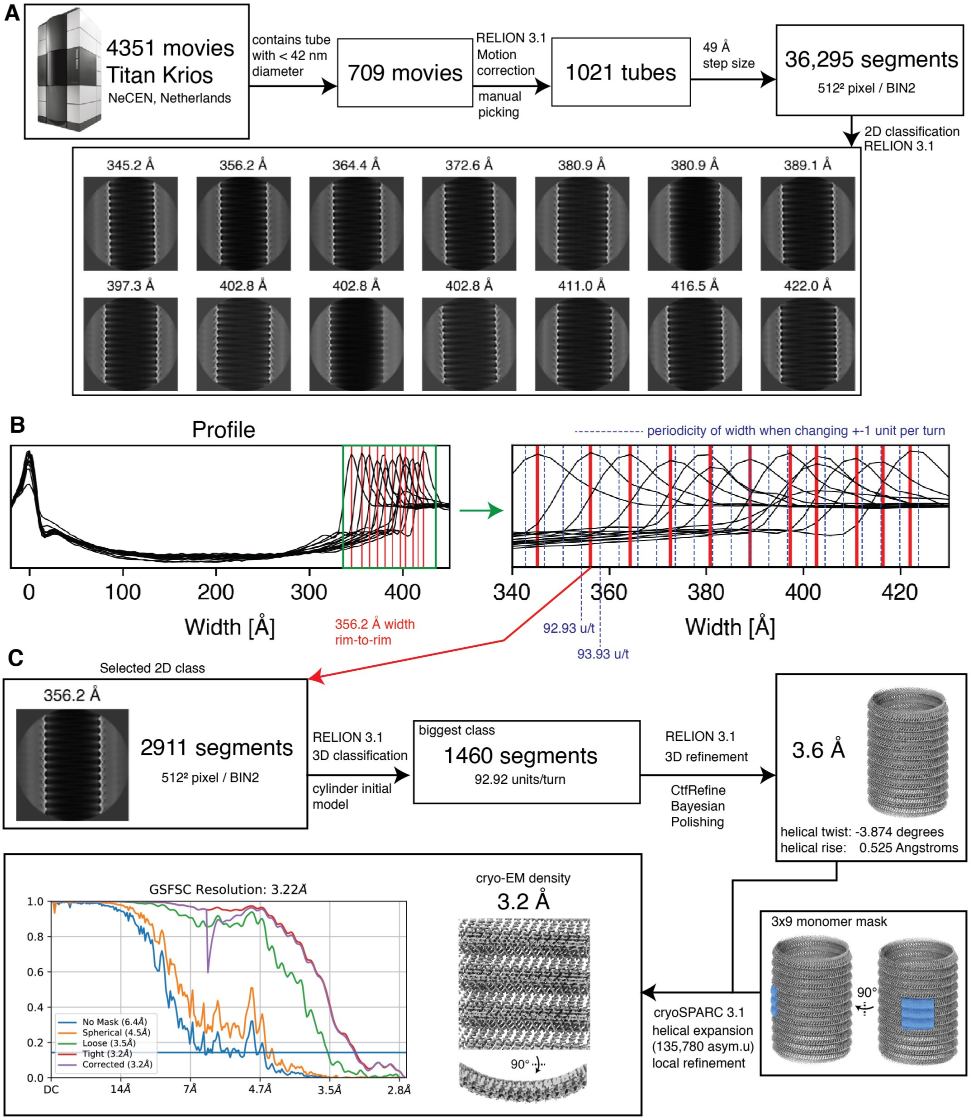

Figure A1: Data processing of *B. megaterium* gas vesicle dataset, related to Figure 3.2. (A) Preprocessing, manual picking, segment extraction and 2D classification leads to 2D class averages of gas vesicles with different diameters. (B) The 2D classes were projected along the helical axis to generate profiles. The profiles were aligned with respect to the left peak. Zooming into the right peaks shows the distribution of gas vesicle widths in the 2D classes. Peaks are marked with a vertical red line. Blue lines indicate the periodicity of widths when an increment of one monomer per helical turn is assumed, based on a side-to-side distance of monomers of 12 Å, leading to a diameter increment of $12/\pi$=3.8 Å. Two to three different helical polymorphs are part of the particle subset belonging to a single 2D class average. (C) Processing steps starting from 2911 selected segments of a particular 2D class. The particle subset from the 2D class was further selected by 3D classification, imposing possible symmetry candidates between 90 and 95 units per wrung to select 1460 segments. Focused refinement on a 3x9 monomer segment of the wall in cryoSPARC 3.1 after symmetry expansion to 135,780 asymmetric units leads to the final result of a 3.2 Å resolution cryo-EM density of the gas vesicle wall.

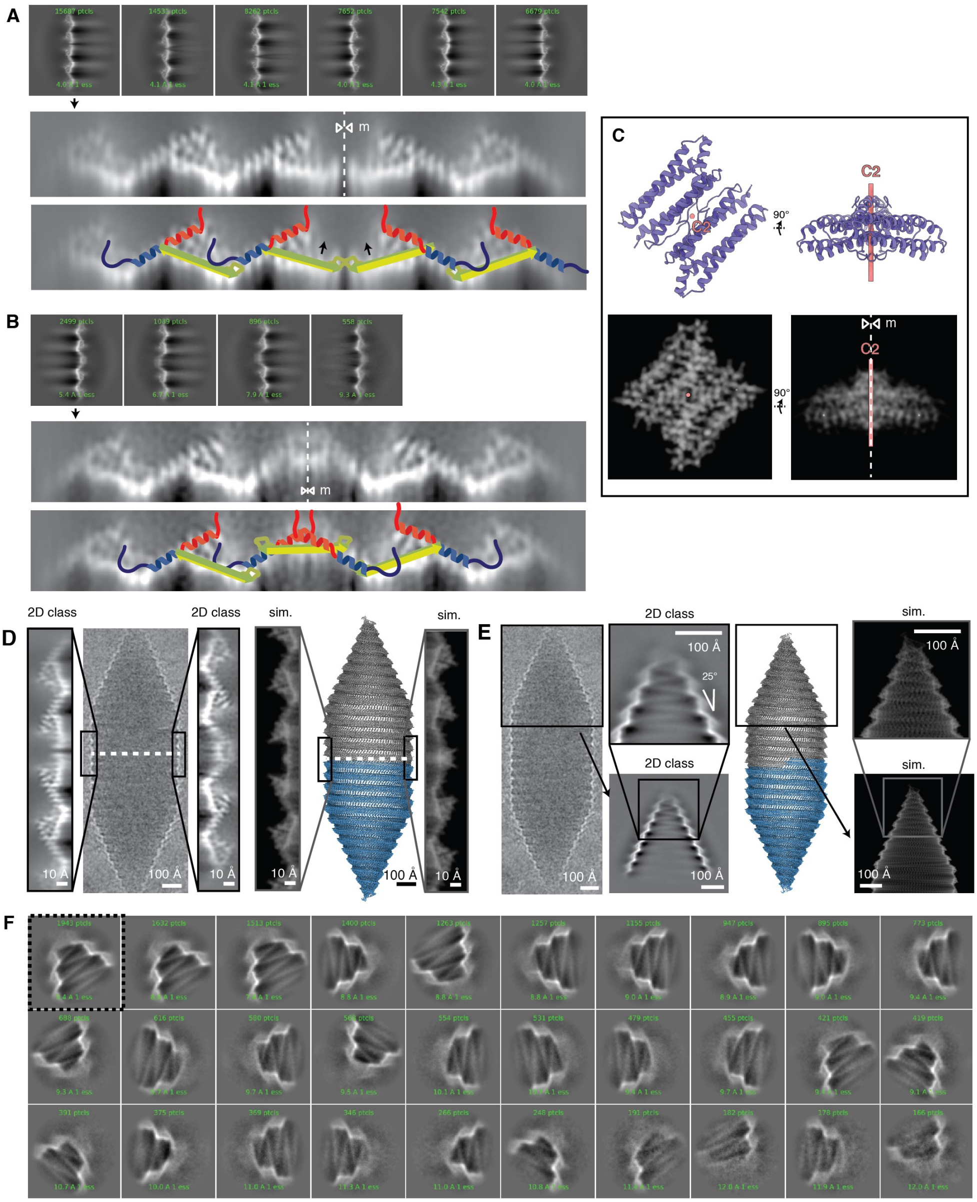

Figure A2: 2D classification of *B. megaterium* seams and tips, related to Figure 3.3. (A) 2D classes from the seam show perfect or near-perfect mirror symmetry. β-hairpins seem to hinge upwards at the seam (black arrows). (B) 2D classes from the putative polarity reversal point. Selected classes were magnified and sharpened for easier depiction. The mirror line is shown (m, dotted white line). A cartoon is drawn on the 2D classes to visualize GvpA molecules with the N-terminus in blue and the C-terminus in red. (C) Demonstration of the fact that views orthogonal to a 180-degree rotation axis show mirror symmetry in projection. (D) 2D class from the seam and polarity reversal point and simulated EM density from the pseudo-atomic model are in close agreement. (E) Pseudo-atomic model of a GV with simulated 2D projections of the tip, closely matching the experimental data. The 2D class average of gas vesicle tips with large box size reveals a linear decrease in radius at the tips with a cone angle of 25°.

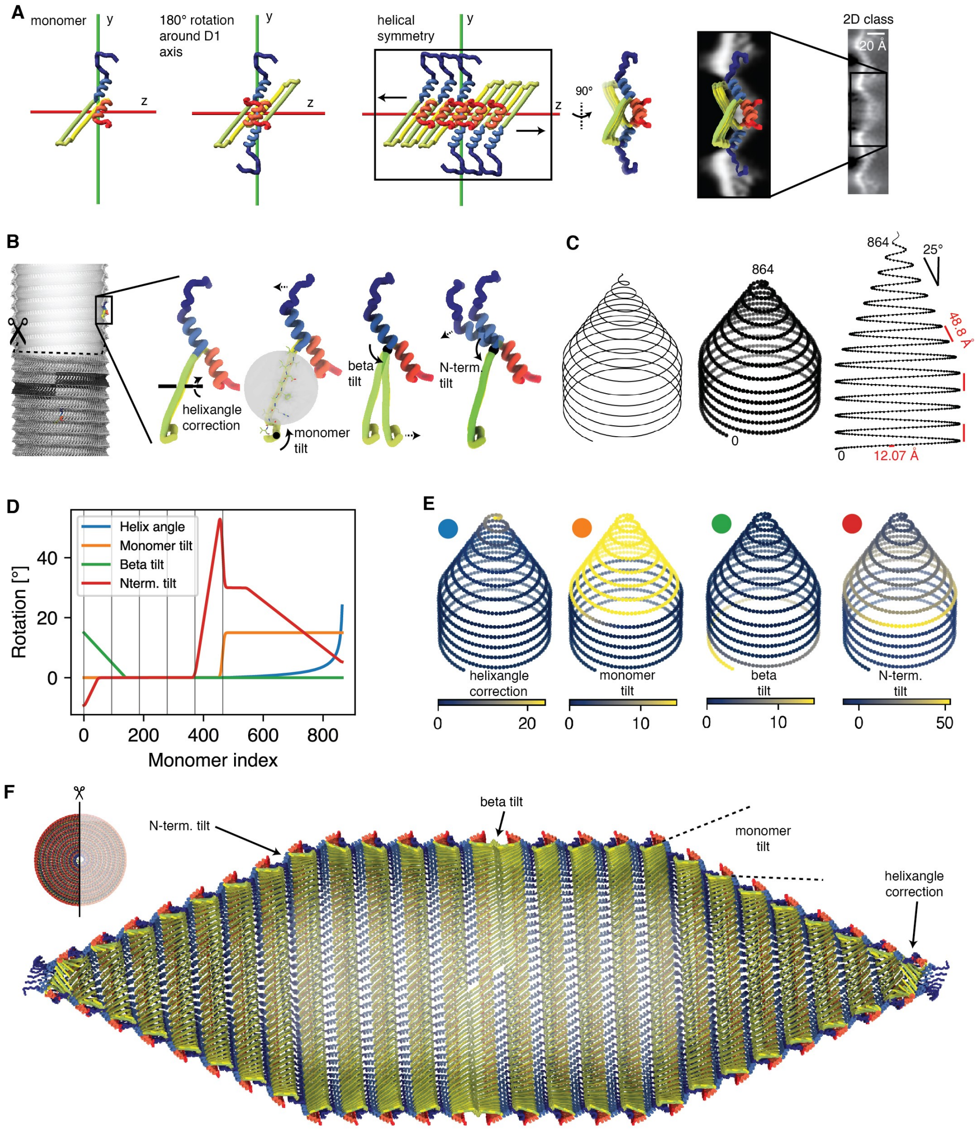

Figure A3: Construction of pseudo-atomic model of a whole *B. megaterium* GV, related to Figure 3.3. (A) A GvpA2 monomer was placed next to the symmetry axis (along x) such that a 180° rotation would reproduce a view corresponding to the experimental 2D class average. The β-sheets meet in an angle at this stage, which is later corrected by tilting the sheets. (B) Four rotation parameters (helix angle correction, monomer tilt, β-hairpin tilt and N-term. tilt) used in the model are visualized. (C) The model is based on a helical curve in space with a linearly decreasing radius in the cones. The pitch in both the cylinder and cone is 48.8 Å. 835 monomers are placed equidistantly on the curve with an intermonomer distance of 12.07 Å.

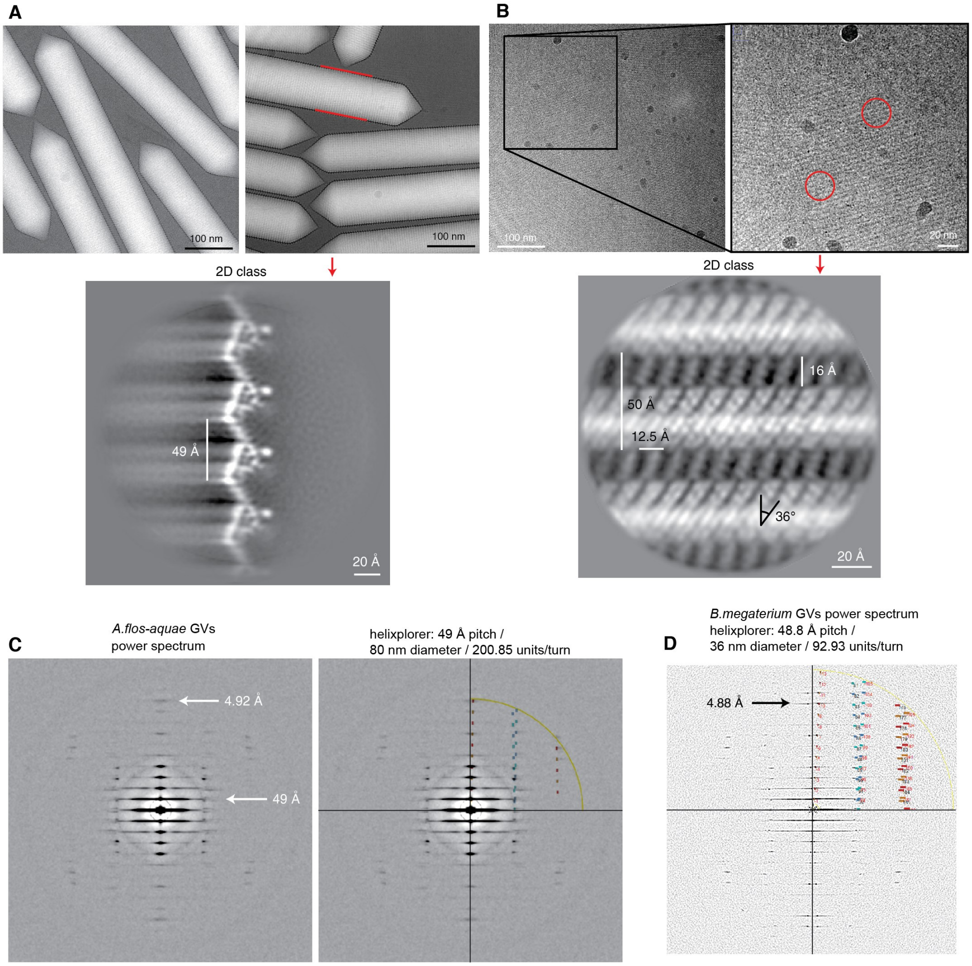

Figure A4: Cryo-EM of *A. flos-aquae* GVs, related to Figure 3.5. (A) Representative micrographs of *A. flos-aquae* gas vesicles. GV edges were analyzed by 2D class averaging to give a low-noise high-resolution 2D view of the edges, to reveal a repetitive zig-zag pattern. The 2D view shows details of at least 5.4 Å resolution corresponding to the α-helical pitch. (B) The same dataset contained collapsed gas vesicle wall segments. Those can be averaged as well by 2D class averaging to reveal a high-resolution top-view of the GV wall with better than 4.8 Å resolution as the β-strands are resolved. (C) Computing the sum of in-plane rotated power spectra of segments of all GVs in the dataset gives rise to a layer-line pattern typical for helical assemblies.

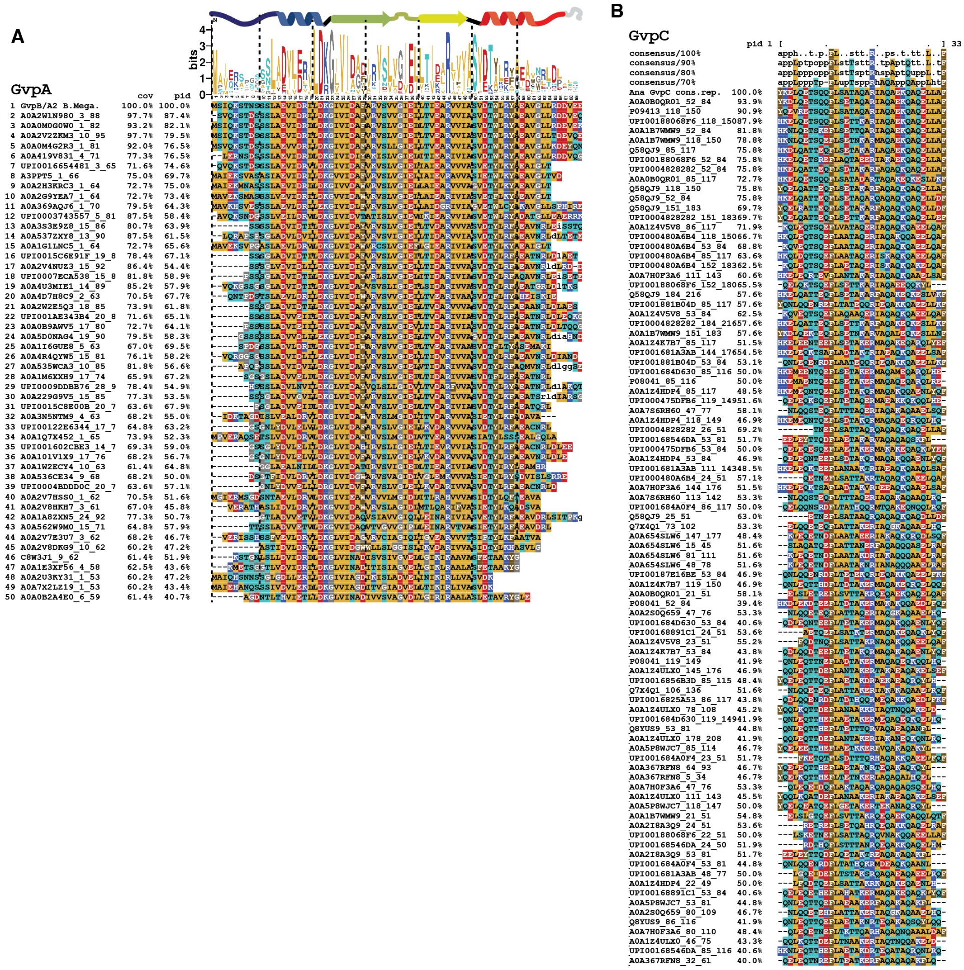

Figure A5: Evolutionary conservation of GV proteins, related to Figure 3.7. (A) Multiple sequence alignment of *B. megaterium* GvpA2 with 50 sampled UniRef90 clusters of 40-100% sequence identity. (B) MSA of sequences similar to *A. flos-aquae* GvpC 33 AA repeats. Alignment of 33 amino acid repeat consensus sequence of Ana GvpC with 91 similar sequences from UniRef90 clusters with 40-100% sequence identity reveals a highly conserved pattern.

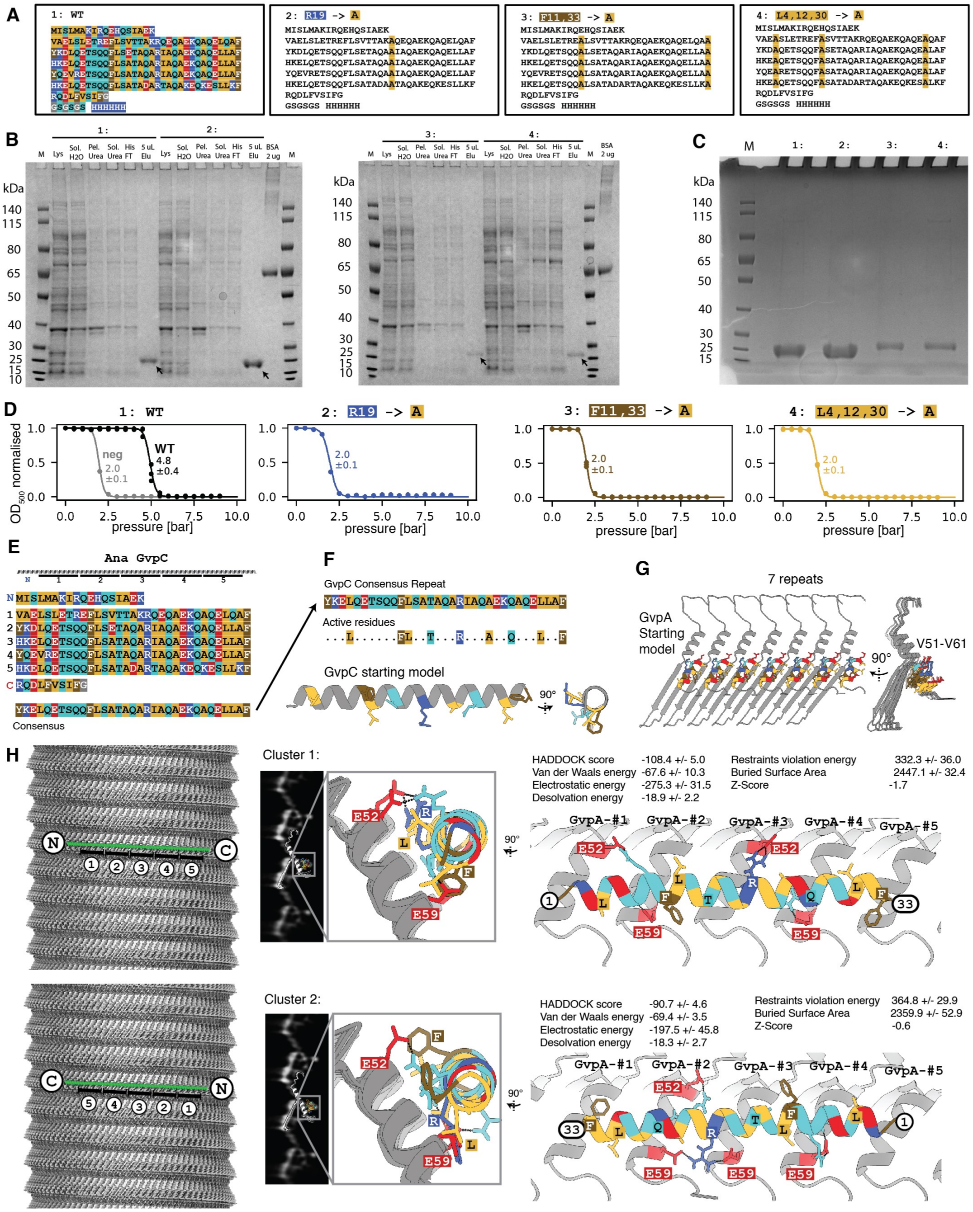

Figure A6: Binding analysis of GvpC to *A. flos-aquae* gas vesicles, related to Figure 3.7. (A) A GvpC wild-type construct and three mutants were designed with F, L, and R residues in all five repeats mutated to alanine. All constructs have a C-terminal GSGSGS linker and 6x His-tag. (B) SDS-PAGE following purification steps of wild-type GvpC and point mutants. (C) Collapse pressure measurements of the four constructs confirm binding to *A. flos-aquae* gas vesicles of the wild-type construct and loss of binding for the mutants.

ACKNOWLEDGEMENTS

Completing this PhD has been a long and transformative journey, filled with both challenges and moments of profound insight. Throughout this process, I have been fortunate to receive the support, guidance, and encouragement of many people, without whom this work would not have been possible. As I reflect on this journey, I am deeply grateful to those who not only made it possible but also made it an unforgettable experience.

First and foremost, I must extend my heartfelt thanks to my supervisor, David. Your continuous support, relentless optimism, and the opportunity you provided have been invaluable. The journey was not always easy, and during the difficult times, your kind words and positive outlook truly meant a lot to me. Those early years were particularly challenging, as we navigated the initial teething problems of nurturing this lab, dealt with the global pandemic, and still strived to conduct meaningful science. I believe that through these shared experiences, we have grown both as scientists and as individuals. I wish you the very best in all your future endeavors, both in science and in life.

I would also like to express my deepest gratitude to Nico for the insightful questions, helpful comments, and especially for providing the final push to complete this dissertation. Your direct approach to science and quick mind have left a lasting impression on me. It has been an honor to be one of the last PhD students to graduate under your tenure. Your influence will continue to inspire me as I move forward in my career.

The intellectual environment of the Medical Imaging department, and the MarescaLab in particular, has been a constant source of inspiration. To my lab mates, both past and present, thank you. To Rick and Baptiste, who were there in those early days of the MarescaLab: you showed me the meaning of hard work and dedication. Your support, both technical and personal, not only made this work possible but made it fun. I finish this journey with fond memories of good coffee, late-night deadlines, long days at the NIN, and fun trips abroad. Speaking of long days at the NIN, I would like to thank Eleonora and Min for their amazing work ethic and great lunch conversations! A special thanks to Vidya for keeping the biolab running during those first years.

To all the people at the lab, both past and current: Hugues, Gabrielle, Olivia, Tarannum, Xin, Myrthe, Alina, Twan, Liam and Merijn, thank you for creating such a supportive and vibrant space. The discussions, seminars, and impromptu hallway chats made the long hours feel less like work and more like a shared adventure. I would like to thank Juancito in particular for his amazing contribution to our work, both in this thesis and outside, and for his amazing attitude and great workmanship. I hope you have the same fond memories of your thesis project as I have, and find the same enjoyment in your own PhD journey.

I would like to thank the entire medical imaging group: Guillaume, Agis, Martijn, Djalma, Masa, Aida, Paulina, Chiara, Fabian, Sebastian, Chih-Hsien, Martina and Xiufeng for making me feel at home in our little corner of the university.

I would also like to thank the administrative and technical staff: Henry, Annelies, Angela. Your tireless efforts behind the scenes, from organizing outings to helping book trips for conferences, helping with administration, and technical advice and repairs, and everything in-between, were absolutely critical. Your support allowed me to focus on my research, and for that, I am truly grateful.

I would like to thank all my friends who supported me; the nerdgame friends for the regular boardgame nights, all the people who joined me in surf-, skate- and climbing adventures, and the people from OMA collective for giving me the opportunity and space to let my DIY-demon out.

None of this would, of course, be possible without the unwavering support and love of my partner Gwen, and more recently the unbridled joy of our son Oliver. Throughout my PhD, Gwen has put up with my grumbling and complaining, my stressed-out anxiety, and my work-related absence with an unrivalled strength and grace. For being my steadfast support and home, she has my gratitude, and my love she has and will have always.

This thesis represents my efforts and the incredible support of everyone who helped me. From the bottom of my heart,

Thank you.

CURRICULUM VITÆ

Dion TERWIEL

10-03-1993	Born in Schiedam, Netherlands.

EDUCATION

2005 - 2011	Secondary education Stedelijk Gymnasium Schiedam, Delft
2014 - 2017	B.Sc. in Life Science and Technology Delft University of Technology
2017 - 2019	M.Sc. in Life Science and Technology Delft University of Technology, Delft
2020 - 2025	PhD. Biotechnology and Physics Delft University of Technology, Delft *Thesis:* From bacteria to biosensors: Engineering gas vesicles for biomolecular ultrasound imaging *Promotors:* Prof. dr. ir. N. de Jong Dr. ir. D. Maresca

AWARDS

2021	ISBUS poster Award
2023	WMIC poster award
2024	EMIM young investigator award
2024	EMIM Educational stipend

LIST OF PUBLICATIONS

4. **Terwiel, D**., Park, B.M., Heiles, B., Waasdorp, R., Munoz-Ibarra, E., Ara, T., Gazzola, V. and Maresca, D. (2025). Acoustic pH sensor for dynamic ultrasound imaging of cellular acidification. bioRxiv, pp.2025-01.

3. Heiles, B., Nelissen, F., **Terwiel, D.**, Park, B. M., Munoz Ibarra, E., Matalliotakis, A., & Maresca, D. (2024). Nonlinear sound-sheet microscopy: imaging opaque organs at the capillary and cellular scale. bioRxiv, 2024-07.

2. Huber, S. T., **Terwiel, D.**, Evers, W. H., Maresca, D., & Jakobi, A. J. (2023). Cryo-EM structure of gas vesicles for buoyancy-controlled motility. Cell, 186(5), 975-986.

1. Heiles, B., **Terwiel, D.**, & Maresca, D. (2021). The advent of biomolecular ultrasound imaging. *Neuroscience* **474**, 122-133.